Ceramic Coatings for Clad (The C³ Project): Advanced Accident-Tolerant Ceramic Coatings for Zr-Alloy Cladding

Fuel Cycle
Integrated Research Project

Kurt E. Sickafus
University of Tennessee at Knoxville

In collaboration with:
Pennsylvania State University
University of California, Berkeley
University of Colorado, Boulder
University of Michigan
University of Manchester
University of Oxford
University of Huddersfield
University of Sheffield

Frank Goldner, Federal POC
Jon Carmack, Technical POC
Stu Maloy Technical POC
Buzz Savage, Technical POC

NEUP | Nuclear Energy University Programs

U.S. Department of Energy

FINAL PROJECT REPORT

Project Title: *Ceramic Coatings for Clad (The C^3 Project): Advanced Accident-Tolerant Ceramic Coatings for Zr-alloy Cladding*

Covering Period: 02/14/2013 – 02-14-2017

Date of Report: February 14, 2017

Recipient: University of Tennessee
                  Knoxville, TN 37996-2100

Award ID Number: 12-4722

Principal Investigator: Kurt E. Sickafus, 865-974-4858, kurt@utk.edu
Co-PIs:
U. of Tennessee (UT)
Brian Wirth   bdwirth@utk.edu
Larry Miller   lfmiller@utk.edu
Bill Weber   wjweber@utk.edu
Yanwen Zhang   yanwen@utk.edu
Maulik Patel   maulik@utk.edu

Penn State (PSU)
Arthur Motta   atm2@psu.edu
Doug Wolfe   dew125@arl.psu.edu

University of California at Berkeley
Max Fratoni   maxfratoni@berkeley.edu

U. Colorado (UC)
Rishi Raj   rishi.raj@colorado.edu
Kenneth Plunkett   kenfplunkett@gmail.com

U. Michigan (UM)
Gary Was   gsw@umich.edu

LANL
Kendall Hollis   kjhollis@lanl.gov
Andy Nelson   atnelson@lanl.gov
Chris Stanek   stanek@lanl.gov

Westinghouse (W)
Robert Comstock   comstorj@westinghouse.com
Jonna Partezana   partezjm@westinghouse.com

U. Sheffield (US)
Karl Whittle   k.r.whittle@sheffield.ac.uk

Manchester U. (MU)
Michael Preuss   michael.preuss@manchester.ac.uk
Philip Withers   philip.withers@manchester.ac.uk

Oxford U. (OU)
Angus Wilkinson   angus.wilkinson@materials.ox.ac.uk

Huddersfield (UH)
Stephen Donnelly   s.e.donnelly@hud.ac.uk

ANSTO
Daniel Riley   dry@ansto.gov.au

Project Goals and Objectives
The goal of this NEUP-IRP project is to develop a fuel concept based on an advanced ceramic coating for Zr-alloy cladding. The coated cladding must exhibit demonstrably improved performance compared to conventional Zr-alloy clad in the following respects:
During normal service, the ceramic coating should decrease cladding oxidation and hydrogen pickup (the latter leads to hydriding and embrittlement).
During a reactor transient (e.g., a loss of coolant accident), the ceramic coating must minimize or at least significantly delay oxidation of the Zr-alloy cladding, thus reducing the amount of hydrogen generated and the oxygen ingress into the cladding.

The specific objectives of this project are as follows:
To produce durable ceramic coatings on Zr-alloy clad using two possible routes: (i) MAX phase ceramic coatings or similar nitride or carbide coatings; and (ii) graded interface architecture (multilayer) ceramic coatings, using, for instance, an oxide such as yttria-stabilized zirconia (YSZ) as the outer protective layer.
To characterize the structural and physical properties of the coated clad samples produced in 1. above, especially the corrosion properties under simulated normal and transient reactor operating conditions.
To perform computational analyses to assess the effects of such coatings on fuel performance and reactor neutronics, and to perform fuel cycle analyses to assess the economic viability of modifying conventional Zr-alloy cladding with ceramic coatings.

This project meets a number of the goals outlined in the NEUP-IRP call for proposals, including:
Improve the fuel/cladding system through innovative designs (e.g. coatings/liners for zirconium-based cladding)
Reduce or eliminate hydrogen generation
Increase resistance to bulk steam oxidation

Achievement of our goals and objectives, as defined above, will lead to safer light-water reactor (LWR) nuclear fuel assemblies, due to improved cladding properties and built-in accident resistance, as well as the possibilities for enhanced fuel/clad system performance and longevity.

Summary of Research Accomplishments
Below, we summarize the most significant highlights of this project.
Note that figures, tables, equations, etc., are numbered separately for each section.

I. **Summary of Penn State University (PSU) and Westinghouse Experimental Research Accomplishments**

This research was focused on developing nuclear fuel claddings with ceramic nitride coatings that can perform well in normal operation conditions and withstand transient conditions such as loss of coolant accident for longer durations to provide more coping times. As an innovative approach, this study considered application of monolithic and multilayer $Ti_{1-x}Al_xN$ (where x~0.54-0.67) and TiN [henceforth referred to as TiAlN or TiN, respectively] coatings on ZIRLO® substrate by cathodic arc physical vapor deposition (CA-PVD) to improve corrosion resistance without requiring a major core design change. Coating performance development was investigated step-by-step by considering the effect of a certain processing parameters and design architectures iteratively via deposited coating generations (GENs). The coating deposition parameters considered for each coating design generation are summarized in Table 1.

Table 1. Investigated coating deposition parameters and design architecture generations.

Generation	Coating	Parameter
GEN-1	TiAlN	Bond coating thickness
GEN-2	TiAlN	Top coating thickness and surface roughness
GEN-3	TiAlN	Processing parameters (N_2 flow, bias, current)
GEN-4	TiAlN/TiN	Design architectures (multilayers and TiN barrier layer)
GEN-5	TiAlN/TiN	Design architectures (multilayers and functionally graded materials (FGM))
GEN-6	TiAlN/TiN	Design architectures (FGM and Multilayers)
GEN-7	ZrN	ZrN Monolayers
GEN-8	TiAlN	TiAl composition, bias and thickness (UK Analysis)
GEN-9	TiAlN/TiN	Surface preparation and increased Al content within the TiAlN coating

Westinghouse provided ZIRLO® substrate material, which had a nominal chemical composition of 1 wt.%Nb, 1 wt.%Sn, 0.1 wt.% Fe and balance Zr. Initially, the coating performance on flat samples (2.54 x 5.08 x 0.05 cm) were studied. As the research progressed, the coating performance on tubular samples (length: 3.81, outer diameter: ~1 cm, inner diameter: ~0.85 cm) was also evaluated. Before coating deposition, the substrate surface was prepared by hand grinding with SiC paper having 240, 600 and 800 grit, except GEN-9 samples. GEN-9 samples involved scotch brite, grit blast and lathe applications in addition to SiC hand grinding. Surface roughness measurements were done using a SJ-201P Surface Roughness Tester and optical profilometry.

Coatings were deposited in a vacuum deposition chamber with dimensions of 50.8 cm x 50.8 cm x 50.8 cm allowing for good coating uniformity. Cylindrical solid cathodes were used with three different compositions: high purity (99.999%) elemental titanium, 33at.%Ti-67at.%Al and 20at.%Ti-80at.%Al (only in GEN-9). The substrate coupon temperature during deposition was ~325°C. Prior to deposition, sputter cleaning was performed to remove the native oxide from the substrate surface and improve coating adhesion by applying -1000 V bias. Titanium bond coating (Ti-BC) layer was deposited on the substrate surface prior to the coating deposition

in order to improve adhesion between the substrate and the coating. Coating properties specific for each sample are provided in Tables 2, 3 and 4. The total coating thickness and compositions resulted in a negligible neutronic penalty realtive to uncoated ZIRLO [1]. A 1.6 mm diameter hole was drilled near one edge of the sample for mounting the sample on an autoclave tree during autoclave corrosion tests.

Corrosion testing was performed at Westinghouse in a static autoclave in pure water up to 180 days at 360ºC and saturation pressure, corresponding to 18.7 MPa at this temperature. The autoclave material was 316 stainless steel. An uncoated ZIRLO® sample was also tested in each test to be used as a reference for the coating performance. The corrosion tests were performed according to ASTM G2 standard practice. Weight gain measurements were performed following the autoclave test as a measure of corrosion, and the samples were examined visually using optical microscopy (OM).

Further characterization was performed using X-ray diffraction (XRD) to determine phases, scanning electron microscopy (SEM) to determine coating thickness and evaluate coating microstructure, and energy dispersive X-ray spectroscopy (EDS) to determine coating composition and oxygen penetration behavior. Both surface roughness and cross-sectional SEM/EDS analyses were performed. Surface morphology evaluations were conducted directly after the autoclave test. Analyses of coating cross sections were conducted by sectioning the samples in half, mounting in cold mount epoxy, grinding and polishing. X-ray diffraction (XRD) studies were conducted on a PANalytical XPert Pro Multi-Purpose Diffractometer (MPD) instrument with 240 mm radius, fixed divergence slit (0.25°), receiving slit (0.25°), using Cu K_α ($K_\alpha1$=1.54056 Å, $K_\alpha2$=1.54443Å) radiation. XRD analysis with Grazing Incidence (GI) and Bragg-Brentano (BB) scans were performed with a step size of 0.026° two-theta to reveal the phases formed during corrosion. Penetration depth according to the incidence angle in XRD-GI was determined by using the Highscore software. Backscatter and secondary electron scanning electron microscopy (SEM) measurements were conducted using a FEI Quanta 200 Environmental SEM at 80 Pa pressure and 20 kV high voltage.

Table 2: Cathodic Arc Physical Vapor Deposition Parameters for monolithic TiAlN and TiN coating fabrication.

ID	GEN	Coating	Ra (µm)	Coating Thickness (µm)	Deposition time (min) (BC/TC)	Substrate Bias (BC/TC)	N$_2$ partial pressure (Pa)	Varying Parameter
E1	1	TiAlN	0.250	~13	6/450	150/50	1.6	Ti BC-0.2 µm
E2	1	TiAlN	0.250	~14	8/450	150/50	1.6	Ti BC-0.4 µm
E3	1	TiAlN	0.250	~12	10/450	150/50	1.6	Ti BC-0.6 µm
E4	1	TiAlN	0.250	~14	15/450	150/50	1.6	Ti BC-0.8 µm
E5	2	TiAlN	0.100	~4	8/112.5	150/50	1.6	TiAlN = 4 µm Ra = 0.1 µm
E6	2	TiAlN	0.250	~4	8/112.5	150/50	1.6	TiAlN = 4 µm Ra = 0.25 µm
E7	2	TiAlN	0.500	~4	8/112.5	150/50	1.6	TiAlN = 4 µm Ra = 0.5 µm

E8	2	TiAlN	0.875	~4	8/112.5	150/50	1.6	TiAlN = 4 μm Ra = 0.875 μm
E9	2	TiAlN	0.100	~8	8/225	150/50	1.6	TiAlN = 8 μm Ra = 0.1 μm
E10	2	TiAlN	0.250	~8	8/225	150/50	1.6	TiAlN = 8 μm Ra = 0.25 μm
E11	2	TiAlN	0.500	~8	8/225	150/50	1.6	TiAlN = 8 μm Ra = 0.5 μm
E12	2	TiAlN	0.875	~8	8/225	150/50	1.6	TiAlN = 8 μm Ra = 0.875 μm
E13	2	TiAlN	0.100	~12	8/450	150/50	1.6	TiAlN = 12 μm Ra = 0.1 μm
E14	2	TiAlN	0.250	~12	10/450 8/225	150/50	1.6	TiAlN = 12 μm Ra = 0.25 μm
E15	2	TiAlN	0.500	~12	8/450	150/50	1.6	TiAlN = 12 μm Ra = 0.5 μm
E16	2	TiAlN	0.875	~12	8/450	150/50	1.6	TiAlN = 12 μm Ra = 0.875 μm
E18	3	TiAlN	0.250	~12	8/450	150/50	1.9	slightly increased N₂ pressure
E19	3	TiAlN	0.250	~12	8/450	150/100	1.9	increased substrate bias to 100 V and N₂ pressure
E20	3	TiN	0.250	~12	8/370	150/150	1.6	Composition (TiN)

*BC=bond coat, TC=Top coat

Table 3: Cathodic Arc Physical Vapor Deposition Parameters for monolithic TiN and multilayer TiN/TiAlN coating fabrication.

ID	GEN	Coating	# of layers		Deposition rate (μm /min)		Total coating
			TiN	TiAlN	TiN	TiAlN	Thickness, (μm)
E21	5	TiN	1		0.018		8.1
E22	5	TiN(thin)/ Ti$_{1-x}$Al$_x$N (thick)	1	1	0.017	0.025	11.1
E23	5	TiN/ Ti$_{1-x}$Al$_x$N 2-layer	1	1	0.026	0.026	11.8
E24	4	TiN/ Ti$_{1-x}$Al$_x$N 4-layer	2	2	0.020	0.020	8.9
E25	5	TiN/ Ti$_{1-x}$Al$_x$N 8-layer	4	4	0.022	0.022	9.8
E26	5	TiN/ Ti$_{1-x}$Al$_x$N 16-layer	8	8	0.024	0.024	10.9

Table 4. Cathodic arc physical vapor deposition parameters used to deposit the coatings in the sequence: Ti\4x(TiAlN\TiN) on green scotch brite prepared tubes.

Run ID	GEN	Tube	Flat	Composition (Ti/Al), at%	Dep. time (min)	Substrate bias (volts)	Source Current (Amps)
C150408	9	PT342	PF620	20/80	8\4x(35.2\35.2)	150\4x(50\150)	65\4x(45\65)
C150410	9	PT348	PF625	20/80	8\4x(50.0\50.0)	150\4x(50\150)	65\4x(45\45)
C150414	9	PT353	PF631	20/80	8\4x(50.0\50.0)	150\4x(75\150)	65\4x(45\45)
C150416	9	PT354	PF633	33/67	8\4x(50.0\50.0)	150\4x(75\150)	65\4x(45\45)

Results and Conclusions

a)   **Ti-BC thickness effect:** The samples (Table 2) with 0.2 and 0.4 µm bond coat thickness suffered weight loss as shown in Fig. 1a, indicating an unstable coating layer in which coating delamination occurred during corrosion. The thicker bond coating samples showed better corrosion behavior: the average weight gain of both thicker (0.6 and 0.8 µm) bond coat samples was minimal compared to that of the uncoated ZIRLO$^{®}$ sample. The 0.8 µm bond coating thickness showed a positive weight gain of only 3 mg/dm^2 and no indication of coating spallation under visual inspection while the 0.6 µm samples showed a similarly low average weight gain without spallation. So, a 0.6 µm thick Ti bond coating between the ZIRLO$^{®}$ substrate and the TiAlN top coating is enough to achieve good coating adhesion to the substrate and corrosion resistant coating performance.

b)   **Substrate surface roughness (R$_a$) and coating thickness effects:** To investigate the substrate surface roughness effect on coating durability, ZIRLO$^{®}$ substrate surface roughness values of 0.1, 0.25, 0.5 and 0.875 µm R$_a$ were prepared prior to coating deposition (Table 2). Additionally, to investigate the effect of the TiAlN top coat thickness on corrosion performance, 4, 8 and 12 µm thick coatings were deposited on ZIRLO$^{®}$ substrate coupons (with fixed 0.6 µm Ti BC thickness layer). The combination of a 0.25 µm R$_a$ substrate surface roughness and a 12 µm top coat layer thickness provided the optimum coating characteristics to obtain best adhesion for CA-PVD TiAlN coatings on ZIRLO$^{®}$ substrates with Ti-BC considering the weight gain data (Fig. 1b) and visual examination.

(a)   (b)
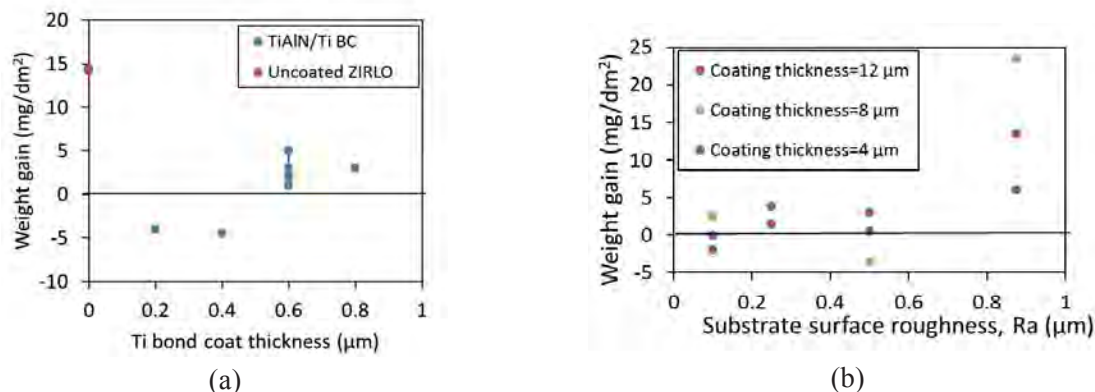
Figure 1. Sample weight gain data with respect to (a) Ti bond coat thickness with TiAlN (~13 µm thickness) top coating after autoclave test exposure at 360°C for 3 days. 0.6 µm Ti bond coat thickness were the minimum values needed to ensure coating durability and prevent spallation during the corrosion tests. (b) ZIRLO$^{®}$ substrate surface roughness values and TiAlN coating thickness values after autoclave testing at 360°C for 3 days.

The XRD results showed that ZIRLO$^{®}$ (ICDD PDF# 00-005-0665) had a basal fabrication texture, leading to a high intensity of the (0002) peak. TiAlN layer was identified as Ti$_{0.5}$Al$_{0.5}$N (ICDD PDF# 04-005-5251). After corrosion test, anatase (ICDD PDF# 04-002-8296) and boehmite phases (ICDD PDF# 00-021-1307) were identified. The boehmite phase was observed as a white region (Fig.2a), identified via XRD (Fig. 2b), and determined to be non-

uniform by using SEM (Fig.2c). The boehmite phase formed due to aluminum migration to the outer surface where it reacted with steam to form AlO(OH) during the autoclave exposure (Fig. 2d and e). To avoid formation of this non-protective phase, TiN coating was considered as an Al diffusion barrier.
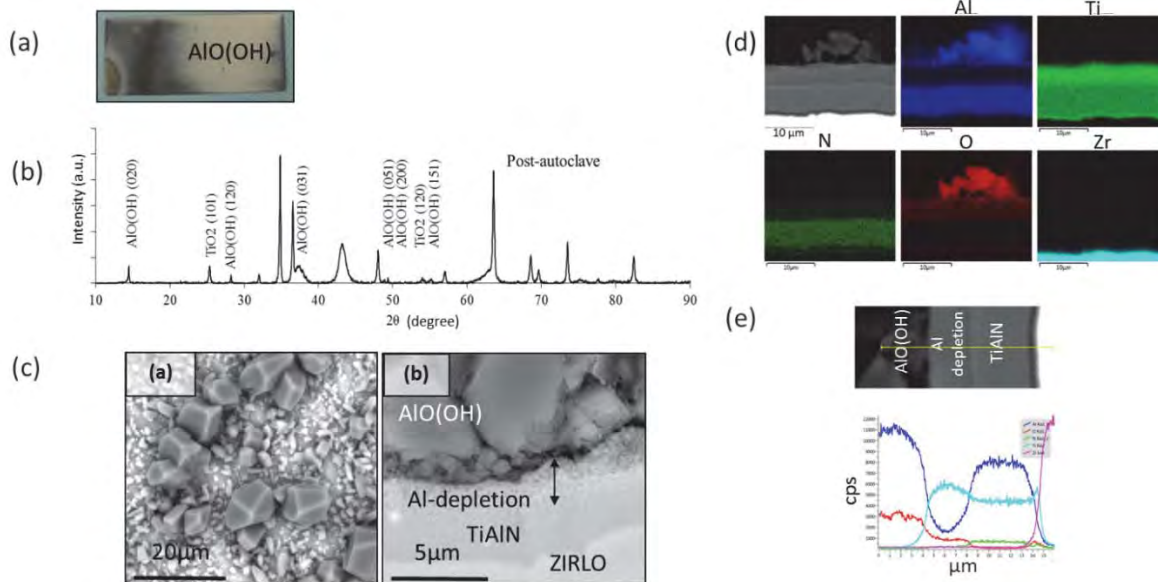

Figure 2. Characterization of TiAlN coated ZIRLO® autoclave tested at 360ºC for 3 days. (a) Digital image, (b) XRD, (c) SEM, (d) Cross section EDS-map analysis, and (e) EDS-line scan showing Al, Ti, N, O and Zr elemental analysis. Al has been shown to have migrated from the top 4 μm TiAlN layer.

c)   **Deposition parameter effect:** The weight gain data for various coating design architectures deposited under different deposition parameters are presented in Fig. 3. An increase in nitrogen partial pressure showed a slight degradation of properties of the coating for the deposition conditions studied. An increase in substrate bias slightly improves corrosion resistance, as the coating microstructure is densified, but the magnitude of the change is less than that effected by a change in nitrogen partial pressure for the deposition condition studied.

Coating	Substrate Bias (BC/TC)	N_2 partial pressure (Pa)	Weight gain (mg/dm²)
TiAlN	150/50	1.6	1.5
TiAlN	150/50	1.9	17
TiAlN	150/100	1.9	10.1
No coating	N/A	N/A	14.4
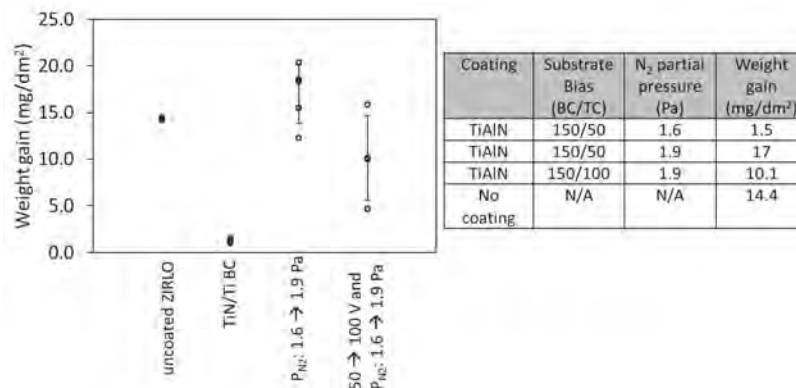
Figure 3. Weight gain data obtained after the autoclave test at 360ºC for 3 days of uncoated ZIRLO®, sample with TiAlN coating deposited by slightly increased nitrogen pressure, sample with TiAlN coating deposited by 100 V of substrate bias and sample with TiN coating.

d)   **Multilayer coatings - Design architecture:** TiN and TiAlN multilayer coatings with various architectures (2-, 4-, 8- and 16-layers) (Table 3) were deposited on ZIRLO® coupons per the previously determined deposition parameters, Ti bond coating with thickness of 0.6 μm and a substrate surface with 0.25 μm R_a roughness. The primary goal was to determine the optimum multilayer design architecture and determine the minimum TiN top layer thickness to achieve a coating that would withstand 360ºC water exposure up to 90 days with minimal weight gain, no boehmite phase formation, no penetration of oxygen, no cracking and no debonding. SEM images of the surface morphology and cross sections of select design architectures after 33 days autoclave exposure are presented in Fig.4.
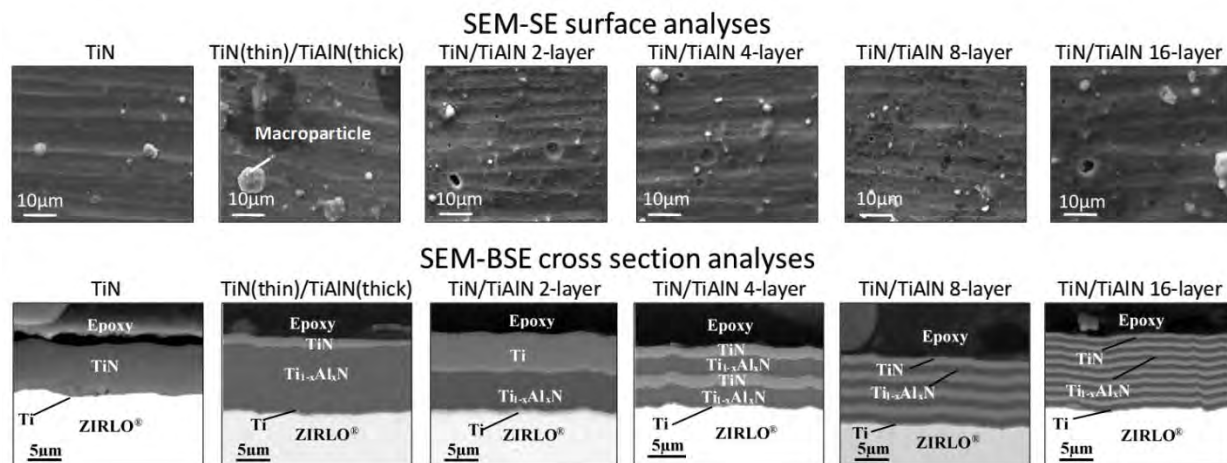
Figure 4. SEM surface and cross section images of multilayer coated flat samples autoclave test at 360°C and 18.7 MPa for 33 days. No coating spallation was observed.

The weight gain data of these coated samples and uncoated ZIRLO® presented in Fig. 5a shows that the coated samples had an order of magnitude lower weight gain compared to uncoated ZIRLO®. This suggests that multilayer coating can achieve better corrosion resistance than uncoated samples. The data also indicates that the multilayer architecture has a strong influence on corrosion performance.
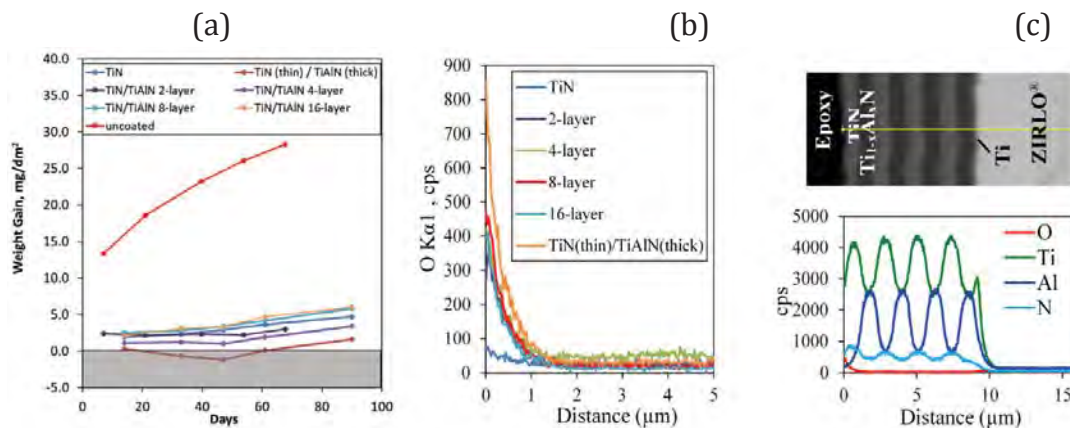
Figure 5.(a) Weight gain (mg/dm^2) data of samples tested in autoclave at 360°C and 18.7 MPa. (b) EDS cross section of oxygen profile through TiN, 2-layer, 4-layer, 8-layer, 16-layer and TiN (thin)/TiAlN(thick) coating starting from the outer layer towards the substrate and (c) oxygen, titanium, aluminum and nitrogen profile through cross section of E25-(TiN/TiAlN 8-layer)/Ti/ZIRLO® sample after autoclave test at 360°C 18.7 MPa for 33 days.

Surface and cross section SEM, EDS and XRD analyses demonstrated that a thin layer (~1μm) of TiN as a diffusion barrier is sufficient to stop Al migration and prevent boehmite phase formation. All coatings could withstand the autoclave test without coating spallation/delamination up to 7 days and most coatings were adherent to the surface for up to 33 days. At the end of 90 days, oxygen penetrated only ~1.5 μm as shown in Fig. 5b. This means that little or no oxide forms on the subsequent layers of the coating or at the substrate and coating interface. Fig. 5c shows a line scan of the multilayer coating for TiN/TiAlN 8-layer coated sample. TiN/TiAlN 8-layer architecture coatings showed the best corrosion performance at 360°C and 18.7 MPa (saturation pressure) compared to other tested multilayer architectures due to no boehmite phase formation, positive weight gain data without any delamination/spallation and prevention of oxygen ingress prevention. We conclude that the best architecture developed (8 and 16-layer TiN/TiAlN multilayer coatings) showed approximately an order of magnitude lower weight gain compared to uncoated ZIRLO® substrate and no delamination or spallation.

e)   **Multilayer coatings – Surface preparation and increased Al content:** The effect of substrate surface preparation methods; SiC grit, lathe preparation, green scotch brite and Al_2O_3 grit blast were examined. Substrate surface roughness was adjusted to ~0.25 μm (~10 microinch) Ra, as shown in Fig. 6.
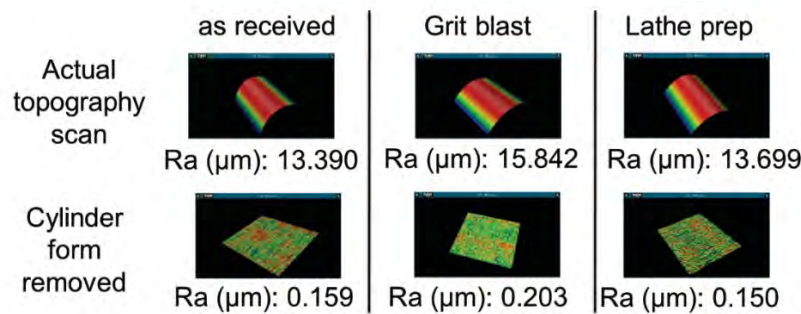
Figure 6. Optical profilometry roughness data of ZIRLO® tubes having a surface prepared with stated methods.

Based on previous test results, the 8-layer TiN/TiAlN coating design architectures were selected for further testing and optimization. Deposition parameters have been maintained the same with the previous depositions except the coating composition. Coating phases were identified as TiN (ICDD PDF#: 04-015-0336) and $Ti_{0.32}Al_{0.68}N$ (ICDD PDF#: 04-017-4686) by using XRD. Corrosion tests were performed in static pure water at 360°C and 18.7 MPa pressure up to 128 days. Green scotch brite prepared samples showed no embedded grits. Based on visual examination (Fig. 7), it was observed that grit blast prepared samples showed the second-best corrosion performance, however during cross sectional SEM analysis Al_2O_3 grit residues were observed at the substrate coating interface as presented in Fig. 8a, which might degrade coating adhesion and eventually coating corrosion performance. Another finding was the nanofiber structures composed of aluminum and oxygen were observed at the spalled regions of grit blast prepared samples, suggesting a healing property of the coating when scratched as presented in Fig. 8b.
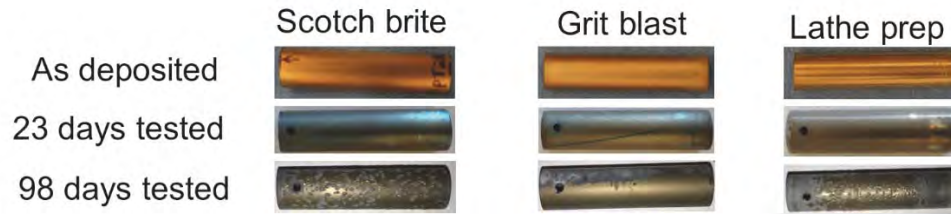
Figure 7. Digital images in the as deposited and after 23 day and 98 day autoclave exposure. Localized blisters observed at scotch brite and lathe prepared samples starting from 23 days leading to spallation at 98 days
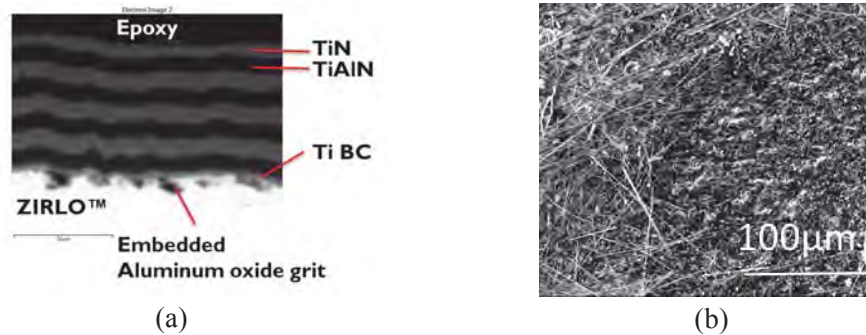

(a) (b)

Figure 8. SEM analyses of grit blast prepared samples, (a) cross section image and (b) surface image of spalled region showing nanofibers.

f) **Multilayer coatings – Deposition parameter effect:** 8-layer coatings were deposited with the parameters specified in Table 4 on green scotch brite prepared samples. Surface and cross-sectional SEM data of as-deposited are shown in Fig. 9 and Fig. 10, respectively.
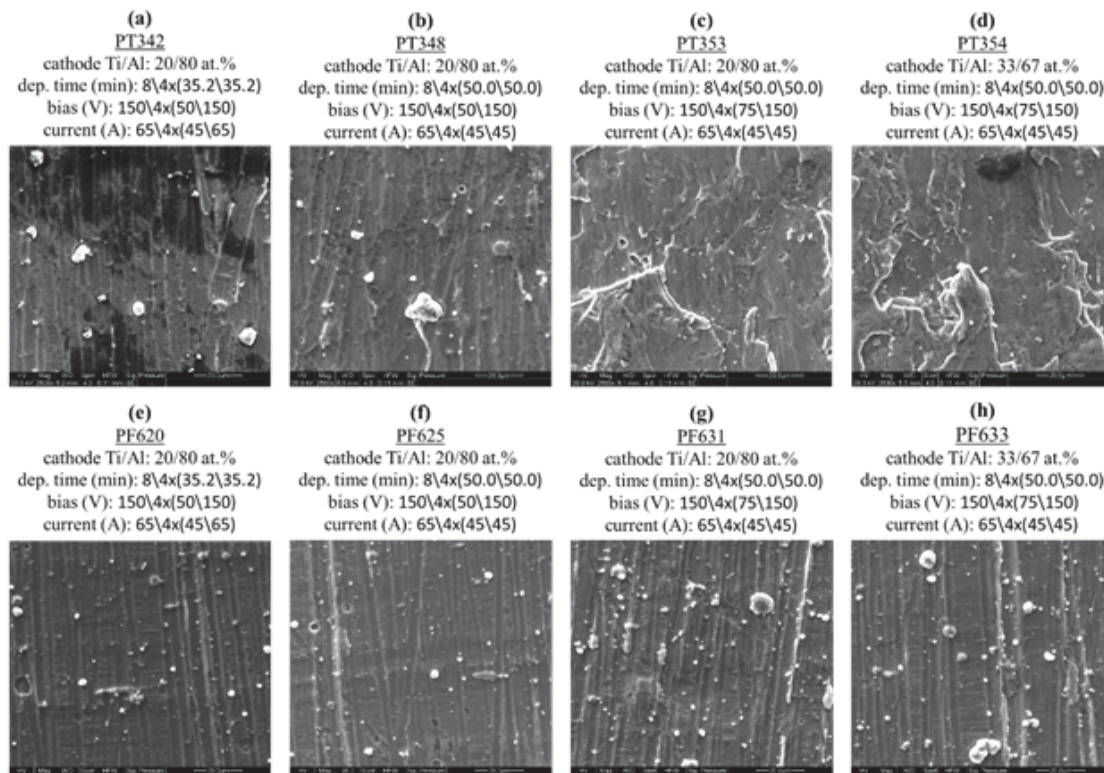
Figure 9. Surface SEM; (a) PT342, (b) PT348, (c) PT353, (d) PT354, (e) PF620, (f) PF625, (g) PF631 and (h) PF633.
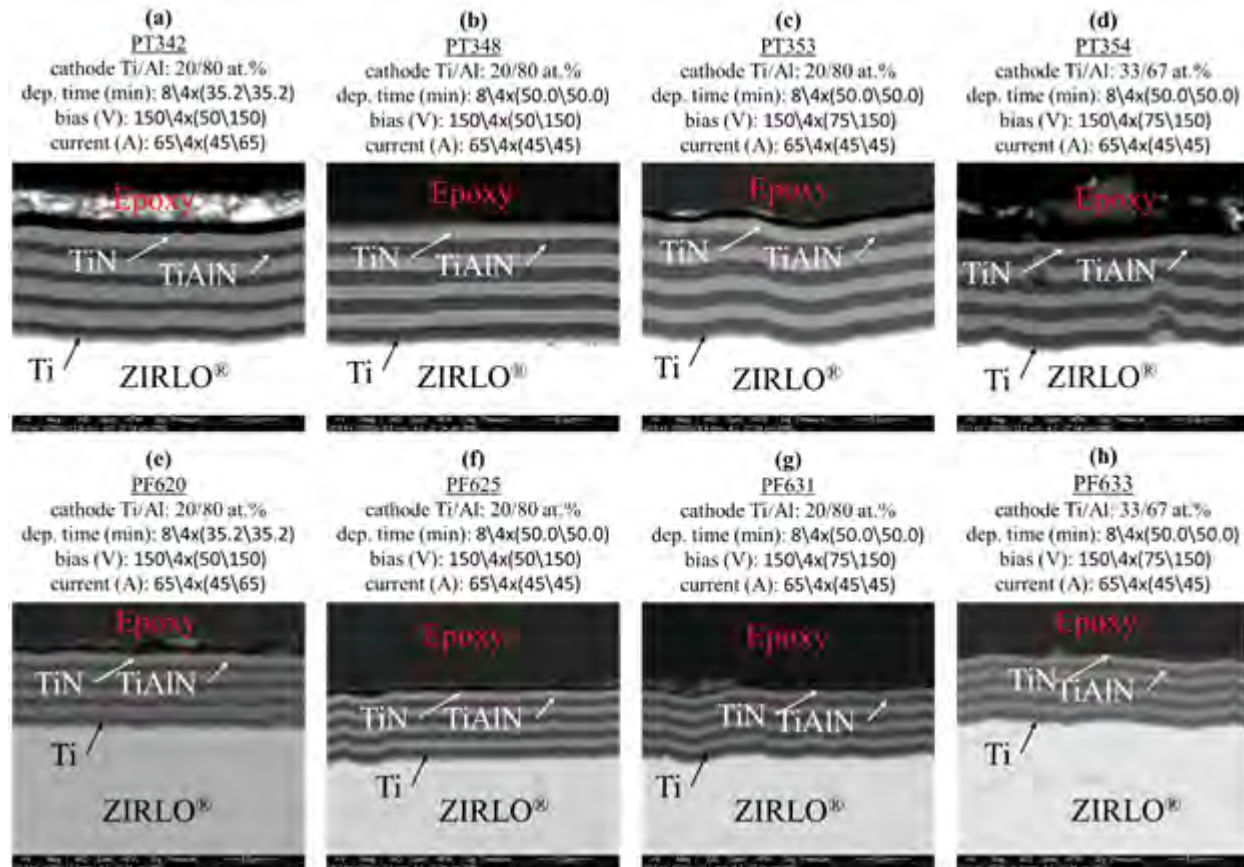
Figure 10. Cross section SEM-BSE images; (a) PT342, (b) PT348, (c) PT353, (d) PT354, (e) PF620, (f) PF625, (g) PF631 and (h) PF633.

It was determined that higher substrate bias resulted in rougher surface morphology on coated samples, leading to non-uniform coating deposition on the surface. No embedded grit was observed at the substrate and the coating interface in case of green scotch brite prepared samples, which is beneficial in terms of achieving better adhesion between the substrate and the coating. Tubular samples were shown to have thicker coatings compared to their flat counterparts, corresponding to 1.5 times more thickness. There was no significant difference in coating layer thickness with substrate bias variation.

Overall Project Summary

In this study, monolithic and multilayer TiAlN and TiN ceramic coatings have been deposited on ZIRLO® coupons and tubes by CA-PVD with the intention of developing an ATF. Cladding performance has been evaluated by using weight gain analyses, SEM, EDS and XRD. Having minimal weight gain, no penetration of oxygen, no cracking, and no debonding has been accepted as the good corrosion resistance criteria.

- Initial studies have been focused on developing monolithic TiN and monolithic TiAlN coatings that adhere well with the sheet ZIRLO® substrate and withstand normal operation conditions for 3 days.
  - Coating adhesion was satisfied by optimizing substrate surface roughness (0.25 µm Ra), Ti-bond coating layer thickness (0.6 µm) and coating deposition parameters.

12

- Post-autoclave sample characterization revealed egress of Al in TiAlN coatings. TiN coating application as a top barrier layer solved this issue and improved corrosion performance.
- Afterwards, coating development efforts were focused on determining the optimum multilayer architecture to achieve desired corrosion performance.
  - A thin layer of (~1μm) TiN was able to act as a barrier to avoid Al diffusion to coating surface and prevent boehmite phase formation.
  - The best architecture was determined to be 8 and 16-layer TiN/TiAlN multilayer coatings which showed approximately an order of magnitude lower weight gain compared to the uncoated ZIRLO® substrate and no delamination or spallation.
  - Substrate surface preparation was determined to be affecting coating corrosion performance. The effect of green scotch brite, alumina grit blasting and SiC lathe preparation were investigated. Alumina grit blasting resulted in Al_2O_3 grit residues. However, aluminum oxide nanofibers were also observed at the spalled regions of these samples.
  - Deposition parameter effects on multilayer coatings were also investigated by varying parameters such as cathode composition, deposition time, bias and current. Effects of these were observed as variations on coating composition, surface roughness and coating thickness.

References

[1]   I. Younker, M. Fratoni, Neutronic evaluation of coating and cladding materials for accident tolerant fuels, Prog. Nucl. Energy. 88 (2016) 10–18. doi:10.1016/j.pnucene.2015.11.006.

List of publications:

1. E. Alat, A.T. Motta, R. J. Comstock, J. M. Partezana, and D. E. Wolfe, Ceramic coating for corrosion (c3) resistance of nuclear fuel cladding, Surf. Coat. Technol. 281 (2015) 133-143.
2. E. Alat, A.T. Motta, R. J. Comstock, J. M. Partezana, and D. E. Wolfe, Multilayer (TiN, TiAlN) ceramic coatings for nuclear fuel cladding, J. Nucl. Materials 478 (2016) 236-244.
3. E. Alat, A.T. Motta, R. J. Comstock, J. M. Partezana, and D. E. Wolfe, Multilayer ceramic coating for corrosion (C3) resistance of nuclear fuel cladding, MS&T16 Conference Paper. (2016).
4. M. Brova, E. Alat, R. Sherbondy, M. A. Pauley, A.T. Motta, and D. E. Wolfe, Ytterbium-Doped Titanium Aluminum Nitride coatings for nuclear fuel cladding (in preparation).
5. E. Alat, M. Brova, I. Younker, A. T. Motta, M. Fratoni, and D. E. Wolfe, High Temperature Performance and Neutronic Analysis of TiN/ Doped TiAlN Coatings on ZIRLO® (in preparation).

List of presentations:

1. **E. Alat,** A.T. Motta, R. J. Comstock, J. M. Partezana, and D. E. Wolfe, Ceramic coating for corrosion (c3) resistance of nuclear fuel cladding, the Materials Day, The Pennsylvania State University, Department of Materials Science and Engineering, September 2015, University Park, PA, poster.

2. **E. Alat,** A.T. Motta, R. J. Comstock, J. M. Partezana, and D. E. Wolfe, Multilayer ceramic coating for corrosion (C3) resistance of nuclear fuel cladding, Materials Science& Technology (MS&T16), October 23-27, 2016, Salt Lake City, UT, presentation.
3. **E. Alat,** A.T. Motta, R. J. Comstock, J. M. Partezana, and D. E. Wolfe, Effect of substrate surface preparation on corrosion performance of multilayer (TiN, TiAlN) coatings, NuMat Conference 2016, November 7-10, 2016, Montpellier, France, poster.

II. Summary of University of Tennessee (UT) Research Accomplishments

The team members at UTK were committed to perform characterization of coatings fabricated by PSU, Univ. Colorado and LANL. In the second year UTK participated in fabricating the coatings in-house as well as characterizing them before and after the autoclave tests. Below we highlight and summarize the effort at UTK.

In the first 12 months of the project UTK performed several characterizations of coatings provided by Univ. of Colorado.

A good example of this study was the detailed microscopy effort on a set of as-deposited and corrosion tested ZrO_{2-x} coated ZIRLO samples. To provide this level of information extending below 1 nm high angle annular bright and dark field (scanning) transmission electron microscopy (STEM) coupled with point-resolved energy-dispersive x-ray and electron energy loss spectroscopy was used to follow the layer chemistry. Focus-ion beam instrument (FIB) was used to first lift-out (<80 nm) thin TEM sections of ZrO_{2-x} coated ZIRLO from, both the as-deposited and tested samples. These sections were then analyzed using high-resolution TEM, selected area electron diffraction (SAED), and S/TEM-based EDS and EELS.
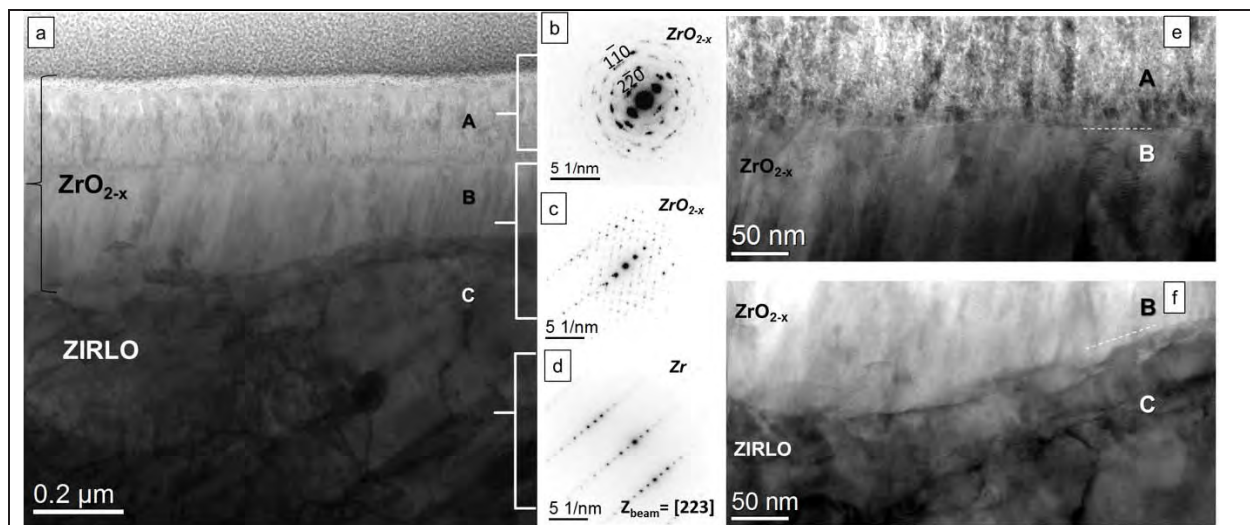
Figigure 1. (a) The as-deposited ZrO_{2-x} thin-film deposited on ZIRLO, following imaged with bright-field STEM image. The micrograph clearly captures the ZrO_{2-x} (~352 nm) thin film deposited directly on ZIRLO. (b-d) Subsequent SAED patterns confirm the presence of these layers, where the ZrO_{2-x} is nanocrystalline. (e) Their two clear interfaces in the sample, one between two ZrO_{2-x} layers and (f) the other between textured ZrO_{2-x} and the ZIRLO substrate.

A closer look at each of the interfaces reveals the details of the coating on ZIRLO. In the case of $ZrO_{2-x}^{\text{Layer A}}$ / $ZrO_{2-x}^{\text{Layer B}}$ shown in **Figure 1e** the interface is undulating by nearly 5 nm, with a clear interface between the two. Deeper into the material, **Figure 1f** is the interface between the bonding $ZrO_{2-x}^{\text{Layer B}}$ / $ZIRLO^{\text{Layer C}}$ the interface is fairly rough and undulating throughout the sample.
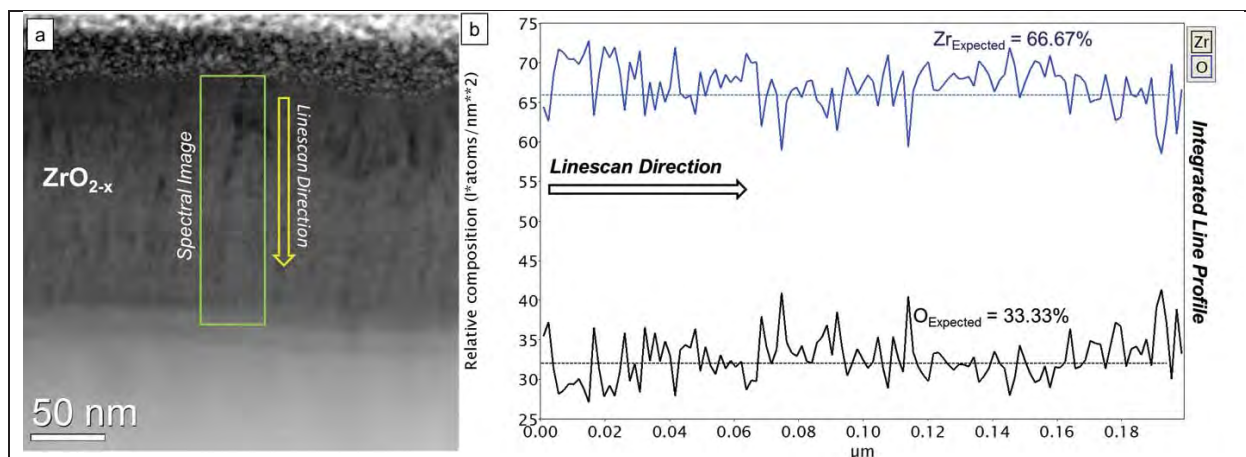
Figure 2. STEM based EELS component chemical mapping was preformed to image the ZrO_{2-x} layer based on the Zr-L and O-K ionization edges. (a) Based on the collected spectral image taken over the area outlined in green, an integrated quantified chemical line plot was calculated (O, black; Z, blue). The line plot depicts a mostly uniform oxide layer.

Based on this quantified EELS map in **Figure 2**, there is clear trend in the data, where there is a higher concentration of oxygen within the first 80 nm and at 140 nm, and respectively a depletion of zirconium.
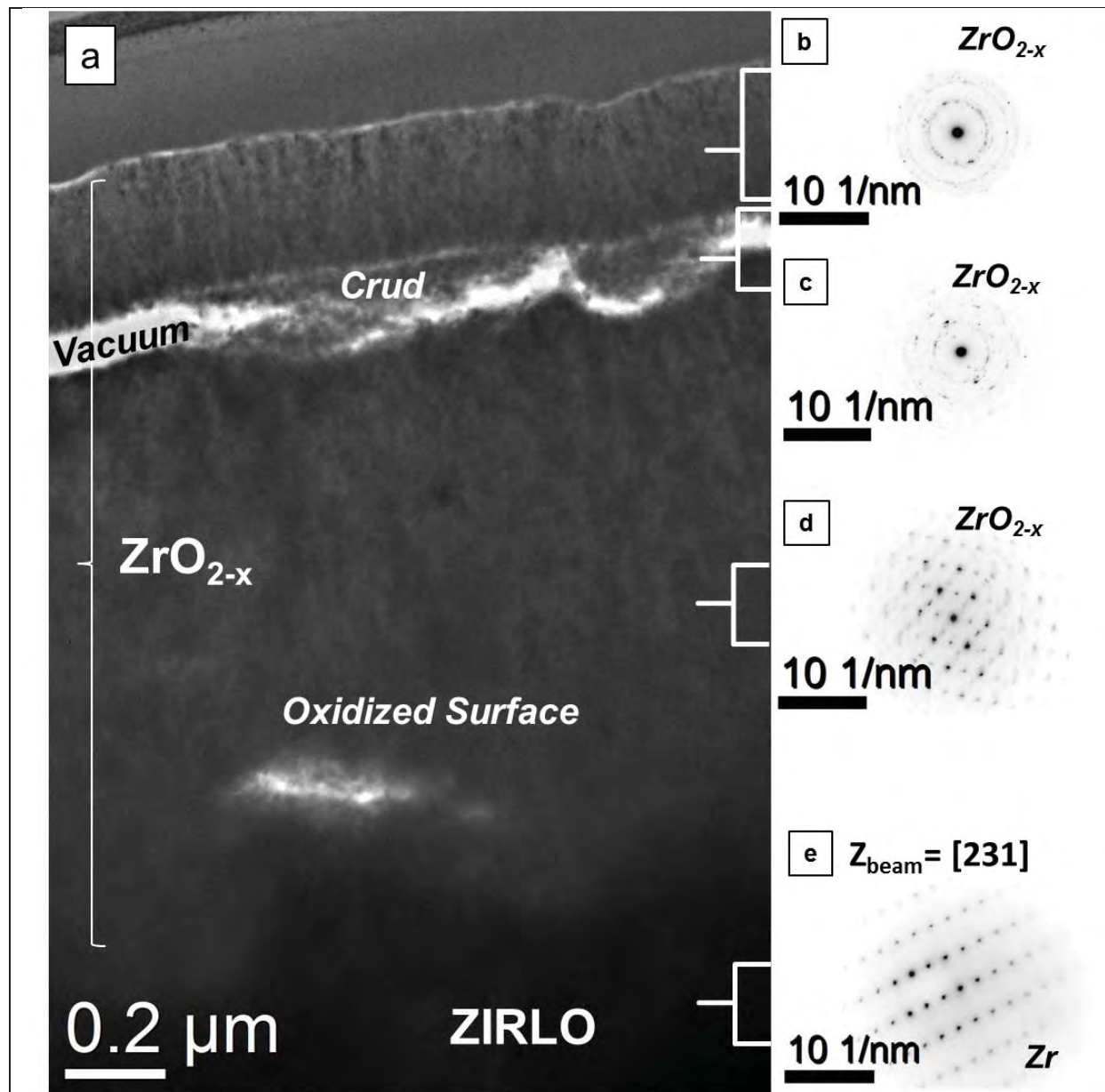
Figure 3. (a) TEM was used to further analyses the structure of the as tested sample. (b-e) SAED patterns were collected that resolve the intact crystallography associated with the sample despite significant departures in the resultant topology following testing.

In the as-tested ZrO_{2-x}/ZIRLO sample we observed clear delamination of the ZrO_{2-x} layer within the first 150 nm, followed by clear surface oxidation of the ZIRLO substrate from the autoclave treatment. The SAED patterns (**Figure 3**), however show crystalline ZrO_{2-x}film at the top, a delaminated gap with crud in the spacing between the film and the substrate and oxidized ZIRLO (ZrO_2 formed post oxidation treatment) and the un-oxidized ZIRLO substrate. From these results we conclude that the film had delaminated during the autoclave treatment and that the water penetrated between the film and the ZIRLO substrate and oxidized the substrate beneath. It is possible that a larger part of the film might have also spalled which would have thus resulted in the lower weight gain.

In the second year, in an effort to augment the fabrication effort, the team at UTK attempted at fabricating Cr_2AlC coatings on Zirlo. In order to explore the perfect sputtering conditions to deposit Cr_2AlC coatings, the initial depositions were performed in a combinatorial manner i.e. a coating with spatial gradient in the elemental composition. The substrate temperatures during these deposition cycles were 450 °C and 550 °C. Grazing incidence XRD (GIXRD) was performed to spatially identify the formation of Cr_2AlC in single phase and hence identify the ideal sputtering conditions.

In-*situ* high temperature GIXRD was performed on a Cr_2AlC coating deposited on a single crystal Al_2O_3 sample in vacuum using an Empyrean diffractometer with an Anton Parr HTK1200N high temperature stage. Scans 2 and 3 in **Figure 4** shows the GIXRD patterns obtained at 250 °C and from 500 °C. One can clearly see that the intensity of (002) peak increases with temperature, this indicated ordering of the Cr-carbide and the Al layers.
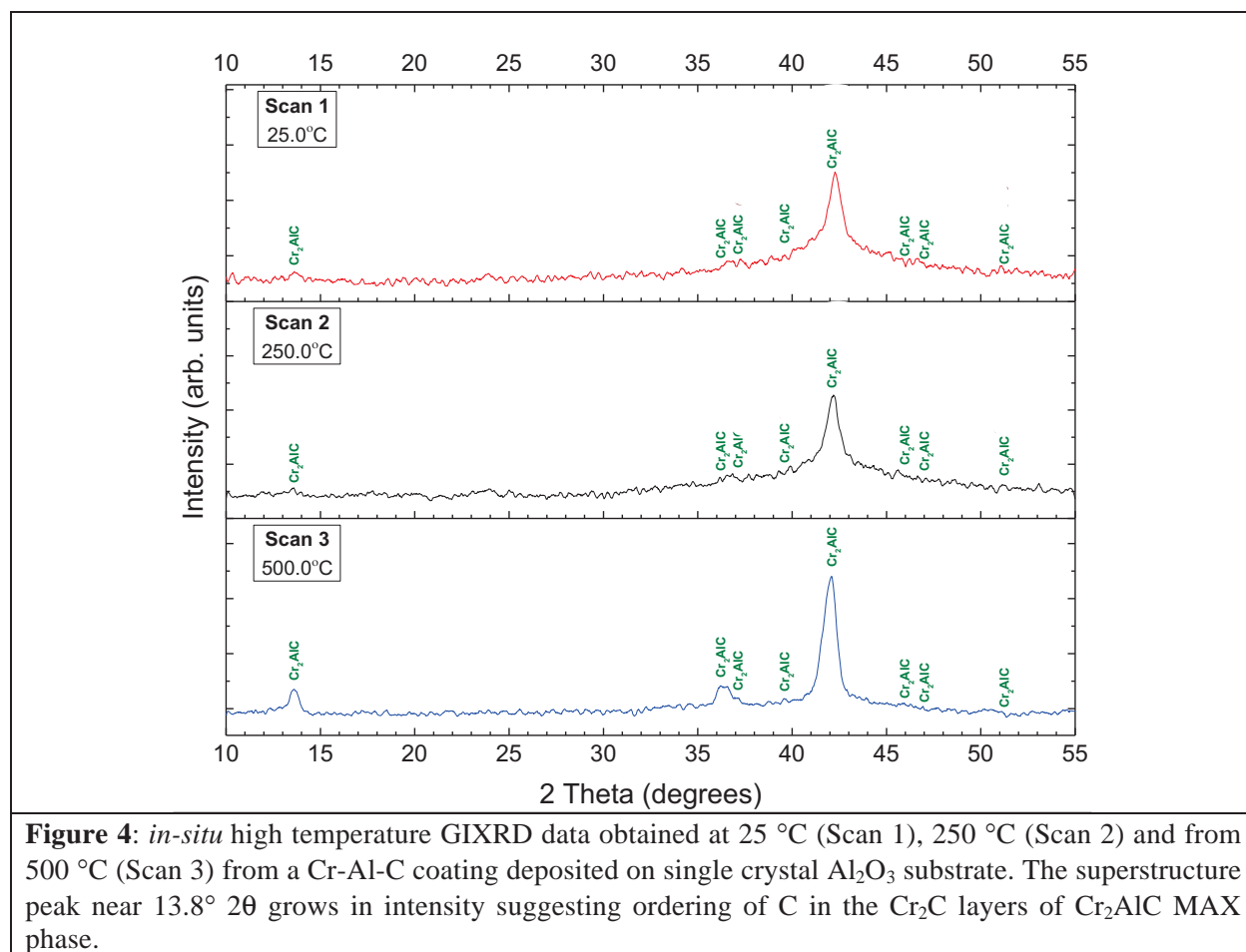

Figure 4: *in-situ* high temperature GIXRD data obtained at 25 °C (Scan 1), 250 °C (Scan 2) and from 500 °C (Scan 3) from a Cr-Al-C coating deposited on single crystal Al_2O_3 substrate. The superstructure peak near 13.8° 2θ grows in intensity suggesting ordering of C in the Cr_2C layers of Cr_2AlC MAX phase.

Figure 5 shows photographs obtained from the front and back sides of coated ZIRLO. Some defects in coatings are observed due to a reaction with the mounting base plates used to hold the ZIRLO substrates in the magnetron sputtering system.
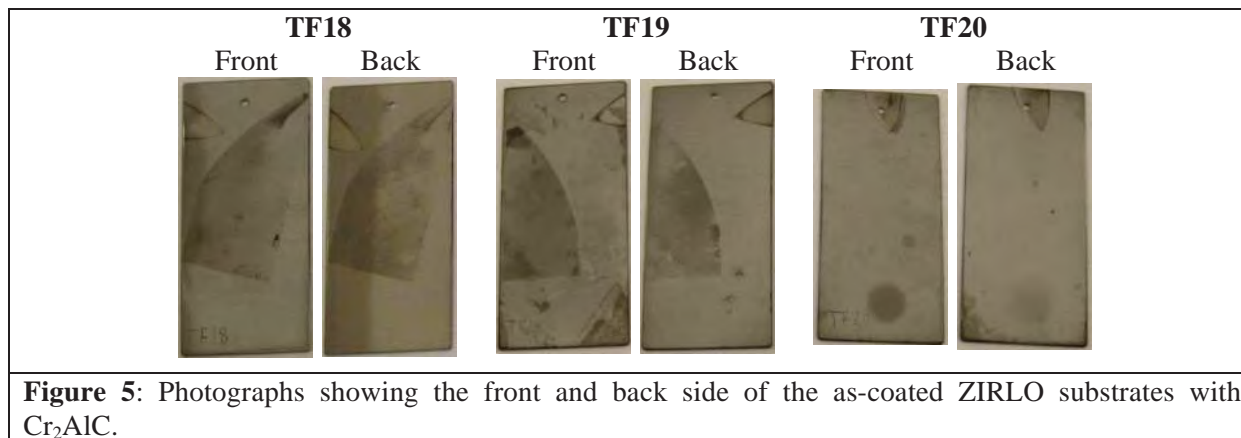
18

Figure 5: Photographs showing the front and back side of the as-coated ZIRLO substrates with Cr_2AlC.

Figure 6 shows GIXRD pattern obtained from the Cr_2AlC coating deposited on ZIRLO. Most of the diffraction peaks can be indexed to the Cr_2AlC MAX phase, however some secondary phases like Cr_2Al and Cr_7C_3 were also observed. In addition, the (002) peak is not distinctly observed.

Figure 6: GIXRD data obtained from as-deposited Cr_2AlC coatings on ZIRLO substrate.
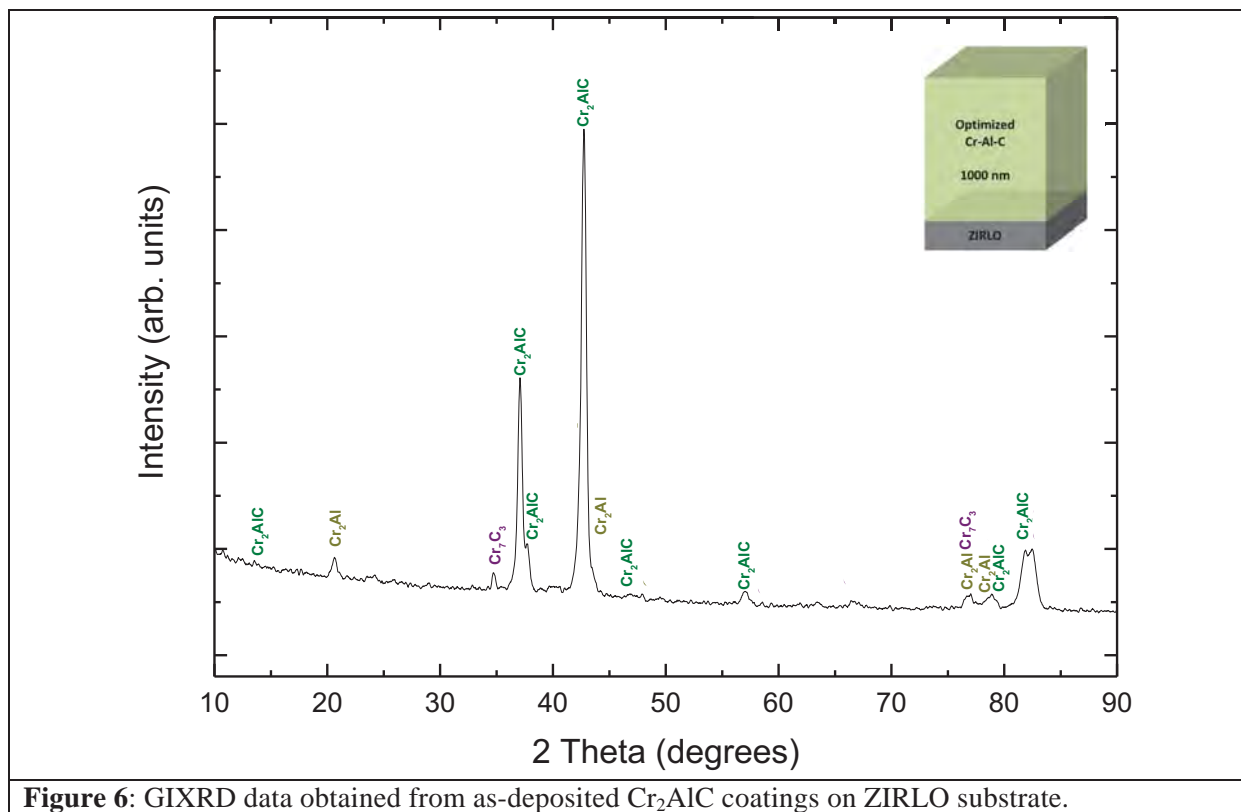
Autoclave corrosion tests were performed according to the ASTM G2 procedure on the ZIRLO substrates coated with Cr_2AlC for 10 days at 360 °C. **Figure 7** shows photographs of the coated samples after corrosion tests. One can see that some portions (darker colored regions) of the coatings had spalled during the corrosion tests, thus exposing the ZIRLO substrate beneath.

Figure 7: Photographs showing the front and back side of the coated ZIRLO substrates after autoclave tests.
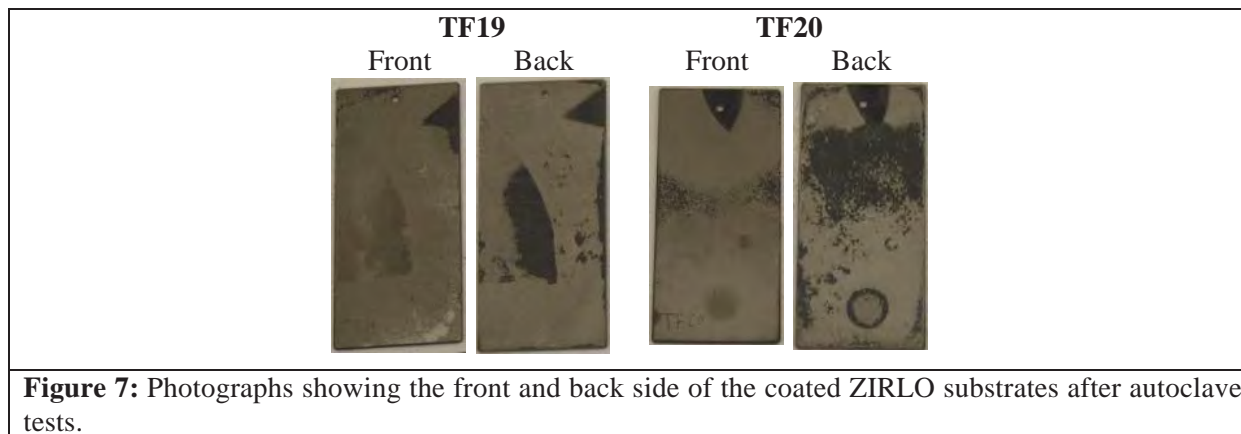
Table 2: Weight gain results from autoclave tests of ZIRLO coated with Cr_2AlC coatings.

Sample ID	Description	Weight Gain After 10 days [mg/dm^2]
TF19	Optimized Cr-Al-C/ ZIRLO	-0.3
TF20	Optimized Cr-Al-C/ ZIRLO	3.7
TF25	ZIRLO (control)	15.6

 Table 2 summarizes the weight gain results for coated and bare ZIRLO substrates. It can be seen that one of the samples (TF19) actually lost weight while the other (TF20) did not seem to have gained a significant amount of weight.

Figure 8 shows GIXRD data obtained from a darker region, marked with a rectangle shown in the inset photograph. The diffraction peaks in this pattern could be assigned to various corrosion products like Boehmite [AlO(OH)], ZrO_2, and Cr_2O_3.

Figure 8: GIXRD data obtained from Cr$_2$AlC coated ZIRLO substrates after autoclave tests. The data was obtained from the spot marked with a rectangle in the photograph shown. The coating at this spot is observed to have spalled during the autoclave test, thus exposing the ZIRLO substrate below.
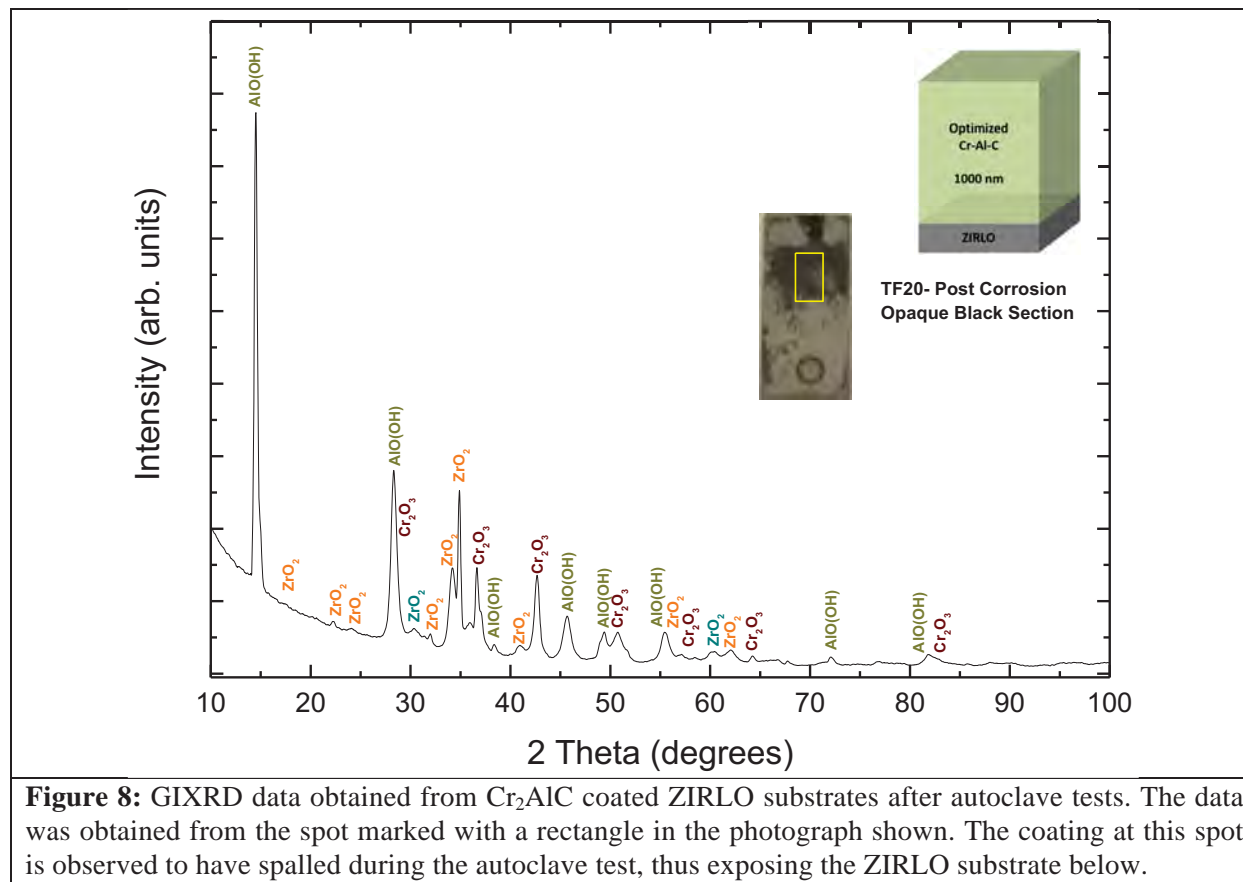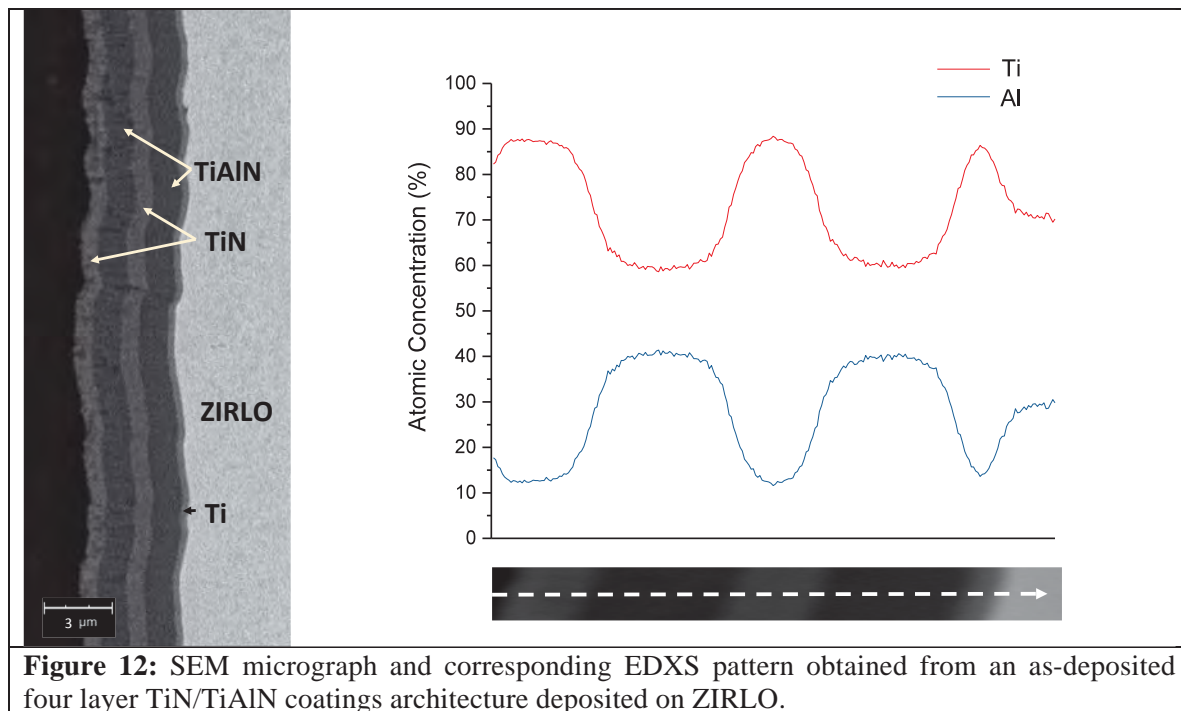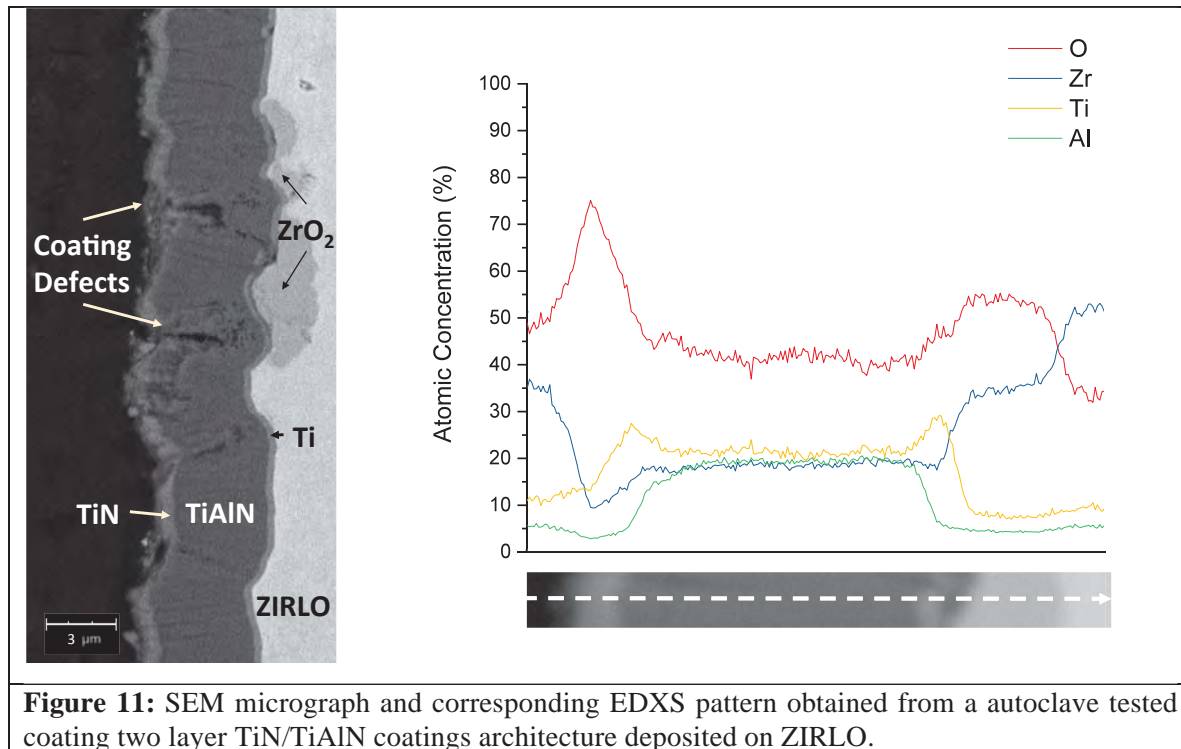
Figure 9 shows GIXRD data obtained from a brighter region, marked with a rectangle shown in the inset photograph. Interestingly, the peaks in this diffraction pattern could be assigned to Cr$_2$AlC and some ZrO$_2$ and Cr$_2$O$_3$. Thus, suggesting that in the regions where the coating survived it did provide some resistance to corrosion. The diffraction peaks related to ZrO$_2$ and Cr$_2$O$_3$ could also result through contributions from the neighboring regions. It can also be seen that the intensity of (002) diffraction peak for the Cr$_2$AlC phase in the corroded sample increased significantly with respect to the as-deposited coatings **(Figure 6)**. Thus suggesting an in-situ ordering of C in the Cr$_2$C layers during corrosion tests.
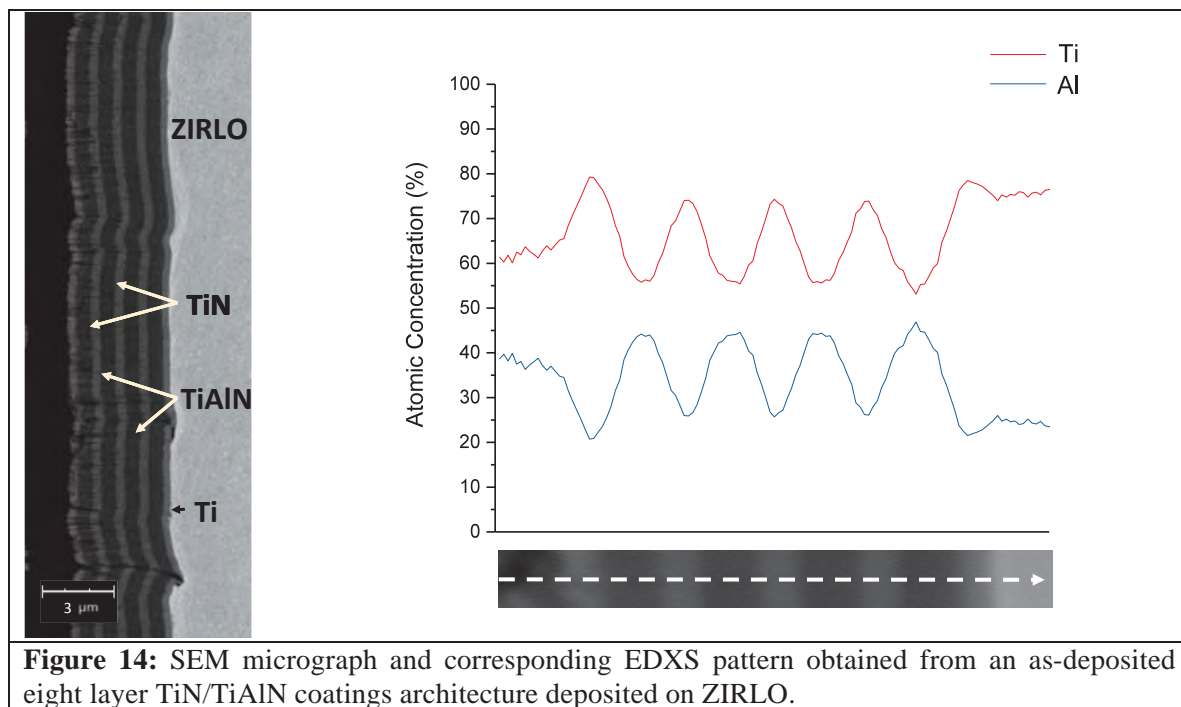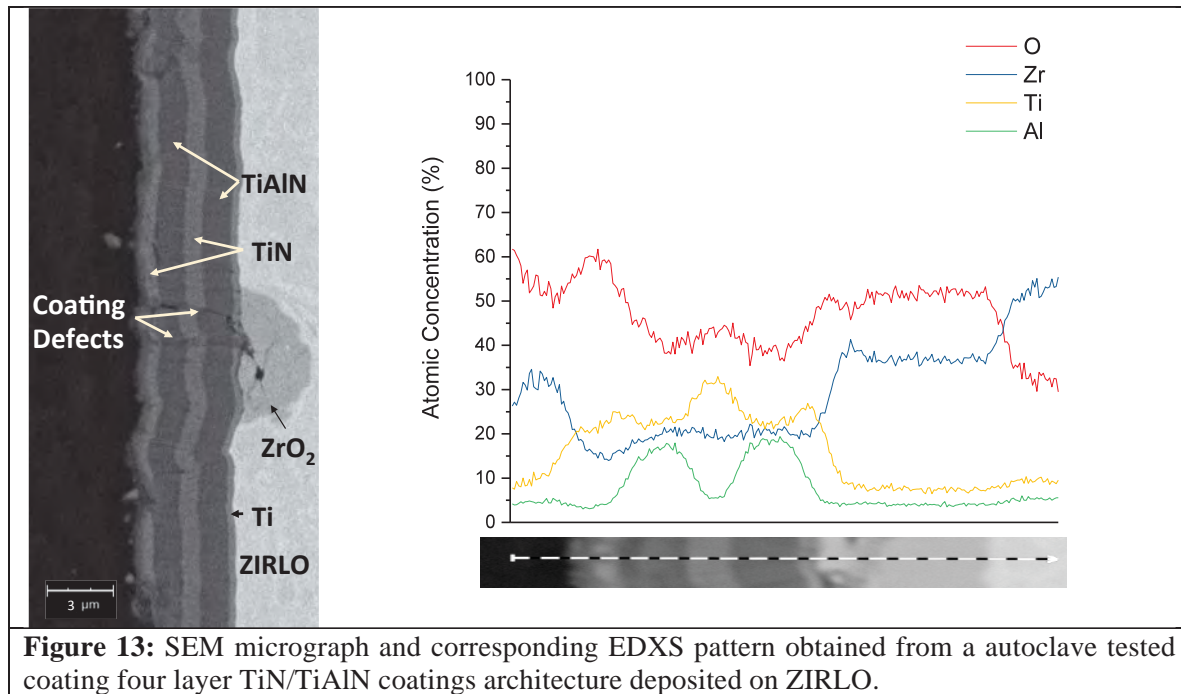
Figure 9: GIXRD data obtained from Cr_2AlC coated ZIRLO substrates after autoclave tests. The data was obtained from the spot marked with a rectangle in the photograph shown. The coating at this spot is observed to have survived during the autoclave test, thus protective the ZIRLO substrate below.
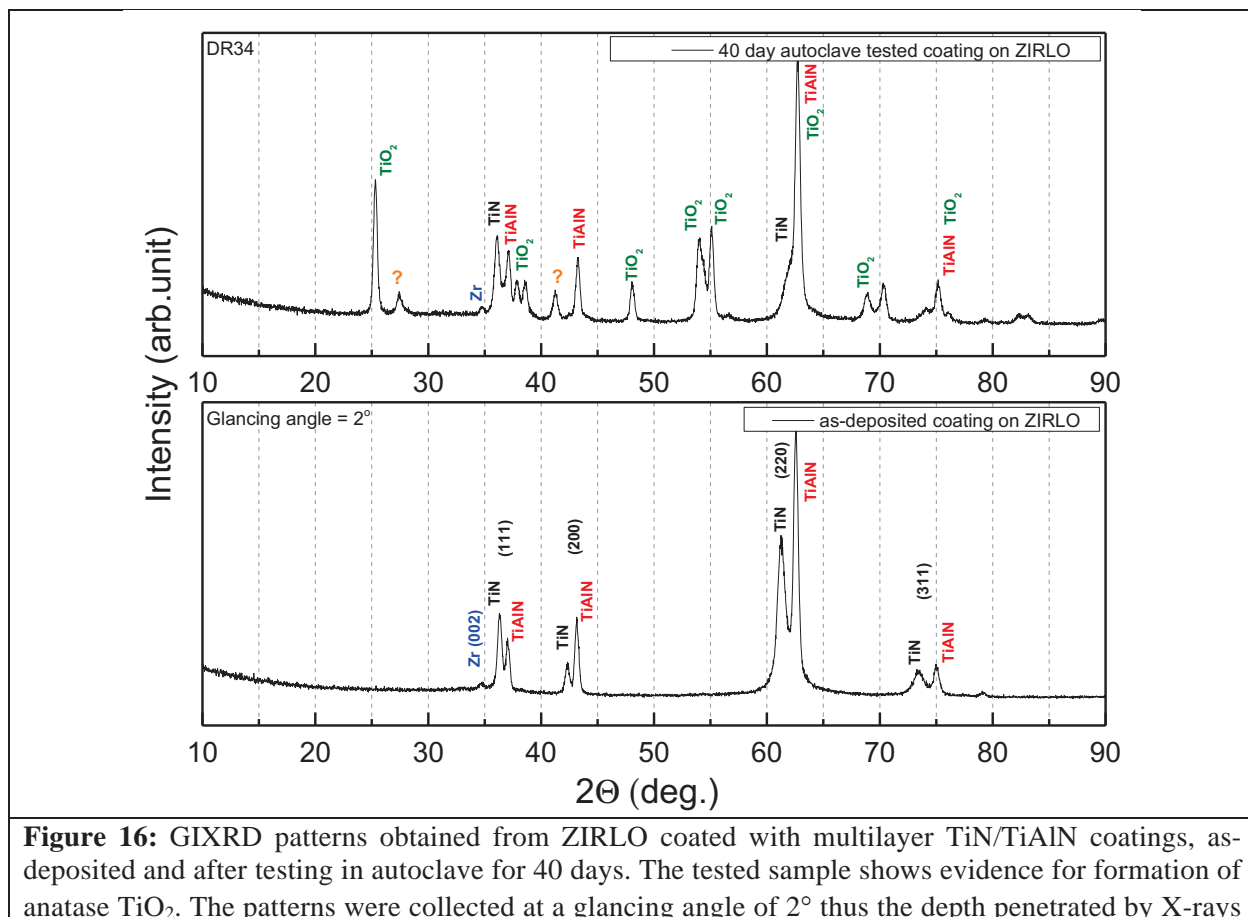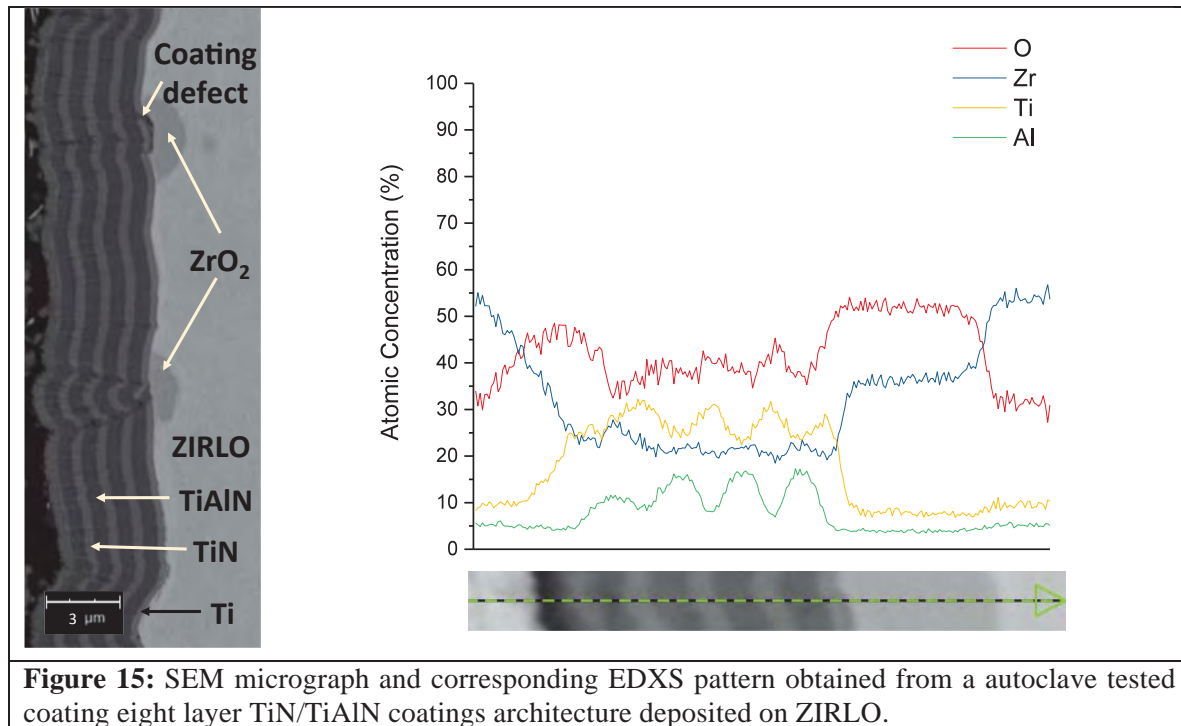
In the last year, the team at UTK focused on consolidating the work performed to study the microstructure of magnetron sputtered TiAlN coatings deposited on Zirlo and Si. The work comprised of characterizing these coatings before and after corrosion tests in an autoclave using scanning electron microscopy (SEM), energy dispersive X-ray spectroscopy (EDXS) and grazing incidence X-ray diffraction (GIXRD). The autoclave tests were performed at Westinghouse for a total of 40 days at 360 °C using the ASTM G2 standard procedure.

Four architectures consisting of single and multilayer TiN/TiAlN coatings were deposited using magnetron sputtering at PSU on ZIRLO substrates. The as-deposited coting architectures can be seen in **Figures 10, 12 and 14.** The coatings showed a columnar structure, this could also be concluded from one of the GIXRD patterns shown in **Figure 16.** The weight gain results shown in **Table 3** show that these coatings were very successful in preventing oxidation to a larger extent. **Figures 11, 13 and 15** show SEM and EDXS of coatings after autoclave tests. It can be clearly seen that the coatings failed at the places where there were even minor defects in the coatings. The corrosion products were identified using GIXRD **(Figure 16 and 17)** collected from to different depths from the surface of the coated substrates. The corrosion products are labeled in the GIXRD figures. A representative GIXRD patterns of bare oxidized ZIRLO is shown in **Figure 18.**
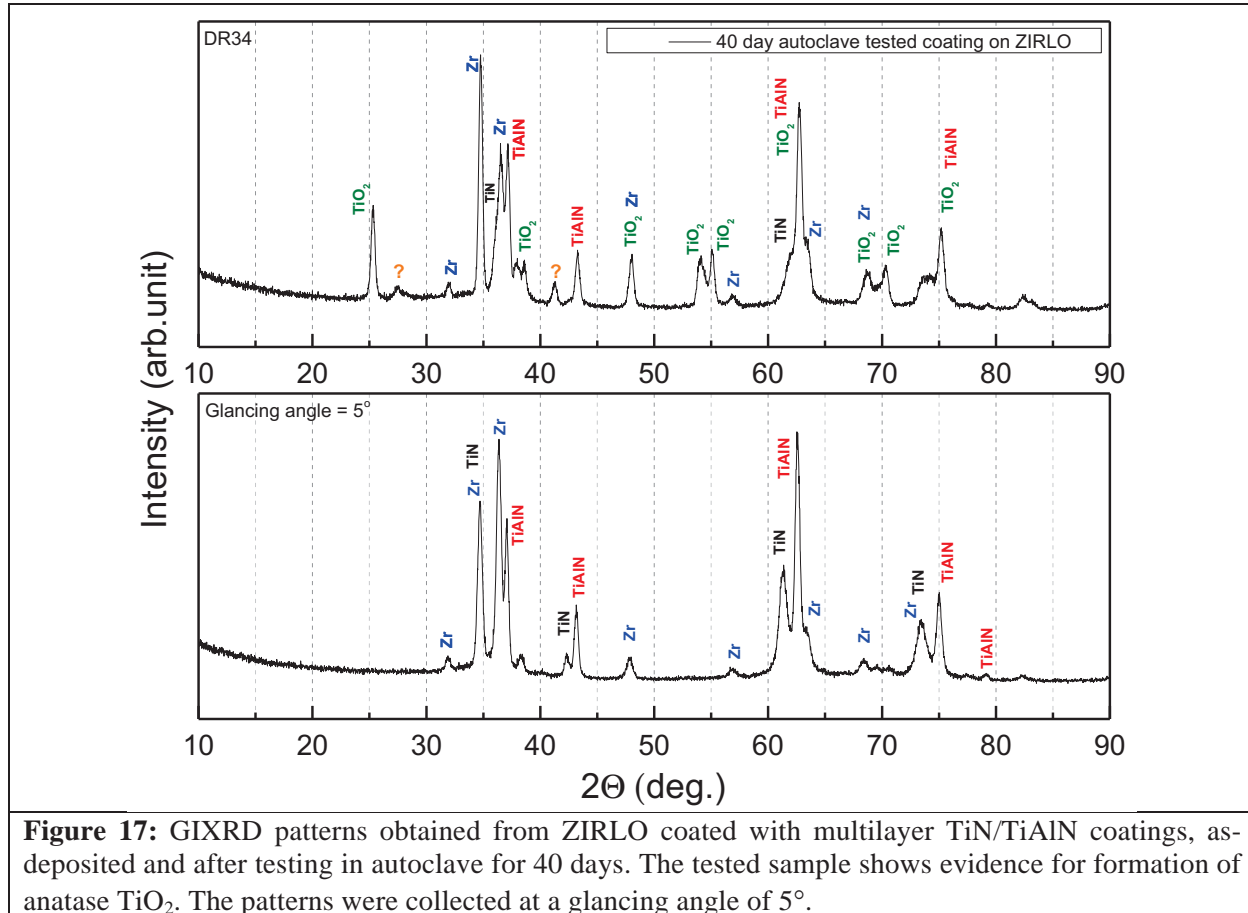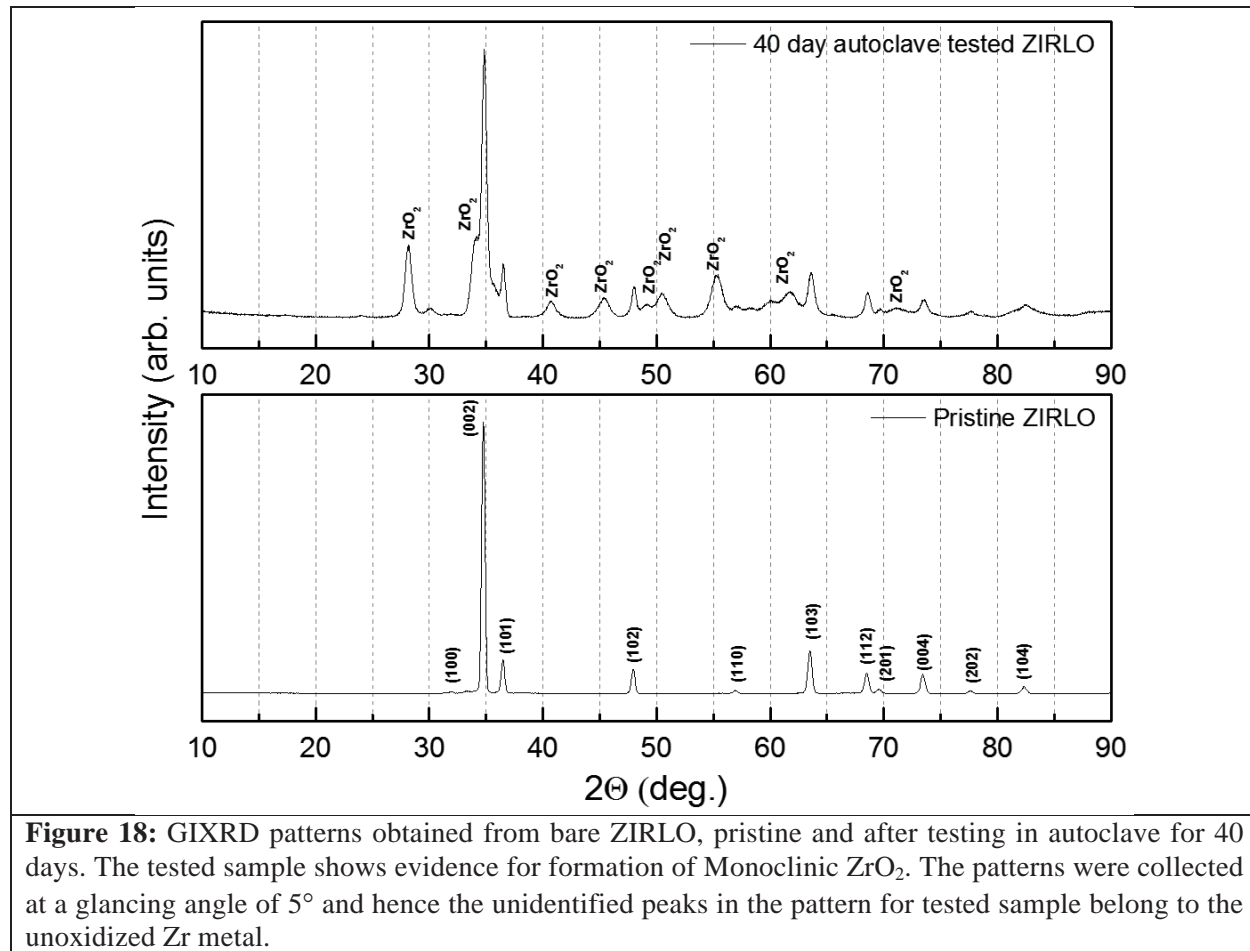

Figure 10: SEM micrograph and corresponding EDXS pattern obtained from an as-deposited two layer TiN/TiAlN coatings architecture deposited on ZIRLO.

Figure 11: SEM micrograph and corresponding EDXS pattern obtained from a autoclave tested coating two layer TiN/TiAlN coatings architecture deposited on ZIRLO.

Figure 12: SEM micrograph and corresponding EDXS pattern obtained from an as-deposited four layer TiN/TiAlN coatings architecture deposited on ZIRLO.

Figure 13: SEM micrograph and corresponding EDXS pattern obtained from a autoclave tested coating four layer TiN/TiAlN coatings architecture deposited on ZIRLO.

Figure 14: SEM micrograph and corresponding EDXS pattern obtained from an as-deposited eight layer TiN/TiAlN coatings architecture deposited on ZIRLO.

Figure 15: SEM micrograph and corresponding EDXS pattern obtained from a autoclave tested coating eight layer TiN/TiAlN coatings architecture deposited on ZIRLO.

Figure 16: GIXRD patterns obtained from ZIRLO coated with multilayer TiN/TiAlN coatings, as-deposited and after testing in autoclave for 40 days. The tested sample shows evidence for formation of anatase TiO_2. The patterns were collected at a glancing angle of 2° thus the depth penetrated by X-rays

barely reaching the unoxidized Zr metal.

Figure 17: GIXRD patterns obtained from ZIRLO coated with multilayer TiN/TiAlN coatings, as-deposited and after testing in autoclave for 40 days. The tested sample shows evidence for formation of anatase TiO$_2$. The patterns were collected at a glancing angle of 5°.

Figure 18: GIXRD patterns obtained from bare ZIRLO, pristine and after testing in autoclave for 40 days. The tested sample shows evidence for formation of Monoclinic ZrO_2. The patterns were collected at a glancing angle of 5° and hence the unidentified peaks in the pattern for tested sample belong to the unoxidized Zr metal.

Table 3: Results of weight gain after corrosion in an autoclave.

Sample	Description	Geometry	Length	Weight Gain (mg/dm^2)	
				10 days	**40 days**
DR19	TiAlN/Ti/ZIRLO	Strip	2.2010	9.8	15.7
DR20		Strip	2.2010	11.1	16.8
DR26	TiN(thin)/TiAlN(thick)/Ti/ZIRLO	Strip	2.2010	11.7	19.4
DR27		Strip	2.2000	11.5	19.0
DR34	(TiN/TiAlN 8-layer)/Ti/ZIRLO	Strip	2.2010	10.5	17.3
DR35		Strip	2.2010	10.6	16.7
DR50	(TiN/TiAlN 4-layer)/Ti/ZIRLO	Strip	2.2010	10.8	17.4
DR51		Strip	2.2010	10.8	17.7
TF21	ZIRLO (control)	Strip	2.202	15.7	25.1
T910-1	W Control 95-7067	Strip	1.107	16.0	25.0
T910-2		Strip	1.134	15.8	25.4
T910-3		Strip	1.091	15.5	25.2

III.   Summary of University of Michigan (UM) Experimental Research Accomplishments

The work at UM focused on assessing the corrosion behavior of multilayer TiAlN/TiN and monolithic Ti coated Zirlo tubes in a supercritical water (SCW) environment at 542 ˚C and 24.5 MPa. The coatings were deposited using CA-PVD technique. Femtosecond laser ablation was used to generate reproducible surface defects in some of the coatings. The corrosion behavior of coated Zirlo tubes in SCW environment and integrity of the coatings to protect the substrate are examined.

Materials and Methodology

Materials

The nominal chemical composition of the Zirlo tube used in this study is 1% Nb, 1% Sn, 300-600 wt. ppm Fe and balance Zr. The Zirlo tubes with two different coating architectures were used for corrosion studies; (a) 4 bilayers of TiAlN/TiN with Ti bond coat, and (b) TiN monolithic coating with Ti bond coat. The coatings were deposited using the cathodic arc physical vapor deposition (CA-PVD) technique. The cathodes used in the CA-PVD were, (a) 99.999% elemental Ti for bond coat/TiN layer and (b) TiAl (33 at% Ti – 67 at% Al) for the TiAlN deposition. Further details of deposition process and parameters are explained in another publication [14].

Methodology

Femtosecond Laser Ablation

A Ti: Sapphire laser system (Clark-MXR CPA-2001) provided 780 nm wavelength pulses with 150 fs pulse duration. All irradiations were conducted at a repetition rate of 1 kHz. A fast mechanical shutter controlled the number of pulses arriving on each irradiation spot with a ±3 pulse accuracy. The spot size of the beam at focus was measured using a WincamD infrared camera. The focused Gaussian beam has an effective spot size of 20 μm. Beam fluence in this experiment is defined as the fluence at pulse peak. Samples were clamped onto a customized holder attached to an electromechanical stage with a position accuracy of 0.5 μm.

Optimization of the laser ablation parameters were conducted on both the multilayer coating and monolithic TiN coating. The optimization was done in terms of laser fluence and number of shots required to generate smooth and reproducible defects exposing the substrate. Using the optimized laser parameters (0.75 J/cm^2 and 275 pulses), a total of nine craters were created on each tube sample: 3 craters located at 2 mm from each end of the cylinder and 3 craters at the center of the cylinder (all linearly arrayed). A representative laser ablated zone with elemental mapping on the multilayer coating is shown in figure 1. Figure 1a shows appearance of multiple ablation zones with similar laser parameters demonstrating the reproducibility of the craters. Figure 1b shows the morphology around one of the ablated spots and figures 1c to 1f present elemental mapping around spot. Multiple ablations were carried out at the same fluence and

number of shots and the resulting crater depth was determined to be similar at 13±1 μm indicating reproducibility of the generated defects.
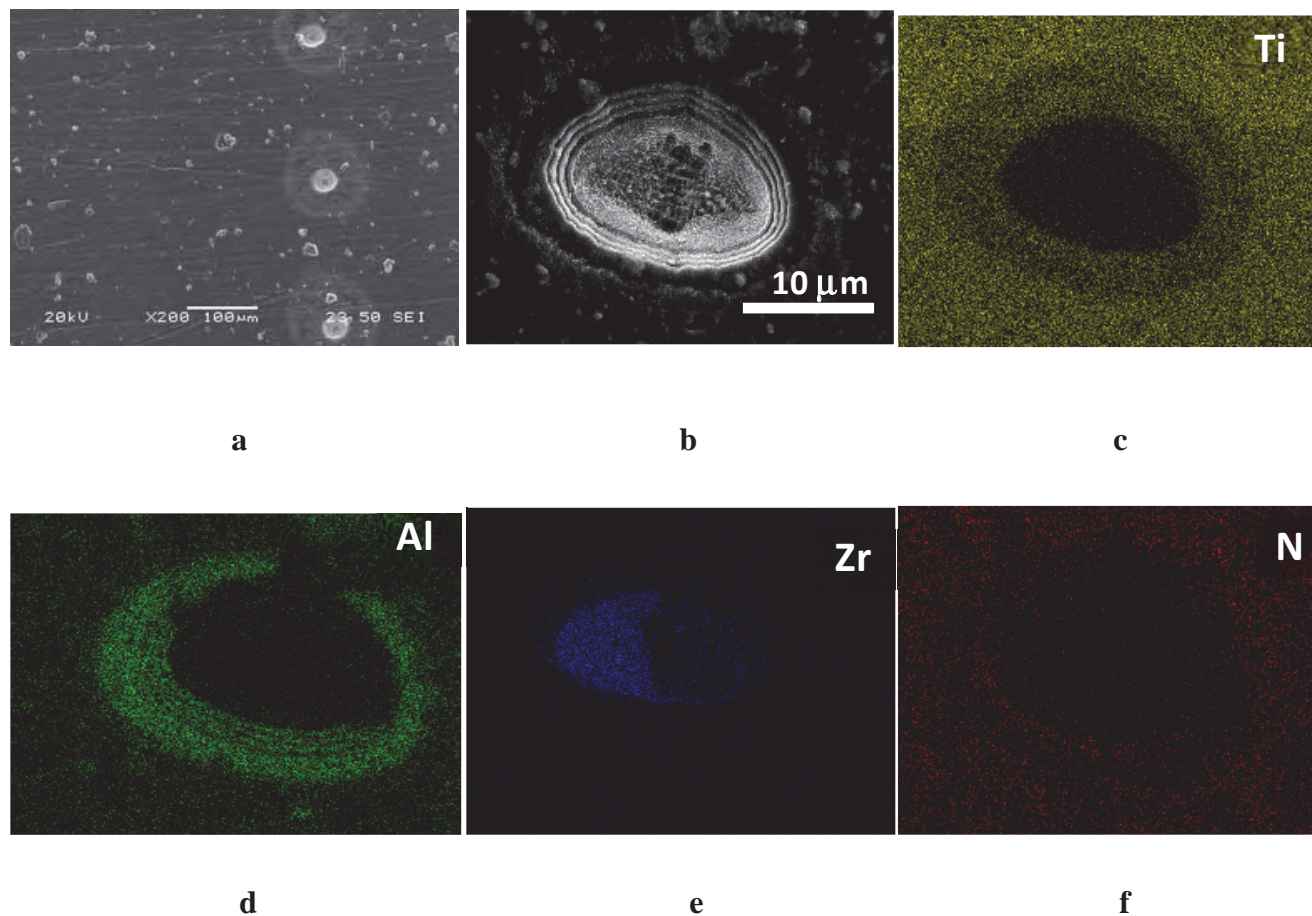

Figure 1. Morphology and elemental mapping of ablated zone in a 4 bi-layer TiAlN/TiN coating on Zirlo tube generated using a laser fluence of 0.75 J/cm^2 with 275 shots (a) multiple ablated spots with same fluence, (b) morphology around a laser ablated spot and (c)-(f) elemental mapping around the spot.

Corrosion Experiment

Tube samples, both coated (with and without laser-induced defects) and uncoated Zirlo, were exposed in pure supercritical water (SCW) environment at a temperature 542 ˚C and pressure 24.5 MPa for a duration of 48 hours. The experiment was conducted in a 2-liter autoclave made of Inconel 625 attached to a recirculation loop while maintaining a flow rate of ~40 ml/min. The dissolved oxygen (DO) level was maintained at < 10 ppb by purging with high purity argon gas. The conductivity remained at <0.1 μS/cm inlet and <2 μS/cm outlet throughout the duration of the experiment. The tubes were suspended in a custom made sample tree (made of Inconel 625) at the center of the autoclave. The base of the tubes rested on a hollow ceramic washer, and a Ni wire with ceramic sheaths through the tube was used to suspend it from the branch. The

thermocouple was positioned to read temperature at the middle branch of the sample tree. It should be noted that the variation of temperature between branches of the sample tree from top to bottom was less than 0.5 ˚C.

Characterization

The weights of the tube samples before and after exposure to SCW were measured using a digital balance with an accuracy of 0.01 mg. An average of three weight gain readings were taken and weight gain is reported per unit surface area in mg/dm^2.

Scanning electron microscopes (SEM); a Philips XL30 field emission gun (FEG), a JEOLJSM-6480 and FEI Helios 650 nanolab, all equipped with x-ray energy dispersive spectroscopy (EDS) were used for characterization of the coating morphology on the surface and cross section. Elemental mapping across the coating layers before and after oxidation and composition along defects was achieved using energy dispersive x-ray (EDS). The cross sections were prepared by mounting in epoxy resin followed by grinding and polishing and subsequently sputter depositing a thin gold layer to increase surface conductivity. TEAM Basic EDAX software was used for EDS mapping and line scans. The top TiO_2 layer post oxidation of coated tubes was measured after fibbing a cross section using Helios nanolab. The oxide thickness for ZrO_2 on the tube outer diameter (OD) underneath the coating and ID was measured using SEM images. The ZrO_2 and TiO_2 thicknesses measured from SEM images were then converted to equivalent weight gain in mg/dm^2 using densities of 5.68 g/cm^3 and 4.23 g/cm^3, respectively. The laser ablated zones were characterized using optical and laser confocal microscopy. The morphology and composition of laser ablated zones was characterized using SEM-EDS. Laser Raman spectroscopy with a 532 nm laser was used to establish the surface oxide structure after exposure.

Results and Discussion

Weight gain post SCW exposure

The tubes coated with 4 bilayers of TiAlN/TiN and Monolithic TiN coating were exposed to the SCW environment at a temperature of 542 ˚C and pressure 24.5 MPa for a duration of 48 hours. Uncoated Zirlo tubes were also included in the exposure as control specimens. Two coated tubes each with laser ablated defects and without them were exposed. Figure 2 summarizes the oxidation weight gain data after exposure.

Three important observations from the figure are: (a) the coated tubes exhibited significantly higher weight gain than the uncoated Zirlo tubes, (b) for a given coating the difference between weight gain between laser ablated and unablated tubes in minimal and (c) The monolithic TiN coated tube showed a slightly lower weight gain than the multilayer coated tubes. The next section will present observations on morphologies and composition of surface and cross sections before and after exposure and oxide thicknesses.
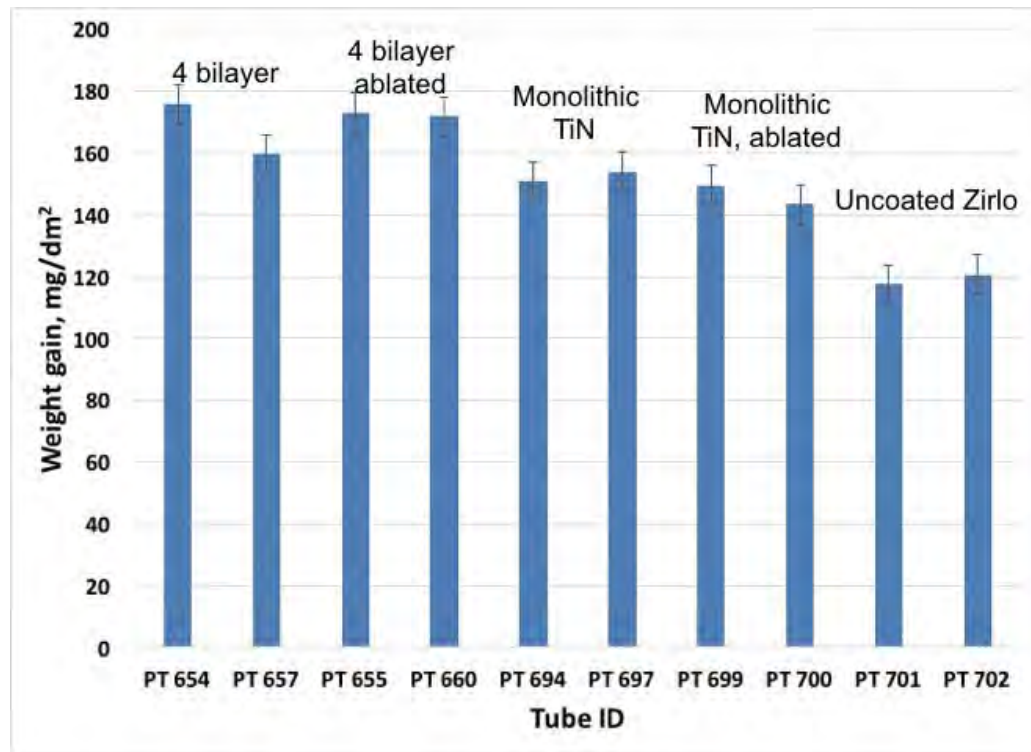
Figure 2. Weight gain values for uncoated Zirlo, Zirlo coated with 4 bilayers of TiAlN/TiN, and Zirlo coated with a TiN monolithic layer with and without laser ablation after exposure to SCW environment.

Characterization of coating architecture

The surface of the coated tube and the architecture of coating layers deposited by CA-PVD technique for four bi-layers of TiAlN/TiN is shown in figure 3. Figure 3a presents the surface morphology of the as-coated tube; while figure 3b-d show the individual layers in the cross sectional micrographs. The as-coated tube was found to contain numerous macro-particles on the surface (figure 3a). The number density of these macro-particles was calculated from multiple SEM images over the tube surfaces. The resulting number density was 3176 m^{-2}, yielding an average inter-particle distance of ~18 μm. Figure 3b shows a representative cross section of the layers describing the coating architecture in which the four alternate bi-layers of TiAlN/TiN , bond coat of Ti, and the top layer TiN layer are clearly visible. The macro-particles observed in Fig. 3a have their origin on the Zirlo surface. Note the particles in the bond coat in images in Figures 3c and 3d. These particles cause a distortion of subsequent layers that propagates to the surface as shown in the cross sectional images in figures 3c and 3d. The particles likely originate from release of chunks of Al (Fig. 3d) or Ti (Fig. 3c) during sputtering to form the bond coat or the first TiAlN layer in the CA-PVD process. Elemental composition maps presented in subsequent sections (figure 5-6) demonstrate these origins better.
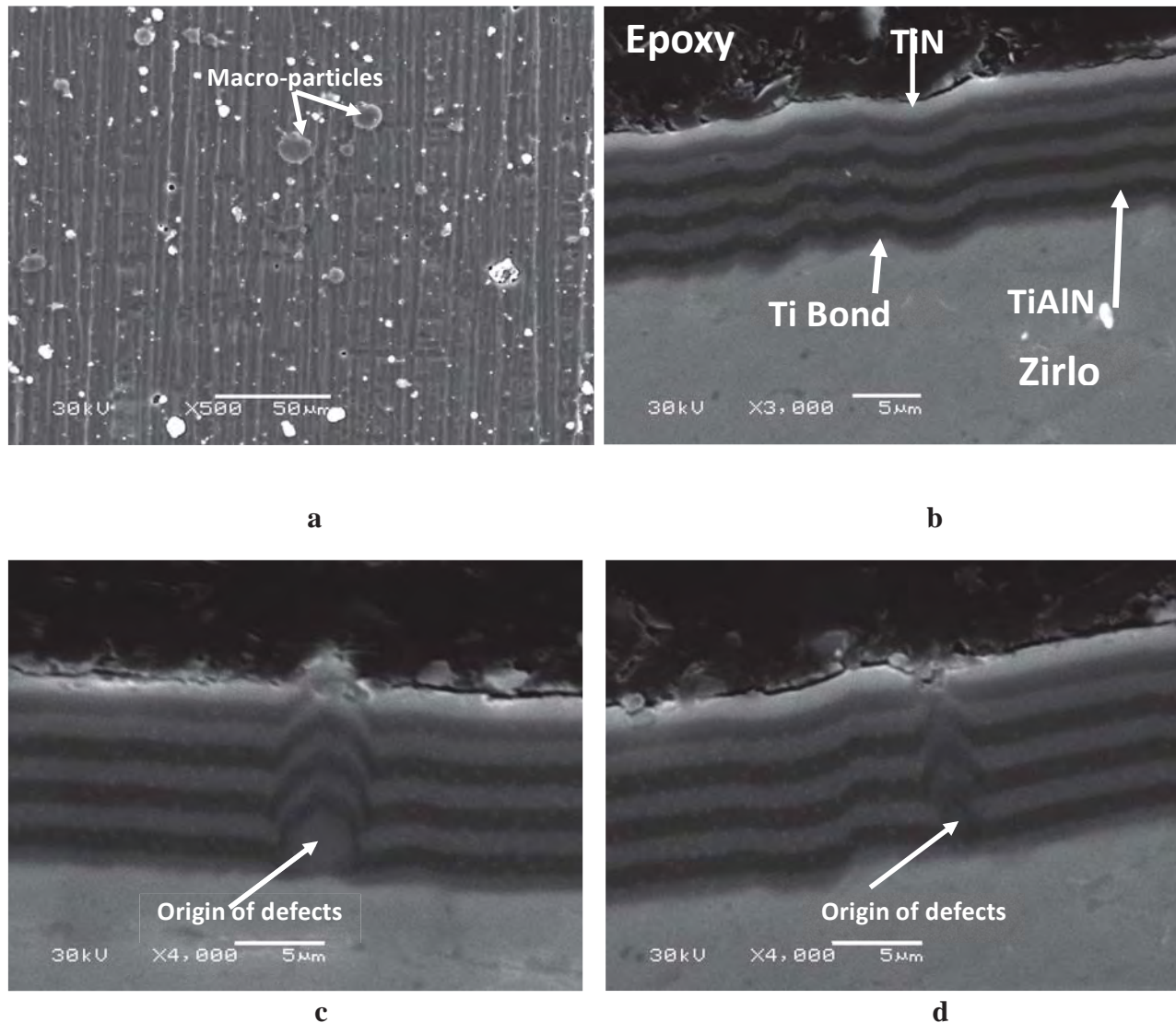
Figure 3. The morphology coating for as-coated tube PT 653 (a) surface appearance and (b) to (d) cross-sectional appearance.

Coating morphology post oxidation

The surface morphology of the four bi-layer coating after exposure to SCW is shown in figure 4. The macro-particles are apparent after exposure, albeit oxidized, as shown in figure 4a. The average inter-particle distance, size of these particles and overall morphology remains similar to that before exposure. In addition to the macro-particles, there is also evidence of cracks on the oxidized surface as shown in figure 4b. The coefficient of thermal expansion (CTE) for TiAlN has been reported to be 7.5×10^{-6} while that for TiN is 9.4×10^{-6}. [12-14] The mismatch of CTE for the alternate layers of TiAlN and TiN might have contributed to the formation of cracks while cooling from a temperature of 542 ˚C. The CTE for Zirlo (6.3×10^{-6}) is significantly lower than

that for either TiN and TiAlN and would contribute to additional tensile stresses in the layers upon cooling. Both the macro-particles and cracks are observed to extend through all the layers down to the bond coat. Figure 4c is an example of a crack extending all the way to the bond layer. Some particles have cracks associated with them as shown in figure 4d.
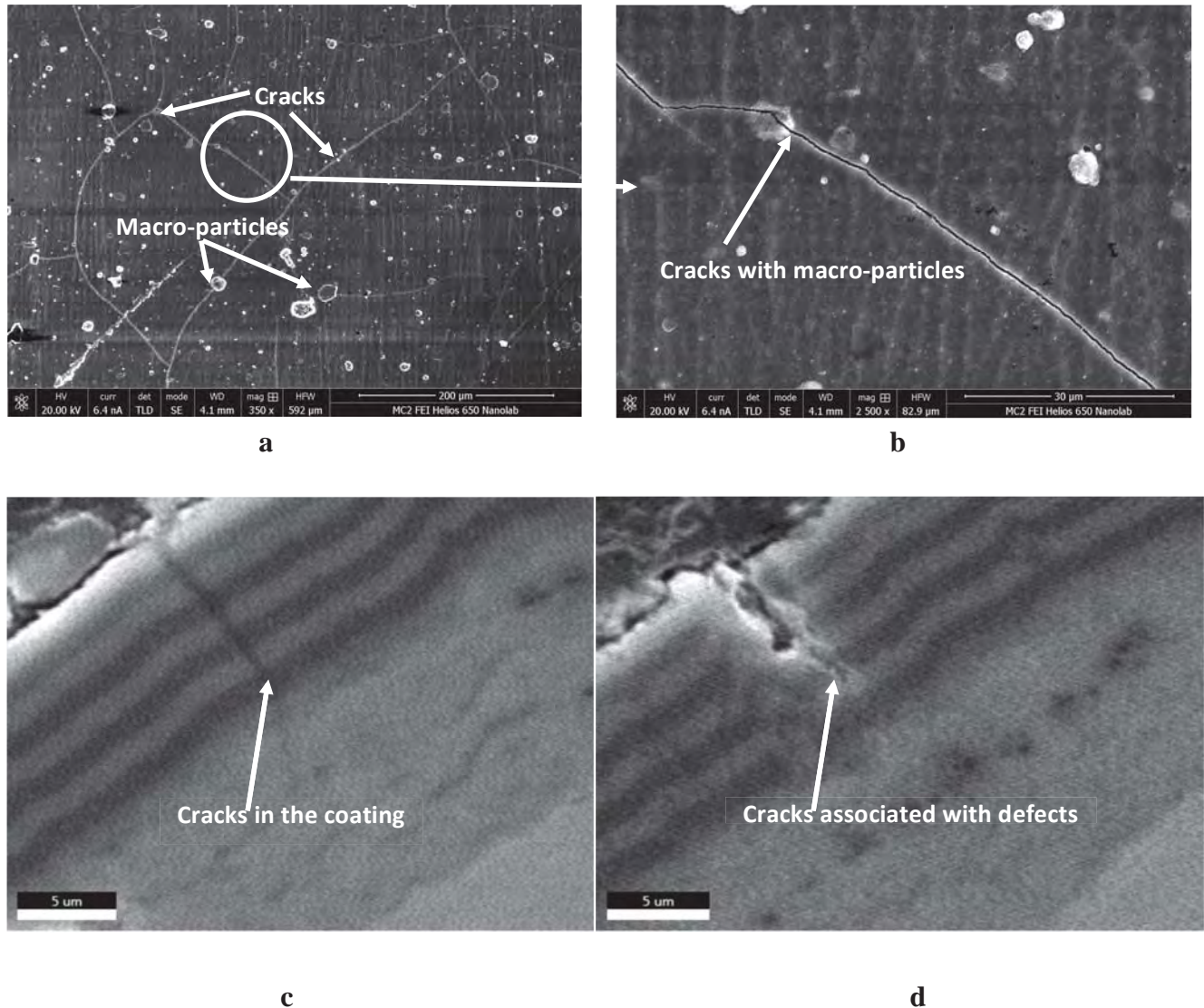
Figure 4. The morphology post exposure to SCW for tube PT 655 showing the oxidized macro-particles and presence of cracks on the surface.

Elemental mapping of the oxidized multilayer coated tube around the macro-particles in tube PT 655 is shown in figures 5 and 6. Figure 5 is an example of an Al-rich (Ti-deficient) macro-particle originating at the coating-substrate interface. Conversely, figure 6 shows an example of a Ti-rich (Al-deficient) macro-particle originating from a thicker Ti bond coat.
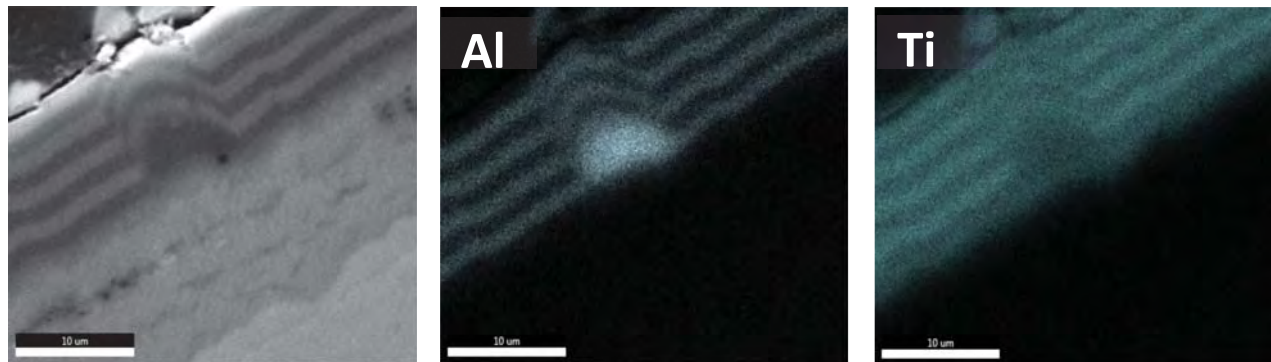
Figure 5. Elemental mapping of 4 bilayer TiAlN/TiN coated Zirlo tube (PT 655) after exposure to SCW environment at 542 ˚C for 48 h deposition of Al chunk resulting in macro-particle.
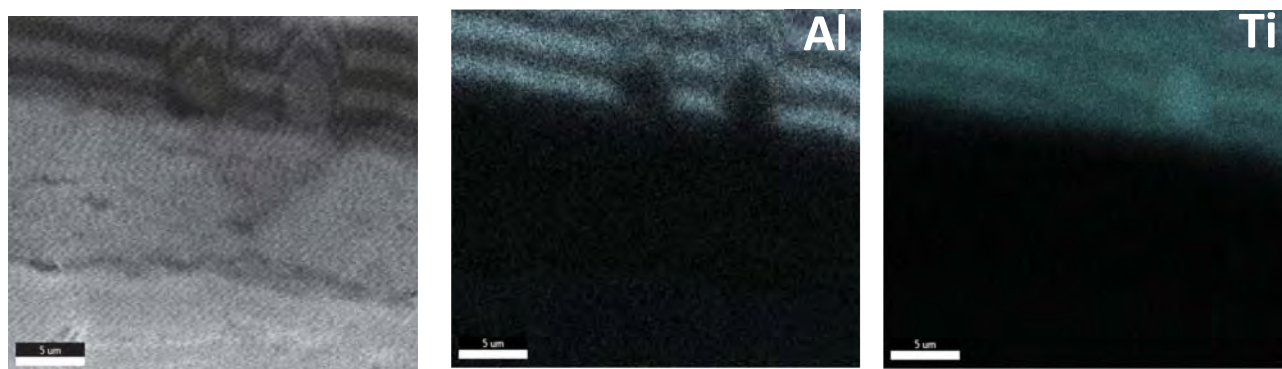
Figure 6. Elemental mapping of 4 bilayer TiAlN/TiN coated Zirlo tube (PT 655) after exposure to SCW environment at 542 ˚C for 48 h; showing thicker Ti bond resulting in macro-particle.

The top surface in both the multilayer and monolithic Ti coated tubes showed a thin layer of titanium oxide as shown in figure 7. Figure 7a and 7b show the cross section of multilayer coated tube and TiN coated tube, respectively, after oxidation. Figure 7c and 7d show the corresponding Raman spectra on the top oxide surface. The spectra clearly reveal both rutile and anatase phases of TiO_2. The surface oxide formed over the coating is about 0.5 µm thick and is uniform.
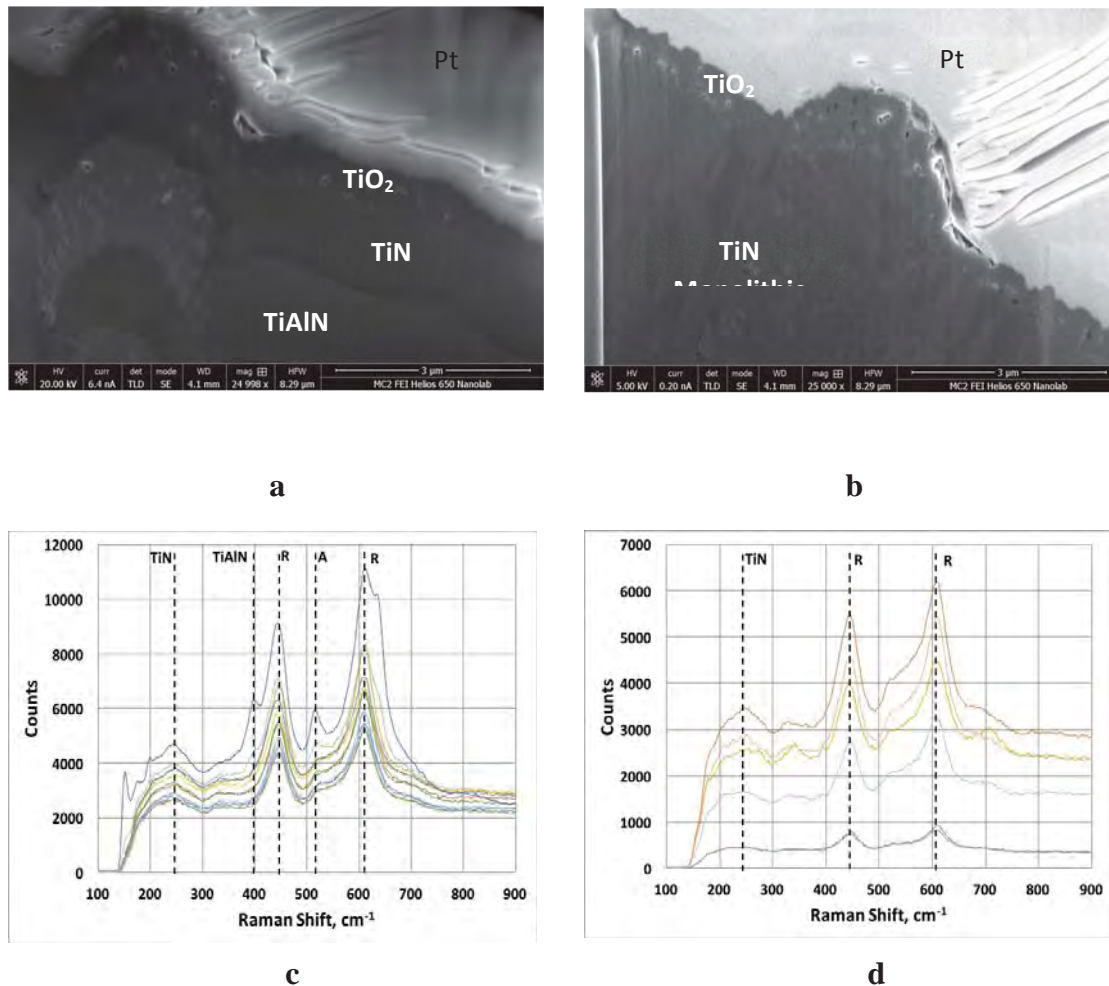
Figure 7. The cross section of (a) 4 bilayer coated Zirlo tube PT 655, (b) TiN monolithic coated Zirlo tube PT 700 after oxidation and Raman spectra on oxidized surface for (c) PT 655 and (d) PT 700.

Oxidation of tube OD beneath the coating

The data in Figure 2 show that the weight gain of the coated tubes was greater than that of the uncoated tubes. Except for the thin titanium oxide layer on the TiN top layer, the coating should have prevented oxidation of the outer Zirlo surface, yielding a weight gain of approximately half that of the uncoated tube. Cross sections of the multilayer coating and underlying Zirlo, in figure 8 show that, in fact, significant oxidation of the Zirlo occurred beneath both the multilayer and the monolithic TiN coating. Figures 8a and 8b show the oxide layer below the multilayer coating and the TiN coating, respectively, and Figure 8c shows the oxide on the uncoated tube ID.
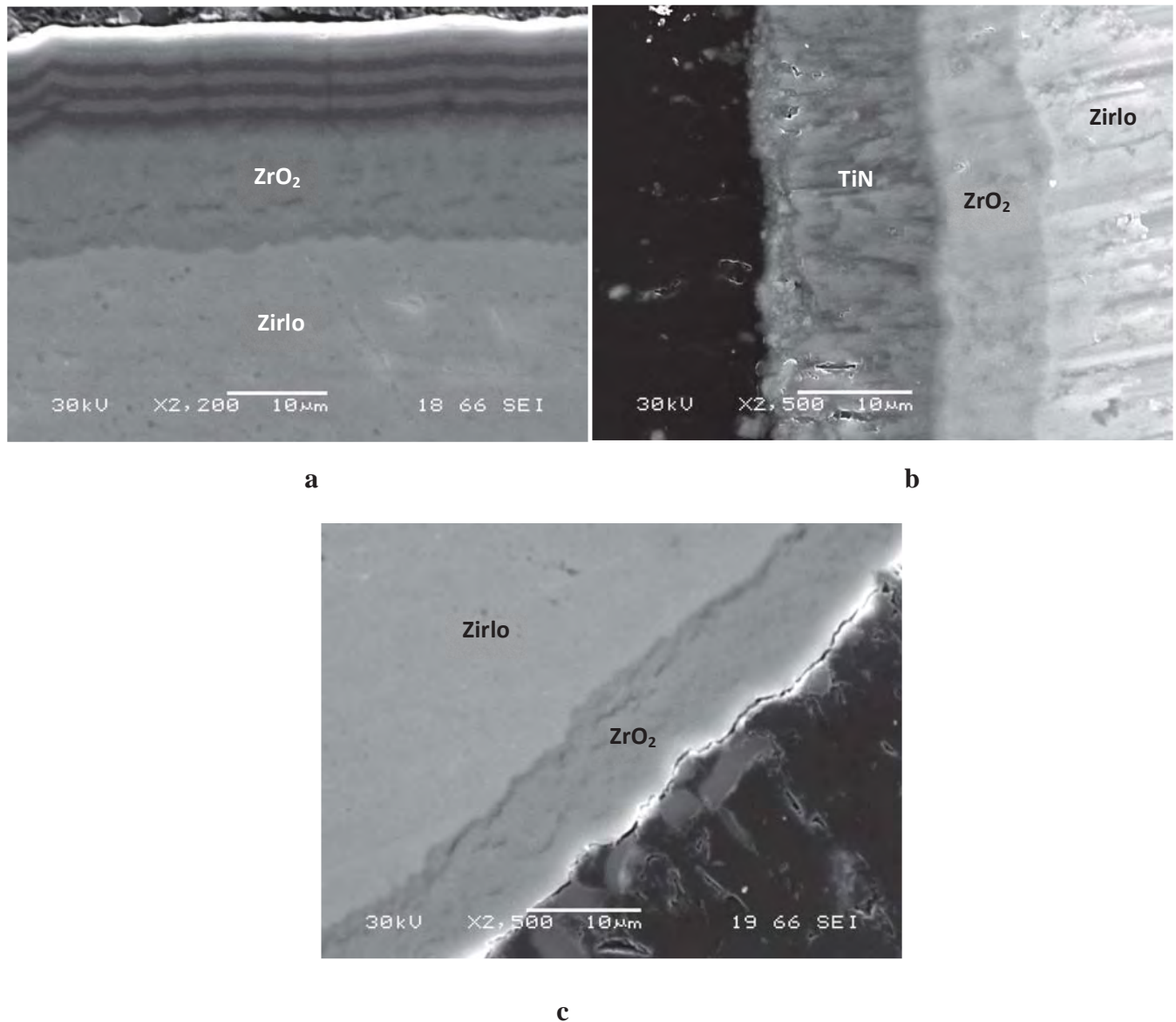
Figure 8. The morphology of ZrO_2 layer (a) on the tube OD beneath the multilayer coating, (b) on the tube OD underneath TiN monolithic coating, and (c) on the uncoated tube ID.

A summary of the thickness data and the weight gains measured and weight gain values calculated from thickness values along with the stoichiometry of oxides is given in table 1. The estimated weight gain values from thicknesses are slightly lower compared to the values measured following autoclave exposure, but fall in the same order as the thickness. Note that the thickness of the ZrO_2 layer beneath the coating is as thick as that on the ID of the tubes. Furthermore, the oxide layer beneath the coating was of uniform thickness, indicating that the coatings provided essentially no protection of the underlying Zirlo from the environment. This

could only be possible if the coating was highly defective. The defects are likely the macro-particles that resulted in distortion of the layers and cracking in the perturbed regions. EDS line profiles of oxygen were taken across the region above the particles and one such profile is shown in figure 9. The profile clearly demonstrates enhanced oxygen levels around the particles as compared to the flat region of the coating layers. So, these macro-particles can be considered to be preferential sites for oxygen access to the substrate. The diffusion coefficient for oxygen in zirconium oxide has been reported to be about 10^{-11} cm^2/sec at 542 ˚C and 10^{-13} cm^2/sec at 360 ˚C [33]. For a diffusion coefficient of 10^{-11} cm^2/sec, an exposure of 48 hours would result in a diffusion length of oxygen of about 13 μm assuming parabolic oxidation kinetics. Thus, the thickness of the observed oxide layer beneath the coating is consistent with rapid penetration of oxygen through the coating and growth of the zirconium oxide by solid state oxidation. For a macro-particle spacing of 18 μm, each particle has an associated area of radius 9 μm if uniformly distributed. That this effective "diffusion length" corresponds with the range of oxide thickness may explain why the oxide underneath the coating is so uniform in thickness. That is, the defect spacing is small enough that oxide growth at the base of the defects merges to form a continuous layer. Similar observations were made on magnetron sputtered multilayer coating at lower temperatures (360 ˚C). In this case, the substrate oxidation was localized to the sites of these macro-particle forming oxides that emerged from the point of the defect to a depth of ~ 2 μm while the rest of the Zirlo was unoxidized [34]. These results are consistent with a diffusion coefficient that is two orders less than that at 542°C. For the CA-PVD multilayer coated Zirlo, the substrate was not shown to oxidize in 360 ˚C water resulting in much lower weight gain [12-14].

It was also observed that there was no significant difference in the weight gain between ablated and unablated tubes. The defects on the coating before and after exposure to SCW environment are shown in figure 10. The defects did not spread beyond the original defect size. No delamination or enhanced oxidation was observed around the defects. The reason that they did not contribute to the oxidation is that the high number density of intrinsic coating defects provided sufficient access of oxygen to the Zirlo so that any additional contribution from the laser ablated regions was negligible.

Table 1. Summary of oxidation behavior of uncoated Zirlo and Zirlo coated with 4 bilayers of TiAlN/TiN and monolithic TiN with Ti bond coat in SCW environment at 542 ˚C

Tube ID / description	Weight gain, mg/dm^2 (measured)	Oxide thickness (µm)			Oxide composition (at %)			Weight gain, mg/dm^2 (from thickness)
		OD ZrO$_2$	ID ZrO$_2$	Top TiO$_2$	OD Zr:O	ID Zr:O	Top Ti:O	
PT 701 / uncoated Zirlo	117.4	7.98	7.88	NA	32:68	32:68	NA	116.9
PT 655 / coated 4 bilayer TiAlN/TiN	172.9	10.4	9.33	0.56	44:56	43:57	43:57	156.3
PT 700 / coated Monolithic TiN	143.4	8.12	9.4	0.55	42:58	45:55	43:57	133.9
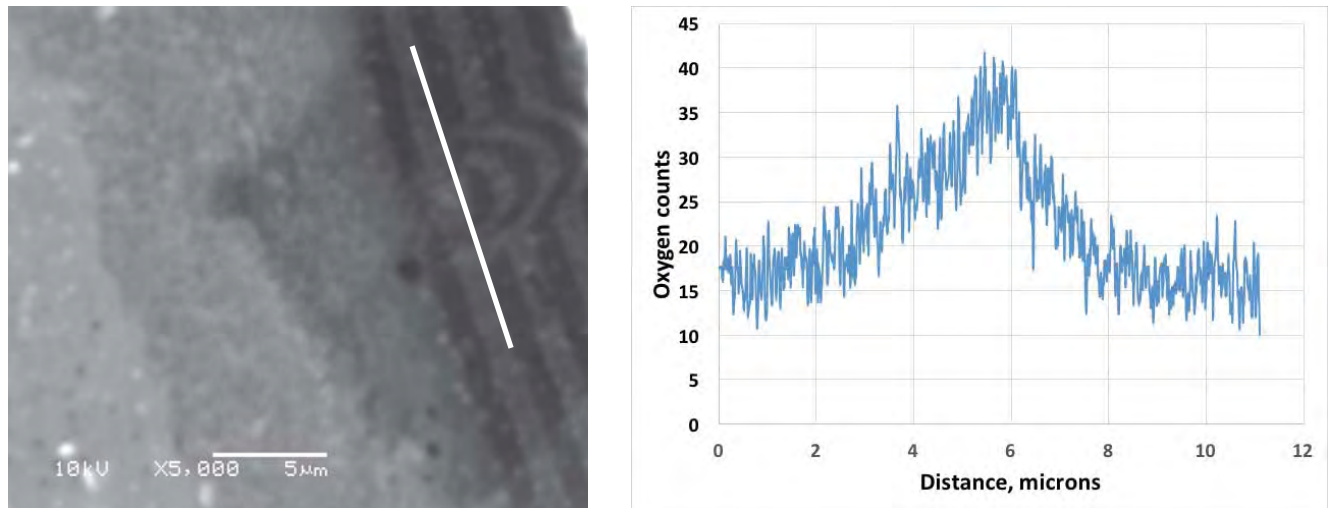
Figure 9. Oxygen conc. profile using SEM-EDS along a macro-particle in oxidized 4 bilayer coated Zirlo tube PT 655.

a   **b**
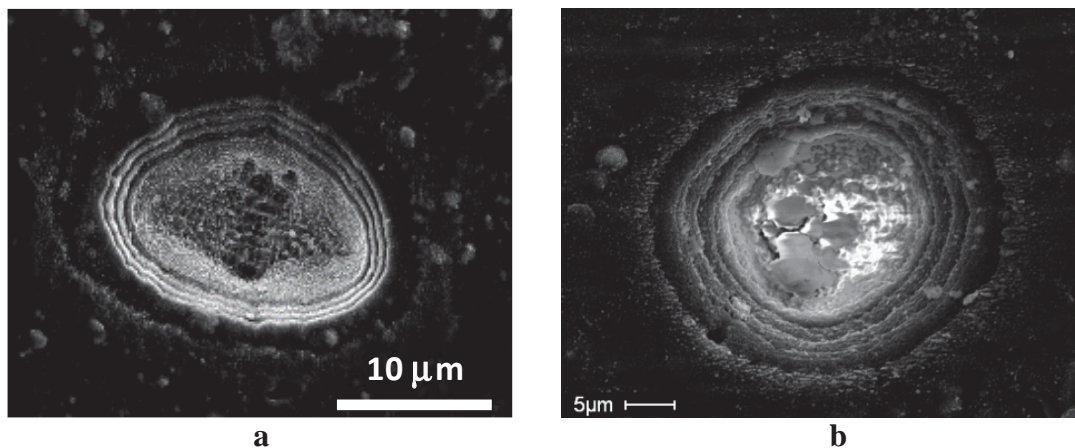
Figure 10. Morphology of ablated (femtosecond laser) zone (a) before oxidation and (b) after oxidation.

Conclusions

The corrosion behavior of multilayer ceramic coated Zirlo tube exposed to supercritical water (SCW) environment at 542 ˚C was studied to evaluate the efficacy of the coating as a potential accident tolerant fuel cladding concept. Zirlo tubes were coated with 4 bi-layers of TiAlN/TiN or with monolithic TiN, on top of Ti bond layers in both cases. In some cases, laser ablation pits were introduced to study the effect of pre-existing defects on oxidation. The PA-CVD process resulted in the formation of Al- or Ti-rich macro-particles originating at the Zirlo surface and causing a distortion of subsequent layers that propagates to the surface, sometimes accompanied

by cracks. These distortions and cracks provided a pathway for rapid access of oxygen to the underlying Zirlo. Their density was such that the oxide layer formed beneath the coatings was of uniform thickness by the time it grew to ~10μm thick. The underlying oxide thickness is consistent with a mechanism of rapid oxygen access Zirlo followed by solid state oxidation at a rate that was similar to uncoated Zirlo. Defects introduced by laser ablation did not spread beyond their original size and did not contribute measurably to the weight gain due to the much higher density of intrinsic defects.

IV.   **Summary of Los Alamos National Laboratory (LANL) Experimental Research Accomplishments**

The C^3 proposal listed the investigation of MAX phase thermal sprayed coatings as one of the coating material/deposition process combinations to be investigated. The attractiveness of the use of coatings of aluminum containing MAX phase material (e.g. Ti_2AlC, Ti_3AlC_2, Nb_2AlC) for accident resistant cladding is in the formation of a protective Al_2O_3 outer layer during high temperature oxidation. Further oxidation is limited as long as the protective Al_2O_3 film is not breached allowing oxygen to reach the Zr alloy structure of the cladding. In order to realize this oxidation protection for cladding, the MAX phase coating must retain the Al contained in the powder feedstock material (no loss of Al during spraying), must not contain open porosity or develop cracks during service allowing oxygen to reach the Zr alloy and must remain adhered to the Zr cladding throughout all normal and off-normal conditions experienced.

A survey of the literature on thermally sprayed MAX phase coatings shows that coating is possible with high velocity oxy-fuel (HVOF) [1], plasma spray [2] and cold spray [3] techniques. The HVOF coatings retain some of the MAX-phase material (Ti_2AlC) but also lose Al compared to the starting powder forming Ti_3AlC_2, TiC, Al-Ti alloys and oxides [4]. Changes in stoichiometry were even greater for plasma sprayed coatings [2]. The HVOF spray conditions that minimized Al loss caused greater porosity, cracks and delaminations in the coating [4]. Therefore, there is a trade off between retaining Al (essential for oxidation protection) and reducing coating flaws (also essential for oxidation protection). Compared to bulk Ti_2AlC which forms a continuous and protective Al_2O_3 surface layer during high temperature oxidation, HVOF coatings of Ti_2AlC do not form a continuous Al_2O_3 layer and are not protective but instead show oxidation extending into the interior of the coating [5]. Therefore, the desirable oxidation protection exhibited in bulk Ti_2AlC was not present in HVOF coatings of Ti_2AlC. In addition, the desirable ductility exhibited by MAX phase bulk materials is not found in Ti_2AlC MAX phase HVOF coatings [1]. Cold spraying is able to deposit Ti_2AlC MAX phase materials without a significant depletion of Al [3] since the particles are not heated to the extent found in other thermal spray techniques. This is a significant advantage over plasma and HVOF coatings. However, cracks and internal delaminations were present in the cold sprayed Ti_2AlC coatings [3] which could decrease oxidation protection.

In a research program separate from C^3, Westinghouse investigated accident tolerant fuel using thermal sprayed coatings. The details of the Westinghouse investigation are shown in Ref. 6. The program investigated Zr cladding alloy coatings of Ti_2AlC and NanoSteel SHS 9172 (Fe, <25 Cr, <15% W, <12% Nb, <6% Mo, <5% B, <4% C, <3% Mn, <2% Si) deposited by cold spray and high velocity oxy-fuel spraying. The HVOF and cold sprayed coatings were tested in steam at 800°F (427°C) and in steam at 1200°C. The HVOF coatings did not survive the 800°F steam test but the cold sprayed coatings did survive and were also tested at 1200°C in steam. The cold sprayed coatings showed no improvement over the Zr alloy in the 1200°C steam tests. Subsequent laser treating experiments on HVOF coatings showed no improvement over the uncoated Zr alloy.

The results from the literature research and the Westinghouse research show that producing a coating of MAX phase material that has the same properties as bulk MAX phase material is very difficult. Cold spray seems to be the most promising technique but there are still significant issues with cracking and adhesion of the coating. Since the existing research into thermal sprayed MAX phase coatings does not look promising, LANL did not pursue the thermal spraying of MAX phase materials for the C³ research program. Instead, LANL investigated coatings containing higher concentrations of Al with metallurgical bonding to the substrate rather than the mechanical bonding of thermal sprayed coatings. The critical issues for a successful coating to increase accident tolerance of cladding were deemed to be: 1) supplying a sufficient amount of Al (or other protective oxide forming material such as Cr or Si) for initial protective oxide formation and self-healing repair of small cracks and porosity; 2) metallurgical bonding (rather than mechanical bonding) of the coating to the substrate; 3) coating strain accommodation to survive the phase transformation and accompanying volume change in the Zr alloy in the 600-700°C range; and 4) maintaining a Zr cladding alloy substrate temperature below 600°C during fabrication to preserve the desirable Zr grain structure and mechanical properties. The LANL coating investigations during the C³ program have sought to produce a coating that satisfies the above 4 issues.

ELECTROSPARK DEPOSITION

Coating fabrication efforts at LANL first focused on development and characterization of oxidation resistant coatings deposited by electrospark deposition (ESD), a pulsed micro-welding process. Initial results have shown that aluminum metal deposited using ESD is successful in generating a protective Al_2O_3 layer at elevated temperatures under oxidizing conditions as illustrated in Figure 1.
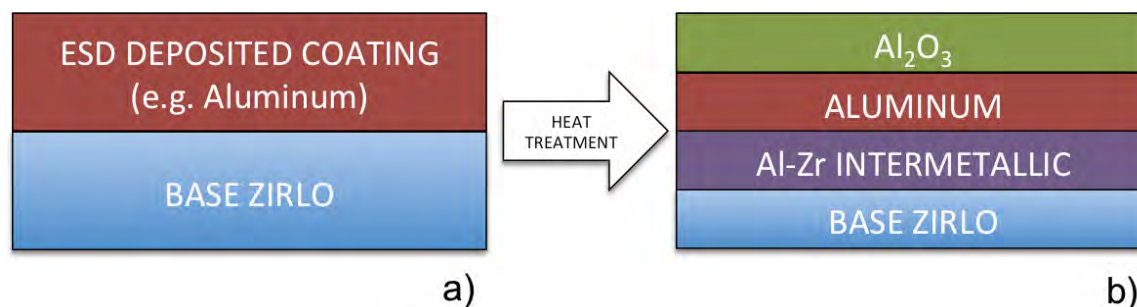

Figure 1. Schematic of ceramic coating synthesis using ESD. The metal oxide precursor is deposited on the Zirlo substrate as shown in a). After a heat treatment step performed under an appropriate partial pressure of oxygen, coarsening of the oxide surface layer and species diffusion will occur as illustrated in b). The relative thicknesses of each layer shown in the graphic are not representative of those anticipated.

Testing of these samples under highly oxidizing environments at 1000°C as documented in the previous reports showed a minimal improvement over the response of uncoated Zirlo. This approach was extended to include base metals intended to seed formation of three ceramic coatings: Al_2O_3, SiO_2, and Cr_2O_3. New coatings were produced using ESD for

characterization and oxidation testing. Examination of these coatings following testing revealed that, while the desired oxide could be located in portions of the surface, the oxide was not continuous and therefore did not prevent breakaway oxidation of the base Zirlo.

ALUMINUM HOT DIPPING

The discontinuous result of samples oxidized following ESD coating prompted exploration of other techniques. In an effort to obtain a uniform coating of Al, other techniques were investigated. One technique investigated was hot dip aluminizing. This technique is commonly used in industry to produce aluminized steel sheet as shown in Figure 2. In addition to covering all surfaces dipped in the Al bath, the process lends itself to high volume production and can likely be cost effectively implemented for the estimated 2 million feet/year of cladding produced by Westinghouse. However, the completeness of coverage (presence of defects) and the effect of defects on oxidation behavior are not known.

Three Zirlo sheet samples 0.020" thick were hot-dip aluminum coated in a laboratory-scale apparatus consisting of a box furnace purged with argon and 1100 aluminum melted in an Al_2O_3 crucible at 750°C. The three samples had aluminum surface area coverage estimated to be 99%, 95% and 90%. Figure 3 shows the sample with 99% coverage. The remainder of the Zirlo surface of the samples was bare due to failure of the Al to wet the surface or due to exposing new Zirlo surface area from trimming the sample.
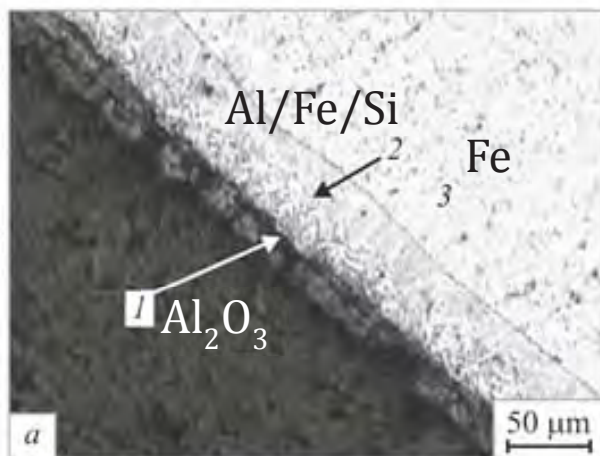

Figure 2. Hot dip aluminized steel with a 50 micron layer of Al/Fe/Si intermetallic on the outer surface covered by a thin layer of Al$_2$O$_3$.

Figure 3. Hot dip aluminized Zirlo sample with dimensions 8 mm x 11 mm.

Samples of ESD Si and Cr coated Zirlo along with hot dip aluminized Zirlo samples were sent to Kerry Abrams of Sheffield University for further examination. The Cr deposits showed only a small amount of mass loss from the Cr electrode during the deposition process. The Cr containing deposits varied in thickness between 30 and 50 μm. The Cr rich outer layer on the Zirlo substrate is shown in Figure 4. Elemental maps of Cr and Zr along with a higher magnification view of the Cr containing surface layer are shown in Figure 5.
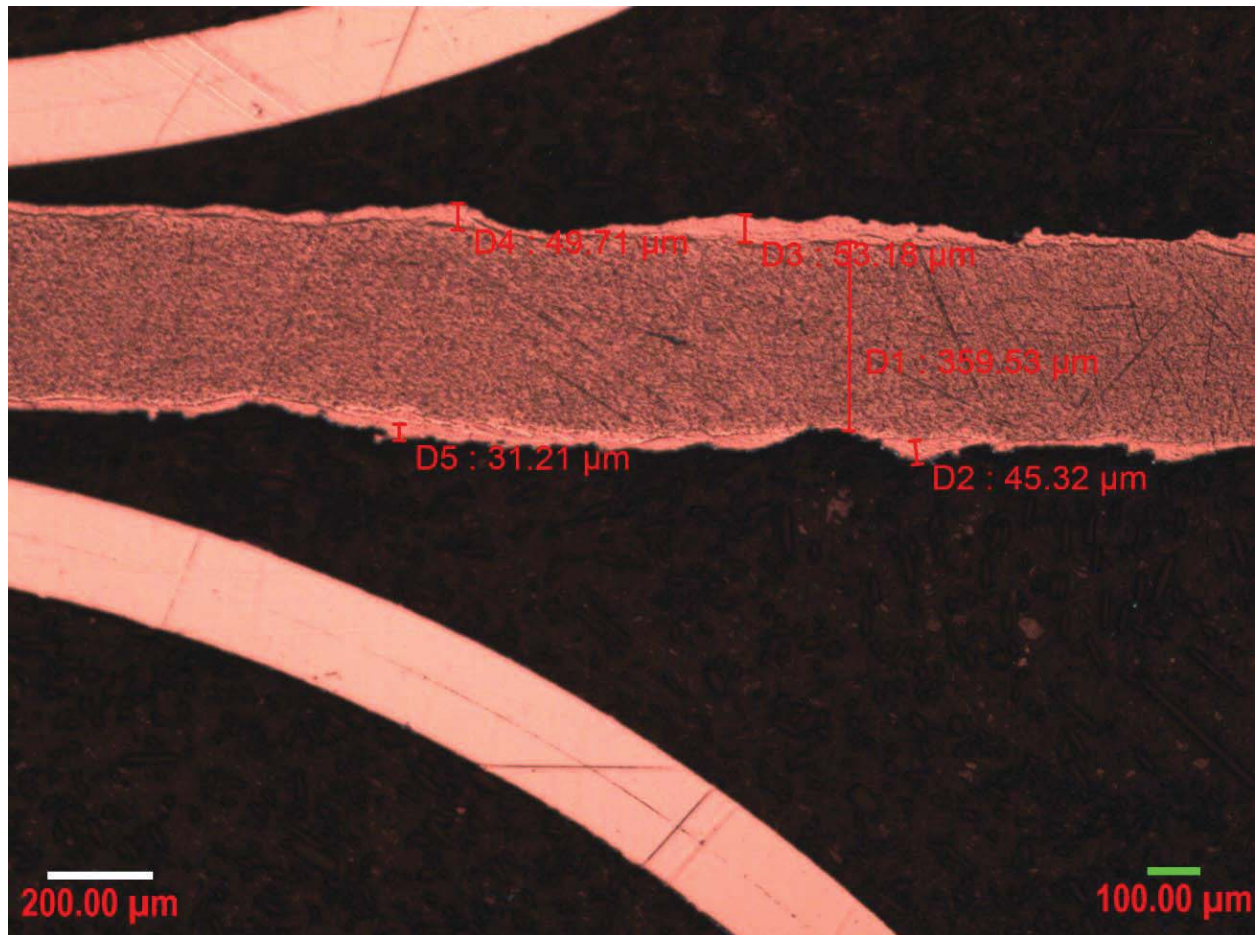
Fig. 4 Cross section of electro-spark deposited Cr on Zirlo substrate showing the variation in Cr containing material depth in regions D1 through D5.
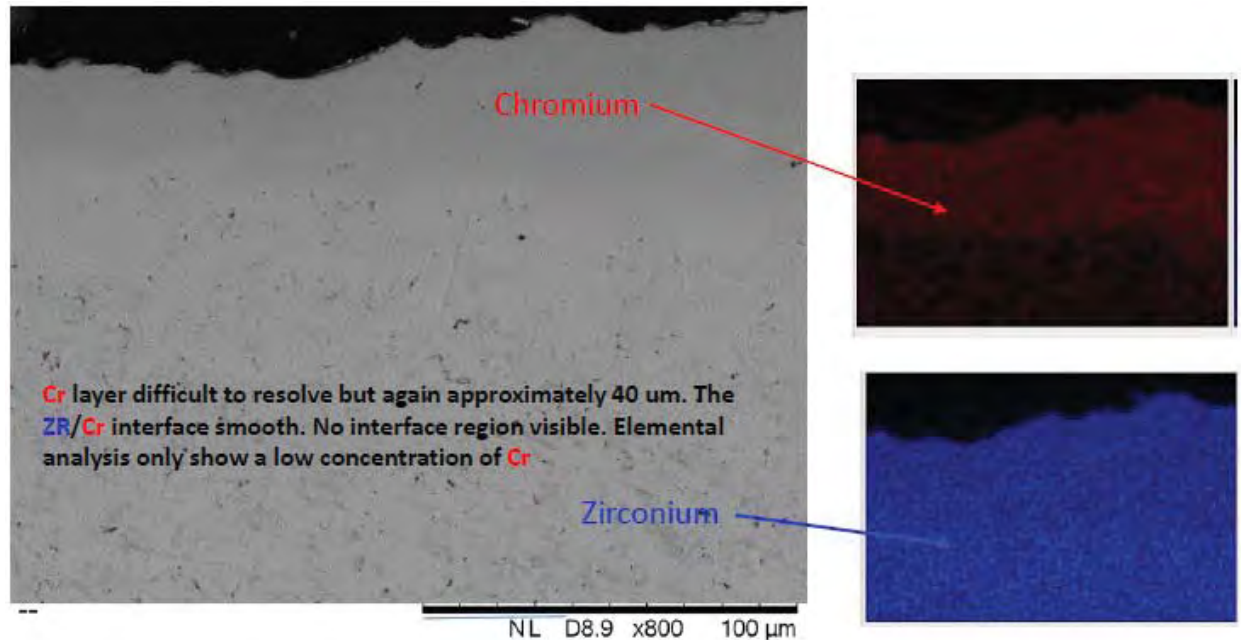
Fig. 5. Cr and Zr elemental maps showing a cross section of the surface region of the Zirlo substrate enriched in Cr deposited by electro-spark deposition.

The Si deposited by electro-spark deposition onto Zirlo is shown in Figure 6. A dendritic reaction layer consisting of Si and Zr is found at the interface between the deposit and substrate. The demonstration of Si deposition with what appears to be a zirconium silicide intermediate layer opens the possibility of forming a protective SiO_2 layer on the outer surface of Zirlo.
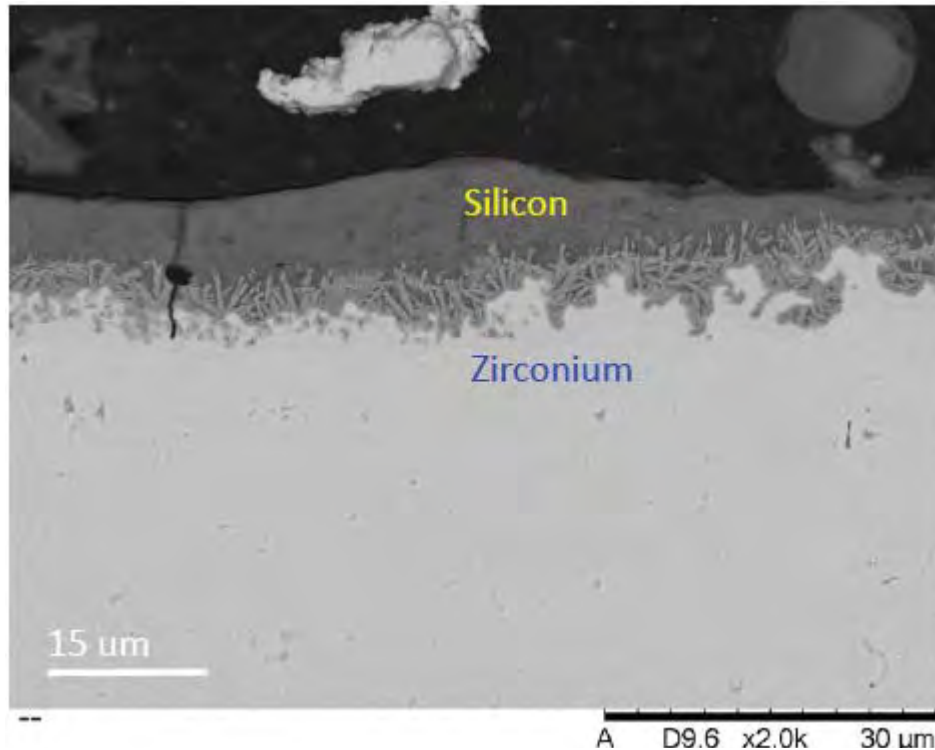
Fig. 6. Cross section of Si deposit on Zirlo.

Samples from the hot dip aluminizing of Zirlo consisted of a reaction layer composed of both Zr and Al with a thickness of approximately 60 μm and on top of that a layer of Al without Zr. The structure is shown in cross section in Figure 7. The outer Al thickness varied significantly around the sample ranging from 0-450 μm. Refinement in the hot-dipping technique for Zr can likely produce consistent results such as is achieved for the Al hot dipping of steel sheet.
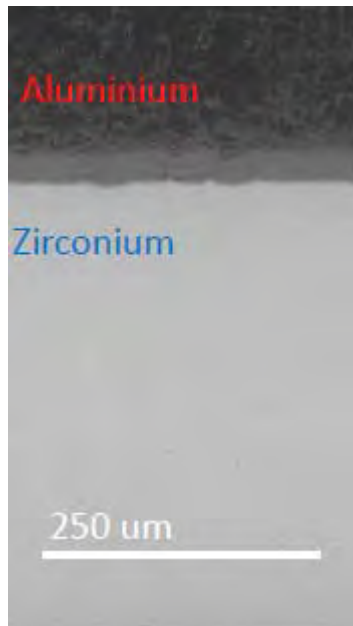
Figure 7. Cross section of hot-dipped Al coating on Zirlo.

In previous testing, coatings containing Al have been demonstrated to improve the high temperature oxidation resistance of Zirlo. However, the Zr-Al compounds on the surface of the Zirlo may perform poorly in the high temperature cooling water environment. In order to provide the needed cooling water corrosion resistance already proven by the Zirlo alloy and to provide high temperature oxidation resistance in the event of a loss of coolant accident, a layered sample geometry was devised. The outer layer is a Zr alloy developed for cooling water corrosion resistance in the normal operational mode. Beneath this outer layer is a second layer consisting of Al to provide the material to form a protective Al_2O_3 layer during a LOCA event. The outer Zr alloy would be consumed by oxidation revealing the Al containing layer beneath. The thickest layer would be the inner most layer composed of a Zr alloy optimized for mechanical and neutronic behavior. With such a layered design for fuel cladding, the behavior during normal operation will be very similar to a single layer Zr alloy material now in use. However, during a LOCA event, the fuel would have enhanced oxidation behavior extending the reaction time allowed before cladding breach occurs.

Initial attempts at fabricating such a three layered structure have partially succeeded. A cross section of one sample is shown in Fig. 8. The outer layer is a Zr foil of thickness 30 μm. The center layer is a varying thickness of Al. The bottom layer is Zirlo.
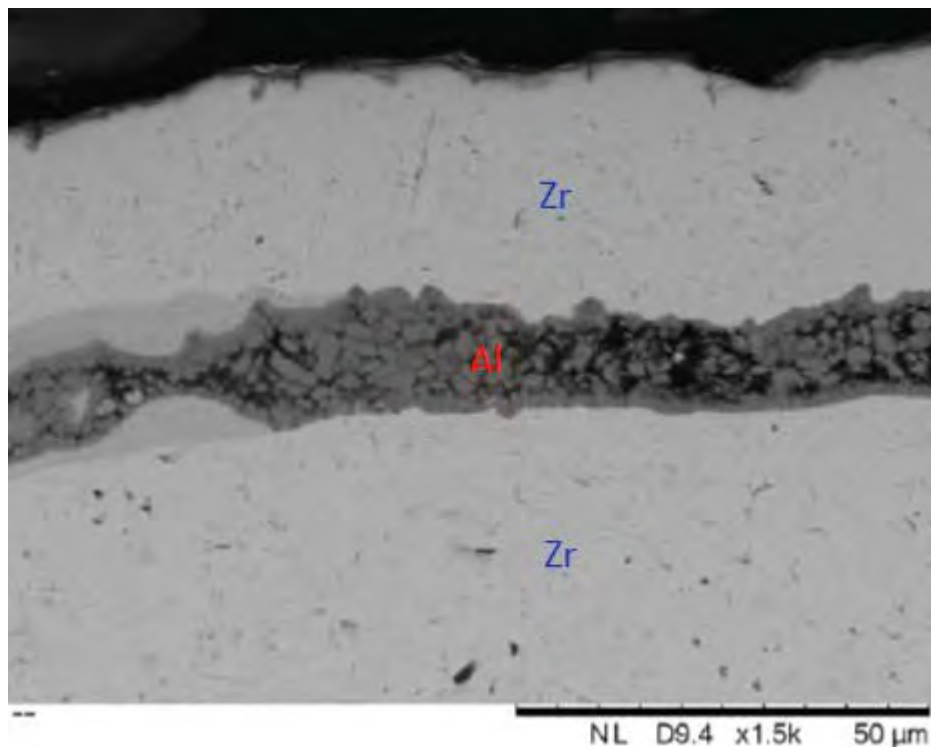
Figure 8. Cross section of Zr-Al-Zr structure.

SPRAY COATING

In collaboration with CeralUSA: Engineered Coatings, bare Zirlo foils were spray coated with a Al-Si alloy powder at four different thicknesses: 50, 80, 110, and 145 microns, then heat treated in vacuum (1E-4 Torr) at 885C for 2 hours.

To test the resistance to oxidation of the AlSi coatings, one sample of each thickness was placed in an atmospheric furnace and held at 700C for various times. The thinnest coating, 50 micron, shows a slight color change (brightening from initial dark gray to a lighter gray) but no delamination until after ~30 minutes of heat exposure, where the coating become brittle, but has not completely spalled off the Zirlo foil. After 1 hour, the 50 micron coating has completely separated from the foil and offers no oxidation protection.

These same experiments were performed on the thicker coatings. The 80 micron sample followed the same pattern as the thinnest coating, completely delaminating from the foil after 1 hour of oxidation exposure. The 110 micron coating did not completely spall off of the foil, but became brittle and substantially delaminated from the sample. The thickest coating sample (145 micron), however, is much more robust, showing no noticeable spalling after 1 hour and the initial dark gray color did not change significantly. When this heat treatment was increased to 24 hours in air at 700C, the thickest coating had become brittle and was not adhered to the foil, but still did not completely spall off the foil, as seen in the thinner samples.

To better understand the causes of delamination, the initial 145 micron foil was cross-sectioned, polished, then analyzed. Elemental mapping by EDS (Figure 9A) shows the presence of Zirconium, Aluminum, and Silicon. Interestingly, the silicon signal is confined to the coating, while the aluminum has diffused into the zirconium substrate. This diffusion layer is more visible using backscattered electron imaging (Figure 9B). This Al diffusion layer is significantly thicker (~20 microns) in the 145 micron coating samples than in the thinner coating samples, suggesting that this interdiffusion layer plays a large role in adherence and oxidation resistance.

Analysis of the oxidized, spalled coating from the thinnest 50 micron sample, which had delaminated during heat treatment at 700C, confirms this segregation of silicon in the AlSi coating. Elemental spectra of the AlSi coating show the presence of Aluminum and Silicon, which is to be expected. However, analysis of the underside of the spalled coating and the foil itself show the presence of aluminum, but no silicon. This suggests that the coating failure occurs somewhere in the Al-Zr interface. It is unclear what role, if any, the silicon is playing in the coating. These elemental spectra and corresponding images can be seen in Figure 10.

Based on the preliminary data, the key portion of the AlSi coating that impacts oxidative resistance seems to be the diffusion layer of Al into the Zirlo foil. Increasing the annealing time after initial coating application would increase this diffusion layer and may improve stability. These early results suggest that the thick AlSi coating layer, and the presence of Si at all, may not be necessary. Removing the outer porous, non-diffused portion of the coating before oxidation testing would better demonstrate the diffused coating resistance to oxidation.

On a more practical note, preparing smaller samples that are coated on all edges with AlSi will lead to more reliable data and testing. Currently, the large coated foils must be sectioned before testing, which exposes pure, uncoated Zirlo foil at the edges. Regardless of the strength of the coating, these uncoated edges will oxidize almost immediately during heat treatment experiments, which does not allow for a truly representative test of the coating.
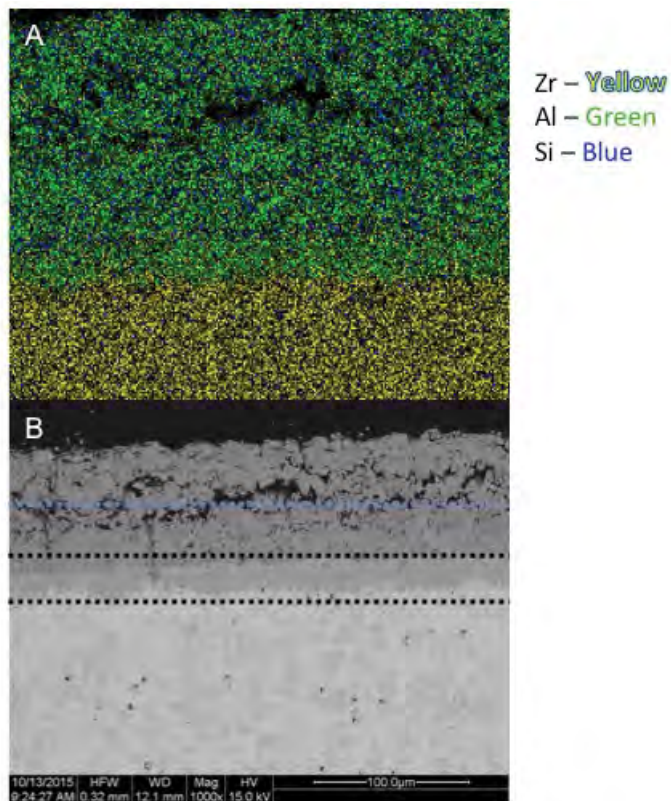
Figure 9: A) EDS elemental map (Zr = Yellow, Al = Green, Si = Blue) of the 145 micron AlSi coating on Zirlo. Notice the silicon signal is predominantly only in the AlSi coating, while the aluminum has diffused into the Zirlo foil. B) Backscattered SEM image of the same region. The interdiffusion layer of aluminum into the Zirlo is shown by two dotted black lines and is ~20 microns thick. A dotted blue line shows a more porous, loosely adhered portion of the AlSi coating ~50 microns deep.
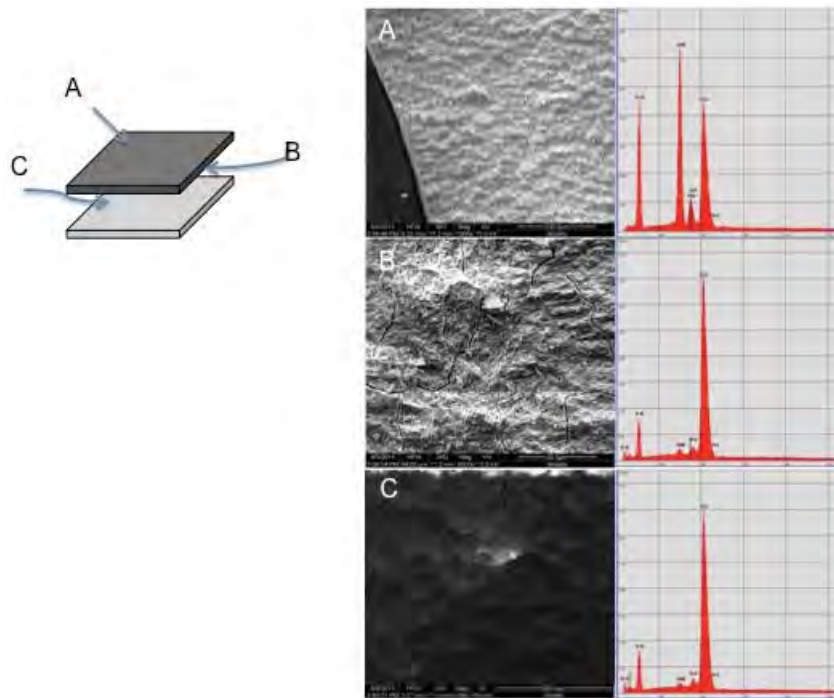
Figure 10: EDS elemental analysis and corresponding SEM images of 50 micron AlSi sample following 1 hour in 700C air furnace. "A" is the top most portion of the coating, which shows the presence of Al, Si, and Zr that has diffused into the coating from the foil. "B" corresponds to the underside of the coating, which shows only Al and Zr, but no Si. Analysis of the foil surface "C", shows Al and Zr, suggesting that the delamination occurs within the Al-Zr interdiffusion layer.

OXIDATION TESTING

The majority of effort expended on this project at LANL supported exploration of the various coating methodologies described above centered on formation of a protective oxide coatings. In addition to the characterization described above, thermogravimetric analysis (TGA) was performed to assess the ability of the as-deposited and/or heat treated coatings to mitigate oxidation. A test condition of 10% oxygen (balance Ar) was chosen to assess breakaway oxidation.

Of the numerous coating techniques evaluated in this work, none were found to measurably improve the oxidation resistance of base Zirlo. TGA testing of coated samples did indicate that delaying oxidation may be possible, but in all cases breakaway oxidation of the base Zirlo was found to result. Examples of this may be seen in Figure 11. Here TGA data for base Zirlo is plotted against hot dipped samples. Although the curves recorded for the different coating variants do exhibit different characteristics, all gain weight rapidly during the testing at 1000C under the prescribed atmosphere (Ar-10%O2). Hypothetical cladding materials possessing this coating structure would not meaningfully improve the coping time of nuclear reactors during a LOCA.
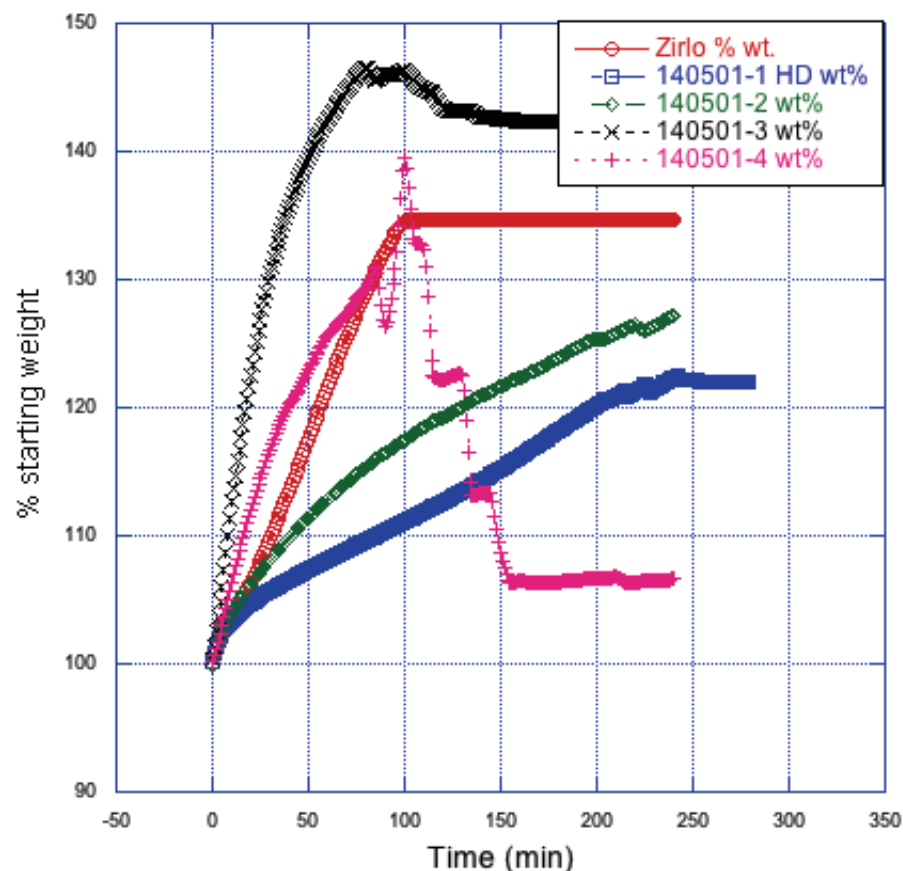
Figure 11. Thermogravimentric oxidation test results for bare and hot dip aluminized Zirlo.

One challenge encountered in TGA testing of applied coatings was geometry. Particularly in development, coatings are applied to samples in a planar geometry. Early testing indicated that oxidation along the edges of the sample, e.g. between the coating and substrate, may result in premature failure of the coating. Unlike in autoclave testing, where exposed Zirlo will perform acceptably and not degrade the results of the coating test, the poor resistance of zirconium alloys to highly oxidizing environments at 1000°C results in rapid delamination of coatings due to oxygen diffusion along the substrate / coating interface. The base Zirlo is thus rapidly consumed making the results of the testing difficult or impossible to interpret. Although such an effect is important to understand in order to assess the impact of coating defects to eventual performance, it is detrimental to baseline evaluation of candidate coating performance.

A technique to mitigate this effect was investigated. The concept is to apply a coating of platinum to all sides of the sample coupon, except for a defined area normal to the coating. This would allow isolation of oxidation effects to the one-dimensional region exposed to the test atmosphere. Platinum was chosen because it is generally inert at the temperatures and atmospheres of interest, but it is important to note that platinum reactions with some of the coating materials included in this study must be considered. A schematic illustration

of this approach is shown in Figure 14. The necessary thickness of platinum was explored in the range of 50 to 200 nm. Numerous schemes of applying and removing a mask were considered. These range from a simple adhesive mask that can be removed after coating to an epoxy 'droplet' that can be dissolved in acetone or other solvent. The critical attributes of a successful mask will be an ability to fully shield the coating in the area intended for testing, complete removal after coating, and masking of a known or measurable area. The latter is important in order to translate weight gain as measured using thermogravimetric analysis or static testing to a weight gain per surface area term as needed for kinetic calculations.

Results of testing at 1000°C in Ar-10% O_2 using Pt coatings of 50 to 200 nm in thickness showed no difference compared to the base Zirlo material. This indicates that the Pt coating is not effective in preventing Zirlo oxidation under these conditions. Since this technique did not show promise in the first few iterations, the alternative approach of using less severe oxidation test conditions will be used for future coating test samples.
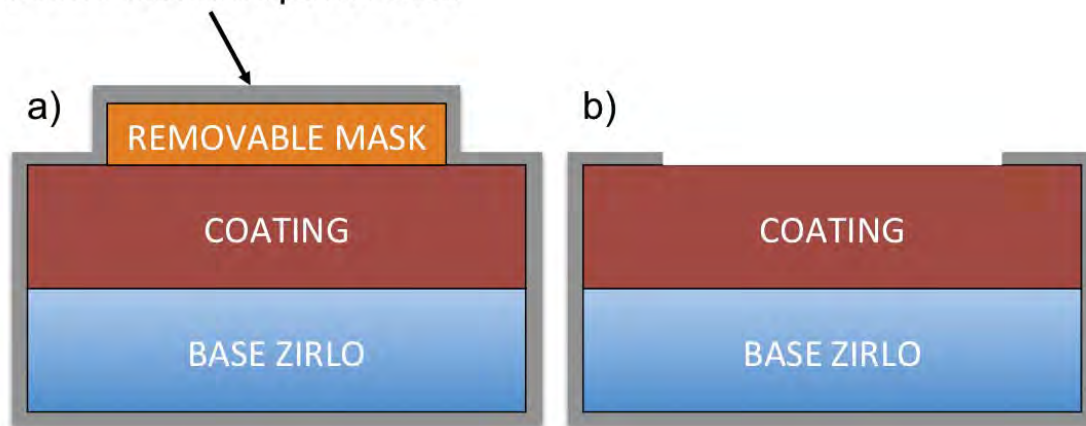

Figure 12. Illustration of the methodology explored for high temperature oxidation testing of coated sample coupons. A platinum coating is applied to all surfaces of the sample as shown in a). After removal of the mask b), a single known surface area is available to be exposed to the test condition.

References

1.J. Jiang, A. Fasth, P. Nylen, W.B. Choi, "Macroindentation and Inverse Analysis to Characterize Elastic-Plastic Properties for Thermal Sprayed Ti_2AlC and NiCoCrAlY", J. Therm. Spray Technol., 18(2), June 2009, p. 194-200.
2. R. Trache, R. Puschmann, C. Leyens, L.M. Berger, B. Matthey, M. Herrmann, "Thermally Sprayed Ti_3SiC_2 and Ti_2AlC MAX-Phase Coatings", Proceedings of the 2013 International Thermal Spray Conference, Busan, Korea, Man 13-15, 2013, p. 74-78.
3. H. Gutzmann, F. Gartner, D. Hoche, C. Blawert, T. Klassen, "Cold Spraying of Ti_2AlC MAX-Phase Coatings, J. Therm. Spray Technol., 22(2-3), March 2013, p. 406-412.
4. J. Frodelius, M. Sonestedt, S. Bjorklund, J. Plamquist, K. Stiller, H. Hogberg, L. Hultman, "Ti_2AlC Coatings Deposited by High Velocity Oxy-Fuel Spraying", Surface & Coatings Technol., 202, 2008, p. 5976-5981.
5. M. Sonestedt, J. Frodelius, M. Sundberg, L. Hultman, K. Stiller, "Oxidation of Ti_2AlC Bulk and Spray Deposited Coatings", Corrosion Science, 52, 2010, p. 3955-3961.
6. P. Xu, "Westinghouse Accident Tolerant Fuel Program", http://www.energy.gov/sites/prod/files/2013/09/f2/5-8-21-2013%20ATF%20Westinghouse%20(xu).pdf.

V.   Summary of University of Colorado (CU) Experimental Research Accomplishments

Ceramic Coatings for Zirlo Prepared by Additive Manufacturing

Abstract

The research in this project has culminated in the development of coatings of 10 mol% cubic zirconia on Zirlo which protects it against corrosion when exposed to streaming steam environment at 400 ^{o}C for several days. The protection mechanism is attributed to (i) a strong adhesion of the coatings to Zirlo, (ii) the absence of electronic conductivity in physically deposited zirconia which prevent the diffusion of oxygen ions through it, and (iii) the crack free nature of the coatings since the cubic phase of zirconia does not suffer from phase transformation. The adhesion was measured by the periodic cracking technique, the electronic conductivity with a I-V experiment, and the corrosion protection by cross-sectional microscopy. The coatings were prepared by an additive, layer-by-layer deposition of the cubic phase in a cold wall reactor using mixed metal-organic precursors of zirconium oxide and yttrium oxide. This method produced crack free coatings of cubic zirconia (but not of 3 mol% yttria stabilized tetragonal zirconia). A patent disclosure for this technology is being filed, which will be followed by a manuscript for publication.

Background

In light water reactors, the zirconium cladding reacts with water to produce zirconium oxide and hydrogen according to the following overall reaction

$$2H_2O + Zr \rightarrow ZrO_2 + 2H_2 \qquad\qquad (1)$$

In practice the corrosion layer continues to grow parabolically with time implying diffusion controlled reaction kinetics [1,2]. Since zirconia is recognized as an oxygen-ion conductor the reaction pathway can be assumed as shown in Fig. 1. However, the diffusion of oxygen ions must be equal to the counter-flow of electrons in order to maintain charge balance. Thus it is very likely that the corrosion overgrowth of zirconia, whose chemistry depends on the composition of the metal on which it grows, becomes doped in such a way as to become electronically conducting. It is also noteworthy that the ceramic overgrowth remains strongly adhered to the metal substrate, presumably achieved by the chemical design of Zirlo.
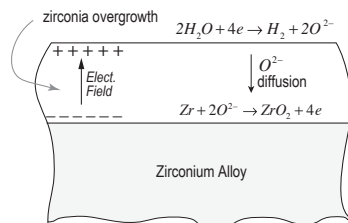

Figure 1: The corrosion of zirconium alloys requires diffusion of oxygen ions from the surface to the interface, which must be balanced by a counter flow of electrons. If the electron transport is slow then a field can develop which will oppose the flow of oxygen ions.

In present work the design of the coatings is based upon the idea that if they were to be constituted from yttria stabilized zirconia, which by the virtue of its use in solid oxide fuel cells, is known to have nearly zero electronic conductivity at moderate temperatures, then they would prevent corrosion. As shown in Fig. 1, an electric field would be generated through the thickness of the zirconia layer which would block the diffusion of oxygen ions. The intrinsic ability of the zirconia ceramic to adhere to Zirlo would assure the mechanical performance of such coatings, as well.

In the following sections results affirm the above concept. Coatings of yttria-stabilized zirconia (YSZ) were deposited from liquid (but volatile) metal organic precursors by an additive, layer-by-layer technique described in earlier papers [3-6]. They were exposed to streaming water paper at 400 °C for several days in an apparatus described in [7]. The electrical conductivities of Zirlo covered with *in-situ* corrosion overgrowth, and Zirlo coated with physically deposited YSZ, as well as that of uncoated metal, were measured by the I-V method. The growth of the corrosion layer in pre-coated specimens was determined by cross-sectional micrography and compared with the values that would have been expected if corrosion had proceeded nominally without any protection being offered by the physically deposited zirconia. The adhesion of the coatings to the metal was measured by the periodic cracking method [8].

Results

Measurement of Interfacial Adhesion

The shear strength of the YSZ-Zirlo interface was measured by the periodic cracking technique where the ductile substrate is deformed plastically to a strain, ε_f, until the ceramic films shows the onset of cracks. With further strain the crack density increases until it reaches saturation with an average spacing of λ^*. If the coating thickness is δ, and E is the Young's modulus of the ceramic then the ultimate shear strength of the metal-ceramic interface is given by

$$\tau^* = \frac{\pi\delta}{\lambda^*}\varepsilon_f E \tag{2}$$

The results from the periodic cracking measurements are shown in Fig. 2. A scanning electron micrograph of the cracks is shown in Fig. 2(a), and the gradual increase in the crack density, λ^{-1}, until it reaches it saturation value, λ^{*-1}, in Fig. 2(b). Substituting the experimental values of $\delta \approx 250$ nm, $\varepsilon_f = 2.5\%$, and $\lambda^* = 2.8\,\mu$m and setting $E = 220$ GPa gives a value for the ultimate shear strength of the interface to be $\tau^* = 1.5$ GPa, confirming the strong adhesion of zirconia to Zirlo.
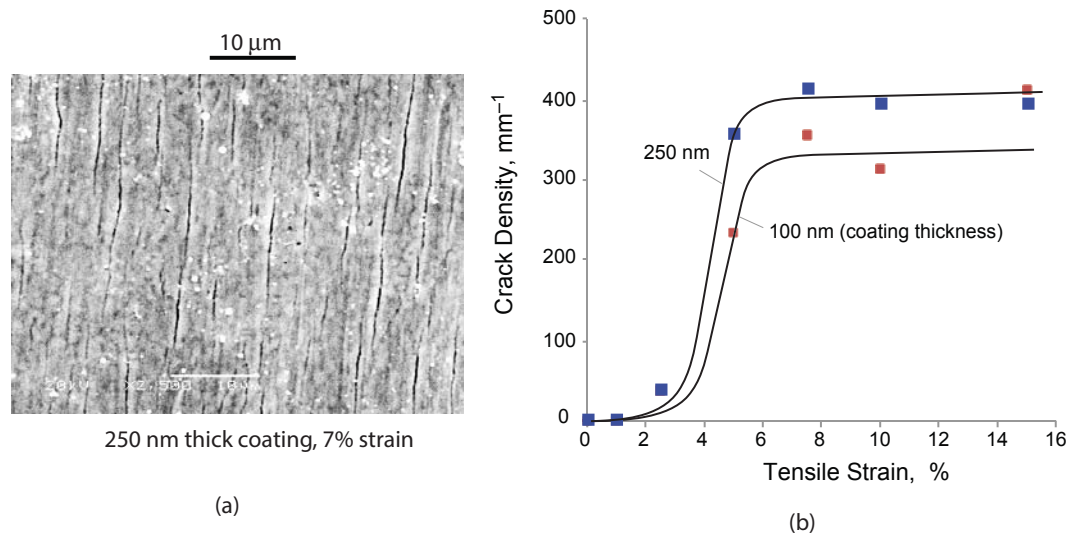
10 μm

250 nm thick coating, 7% strain

(a)

(b)

Figure 2. (a) The cracks in the ceramic film, aligned normal to the tensile axis at a strain of 7.5% in the Zirlo substrate. (b) The cracks begin at a threshold value of the strain and then reach a saturation density, which depends on the thickness of the coating as predicted by Eq. (2).

Measurement of Electronic Conductivity

The electronic conductivity of the coatings was measured with platinum paste being applied to the two sides of the specimens. The Zirlo specimen was 0.45 mm thick and had a surface area of 12.5 mm x12 mm. It was placed within a "coin-cell" which consists of stainless steel electrode, insulated from one another, which are pressed against the two sides of the specimen. The coin cell could then be inserted into the standard holder for an Arbin machine which applies a current to pass through the specimen and measures the voltage generated across it. The resistance is then obtained from the ratio of the voltage divided by the current. The current was cycled between positive and negative current values six times in each direction. The results from these twelve tests for three types of specimens, as received Zirlo, uncoated Zirlo after exposing to steam corrosion at 400 ^{o}C, and 10YSZ (10 mol % yttria) coated Zirlo also corroded under the same condition as the uncoated specimen, are given in Table 1.

	Current range	Voltage range	# Measurements	Resistance Ω
As is Zirlo	–5.79 mA to 5.82 mA	–0.85 mV to +0.13 mV	12	0.15 to 0.27
Zirlo after Corrosion	–1.96 mA to +1.90 mA	–0.25 V to +0.25 V	12	127 to 132
10YSZ coated Zirlo after Corrosion	–0.53 uA to +0.53 uA	–0.25 V to +0.25 V	12	2.12E+06

Table I. Measurements of the through thickness resistance, in Ohms of uncoated, as received Zirlo, corroded Zirlo corroded at 400 °C in steam, and Zirlo coated with 10YSZ and then further corroded under the same conditions as the uncoated Zirlo.

These results show the remarkably high resistance for the 10YSZ coated sample relative to the uncoated sample, after being exposed to steam at 400 °C. The as received Zirlo sample gave a resistance of only ~0.2 Ω. Its resistance increased to ~130 Ω after corrosion reflecting the controlling, albeit low resistance of the zirconia overgrowth. However, the 10YSZ sample was entirely insulating with resistance of several MΩ. These results confirm that the *in-situ* grown zirconia is electronically conducting, while the physically deposited 10YSZ coating is electronically insulating.

Measurement of Corrosion Rates

We have attempted to measure the corrosion rates of YSZ coated Zirlo by cross-sectional microscopy. The weight change measurements encumber significant uncertainty because of corrosion from the edges and uncovered surfaces which can propagate quickly along the interfaces; the sensitivity of the weighing scale that we have was also not adequate for reliable measurements.

The approach for analyzing the data is to assume that the YSZ coating is *non-protective,* that is, it will grow at the same pace as *in-situ* growth of the corrosion layer. We then compare the thickness of the actual overgrowth, with the increase that would be predicted by assuming that the YSZ coating is *not* protective.

We assume that the YSZ coating has a thickness of H, but that it continues to grow as if it had the same behavior as the *in-situ* grown zirconia. Let us say that it is expected to grow to a thickness of $(H + h_c)$ after an exposure of time, t. The following procedure gives an estimate of $h_c(t)$. The parabolic rate of growth of the corrosion layer is described by

$$2h\frac{dh}{dt} = k_p \tag{3}$$

where h is the corrosion layer thickness growing with a parabolic rate constant k_p.
Integrating (3) between appropriate limits

$$\int_{H}^{H+h_c} 2h\,dh = k_p \int_{0}^{t} dt \ \ \text{limits} \tag{4}$$

gives the following result for $h_c(t)$

$$h_c = \sqrt{H^2 + k_p t} - H \tag{5}$$

It now remains to obtain a value for k_p under the conditions of temperature and environment (400 °C in steam) used in all experiments. Its intrinsic *in-situ* value, as given by Eq. (3), was determined with base Zirlo by measuring the change in weight as a function of time, and converting the weight change to the thickness of the zirconia overgrowth. The results from these experiments are shown in Fig. 3.
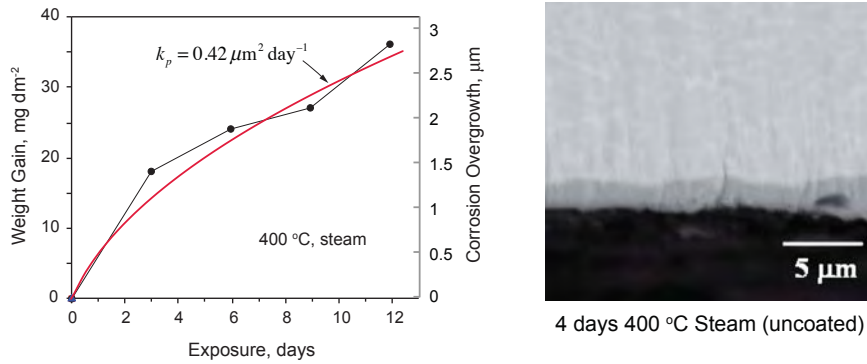
4 days 400 °C Steam (uncoated)

Figure 3. *(Left)* Measurements of the *in-situ* corrosion overgrowth at 400 ^oC in steam for a period of 13 days. The weight change was converted into the thickness of the over growth using the following procedure. The molecular weight of Zr is 91 g mol^{-1} and for ZrO$_2$ it is and 123 g mol^{-1}. From Eq. (2) one mole of Zr will be consumed to produce an overgrowth that equals one mole of ZrO$_2$. Given that the density of ZrO$_2$ is 5.68 g cm^{-3}, the volume of one mole of ZrO$_2$ is 21.65 cm^3, which if spread over and area of 1 dm^2 will be equal to a thickness of 0.2166 cm. Therefore a weight gain of 32 g (the difference between the molecular weight of ZrO$_2$ and Zr) will produce an overgrowth of ZrO$_2$ equal to 0.2166 cm across a surface area of 1 dm^2, which converts to 0.068 mm of overgrowth for a weight gain of 1 mg dm^{-2}. This conversion is used to create the scale on the right hand side in the figure. (Right) A cross sectional micrograph showing the corrosion overgrowth on a pristine Zirlo specimen, in agreement with the estimate from weight change measurements shown in the left.

The protective YSZ coatings deposited by the method described earlier [3-6] had two thicknesses, ~0.95 µm, and ~2.5 µm. The prediction of h_c, given by Eq. (5) assuming the *in-situ* rate of growth described in Fig. 3 for similar corrosion conditions (400 ^oC in steam) is plotted in Fig. 4.
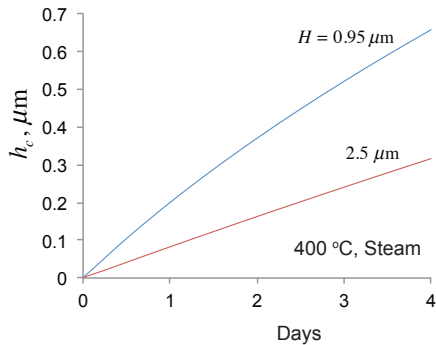

Figure 4. Prediction of increase in the thickness of the coating from corrosion overgrowth, as given by Eq. (5) *assuming* that the coating continues to thicken by corrosion at the same rate as the intrinsic *in-situ* growth of the overlayer as described in Fig. 4. The experiments were carried out with YSZ coatings of two thicknesses, 0.95 µm, and 2.5 µm. In a 4 day exposure they would be expected to add 0.66 µm and 0.32 µm, respectively to the coating thickness if the coating were to be *non-protective.*

Thus from Fig. 4 it is predicted that if the coating was not protective, that is, it continued to grow at the rate of intrinsic corrosion, then a ~0.95 µm thick coating would grow to a total thickness of 1.6 µm after an exposure of 4 days to 400 ^oC in a steam environment. Under the same conditions a ~2.5 µm thick YSZ coating would grow to a total thickness of 3 µm.

The scanning electron micrographs of cross-sections of the YSZ coated specimens before and after corrosion exposure are shown in Fig. 5. If the coatings were *not* protective, then the 0.95 mm thick coating would have been expected to thicken by 50%, and the 2.5 mm thick coating by 20%. This change is not evident which supports the concept that the YSZ coatings were protective.
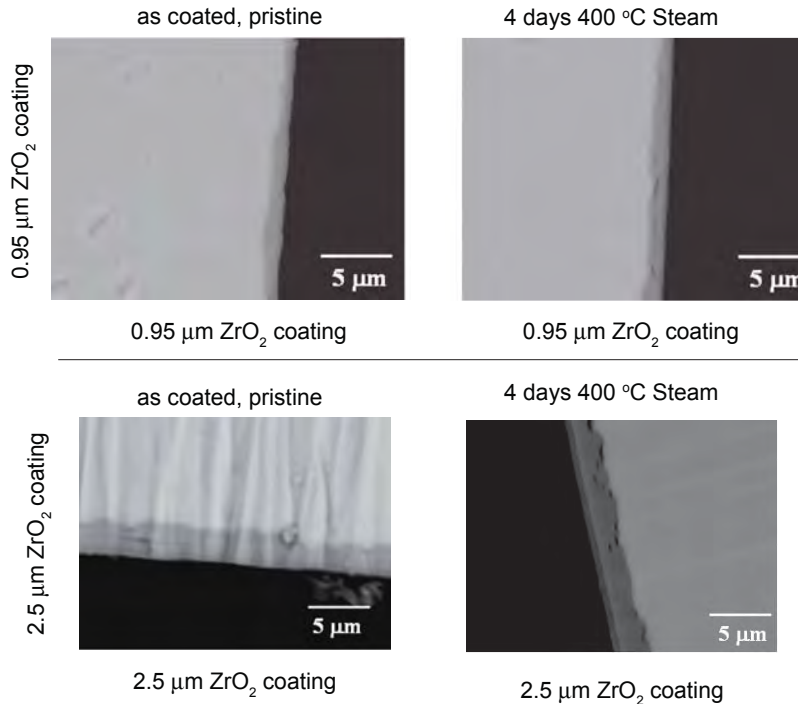
Figure 5. Cross-sectional micrographs showing the as deposited coatings (0.95 μm in the upper and 2.5 μm in the lower micrographs) and the change in the thickness of the coatings after 4 days exposure at 400 °C in steam.

Composition and Characterization of Coatings

In addition to the summary of results presented in the previous sections, we also have results for X-ray diffraction and Raman Spectroscopy of the coatings. Two compositions of coatings, 3 mol% yttria stabilized tetragonal zirconia (3YSZ) and 10 mol% yttria stabilized cubic zirconia (10YSZ) were prepared. The 3YSZ underwent monoclinic to tetragonal transformation which caused cracks in the coatings. However, the 10YSZ coatings being of a single phase remained crack free before and after corrosion testing. Thus for future work 10YSZ compositions would be preferred.

Summary

Physically deposited coatings of yttria stabilized zirconia adhere well to Zirlo with an interfacial shear strength > 1 GPa. Being electronically insulating they inhibit the progression of oxide growth in corrosive environments (400 °C in steam). Coatings of single-phase cubic zirconia stabilized with 10 mol% yttria show better performance than tetragonal zirconia (3 mol% yttria). The tetragonal phase transforms to the monoclinic phase causing cracks in the coating, but the coatings made from the cubic phase remain crack free.

The coatings were produced by an additive manufacturing approach where the metal-organic precursor is nebulized with an ultrasonic nozzle and deposited "pulse-wise" with many layers [3-6]. The process can be up-scaled to coat the outside surfaces of Zirlo tubes in a continuous "roll-to-roll" like coating process.

References

[1] A. T. Motta, A. Couet and R. J.Comstock, "Corrosion of Zirconium Alloys Used for Nuclear Fuel Cladding," *Annual Review of Material Research*, 45 (2015) 311-343.

[2] Allen T.R., Konings R.J.M., and Motta A.T., "Corrosion of Zirconium Alloys", In: Konings R.J.M., (ed.) *Comprehensive Nuclear Materials*, vol. 5 (2012), pp. 49-68.

[3] Krumdieck, S. P., Sbaizero, O., Bullert, A., & Raj, R., YSZ layers by pulsed-MOCVD on solid oxide fuel cell electrodes. *Surface and Coatings Technology*, *167*(2), 226-233 (2003).

[4] Krumdieck, S., & Raj, R., Conversion Efficiency of Alkoxide Precursor to Oxide Films Grown by an Ultrasonic‑Assisted, Pulsed Liquid Injection, Metalorganic Chemical Vapor Deposition (Pulsed‑CVD) Process. *Journal of the American Ceramic Society*, *82*(6), 1605-1607 (1999).

[5] V. A. Versteeg, C. T. Avedisian, R. Raj, "Method and apparatus for CVD using liquid delivery system with an ultrasonic nozzle", US Patent number: 5451260 (1995).

[6] V.A. Versteeg, C.T. Avedisian, R. Raj, "Metalorganic chemical vapor deposition by pulsed liquid injection using an ultrasonic nozzle: titanium dioxide on sapphire from titanium (IV) isopropoxide", *J. Am. Ceram. Soc.* 78 (10) (1995) 2763-68.

[7] B. Sudhir, R. Raj, "Effect of Steam Velocity on the Hydrothermal Oxidation/Volatilization of Silicon Nitride", J. *Am. Ceram. Soc.,* 89 [4] 1380–1387 (2006).

[8] D. C. Agarwal, R. Raj, " Measurement of the ultimate shear strength of metal ceramic interface", *Acta Metall.*, 37 (1989) 1265-1270.

VI.   Summary of Computational Accomplishments

Neutronic and Thermal Effects of Ceramic Fuel Rod Coatings on Reactor Performance

The objective of this IRP is to improve reactor safety of the current nuclear reactor fleet by adding ceramic coatings to the Zr-alloy cladding. These coatings should minimize hydrogen generation and oxidation that may occur at high temperatures under accident conditions, and they may increase the life of the cladding in normal operation by slowing corrosion mechanisms. To date, the following ceramic films have been studied:

1. ZrO_2
2. TiAlN
3. Ti_2AlC
4. Ti_3AlC_2

The computational portion of this effort determines the effects of these coatings on the neutronic and thermal performance of a reference PWR during steady state and transient conditions. In particular, the impacts of 5 and 10 micron thick films have been evaluated for the following reactor operational characteristics:

1) Initial reactivity perturbation,
2) Length of the fuel cycle,
3) Fuel centerline temperature during steady state operation,
4) Impact of coating roughness on fuel centerline temperature,
5) Fuel and moderator temperatures during transients,
6) Zero-dimensional analysis of a loss of cooling accident
     a. Time to boil dry based on total water inventory and total decay heat,
     b. Time to initiate a Zr-H_2O reaction after a loss of cooling accident,
     c. Heat up rate with no cooling,
     d. Time to initiate a Zr-H_2O reaction with no Coating and no cooling,
     e. Time to initiate a Zr-H_2O reaction with coating and no cooling, and
     f. Production of hydrogen.
7) Single channel analysis of a loss of cooling accident.
     a. Calculation of single channel boil down time,
     b. Calculation of the steam temperature above the liquid-steam interface,
     c. Heat transfer coefficient in the steam region, and
     d. Fuel centerline and clad axial temperature distributions.

Initial Reactivity Perturbation
Changes in reactivity from a reference case are obtained by using the ABH method (proposed by Amouyal, Benoist, and Horowitz), the MCNP Monte Carlo code, XSDRN discrete ordinates code, and the four factor formula. Results from the MCNP and ABH calculations are in good agreement and are listed in Table 1. Neither the results from discrete ordinates nor the thermal utilization methods are in particularly good agreement with the MCNP results and are not listed.

Table 1: Reactivity changes for 5 and 10 micron thick films for the MCNP and ABH computational methods.

Simulation	Thickness (micron)	MCNP		ABH Method
		k-value	% change	% change
Reference	-	1.49032	-	-
ZrO_2	5	1.48961	0.05%	0.03%
TiAlN	5	1.48768	0.18%	0.14%
Ti_2AlC	5	1.48879	0.10%	0.15%
Ti_3AlC_2	5	1.48948	0.06%	0.11%
ZrO_2	10	1.48936	0.06%	0.05%
TiAlN	10	1.48741	0.20%	0.27%
Ti_2AlC	10	1.48654	0.25%	0.30%
Ti_3AlC_2	10	1.48716	0.21%	0.22%

The initial MCNP cell calculations used reflective boundary conditions, and they were in poor agreement with the ABH method results. It was then realized that reflective boundary conditions for MCNP cell calculations permit internal reflection of neutrons when they should escape and re-enter the cell. The MCNP calculations were rerun with white boundary conditions, and good agreement between MCNP and ABH results was obtained.

Length of Fuel Cycle
An initial decrease of reactivity due to adding a coating should reduce the fuel cycle length of a light water reactor (LWR) if no other changes are made to the fuel management scheme since the decrease in reactivity due to fuel depletion in LWRs is relatively linear, as shown in Figure 1. Therefore a linear reactivity model[2] should provide a relatively accurate estimate for the loss of the length of the fuel cycle. Figure 1 illustrates calculations based on a code that was in commercial use for a number of years by Westinghouse. Results for the various coatings are listed in in Table 2.
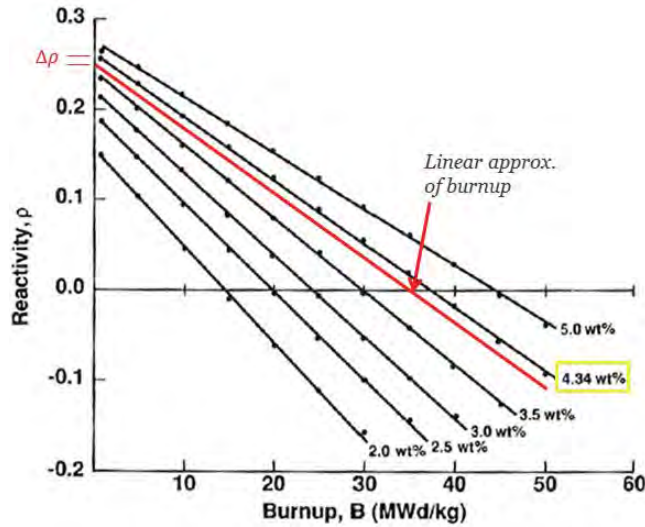
Figure 1: Reactivity vs. Burnup relationship obtained from the Electric Power Institute implementing a version of LEOPARD program.[2]

The red-line in Figure 1 is added to illustrate the change in reactivity and the impact on the burnup for a reference reactor. In this study, the linear reactivity model is used to assess the loss in fuel cycle length for a 900 day cycle (i.e. three periods of 300 days within the reactor) and the final burnup value based on a reference burnup of 50 MWd/kg. The loss in fuel cycle length (days) is based on the reactivity change from a reference reactor (no-film region) fuel pin.

Table 2: Estimated loss fuel cycle length based on a 900 day cycle and fuel burnup.

Film	Thickness (micron)	Reactivity Change (MCNP)	Cycle Loss Estimate (days)	Burnup (MWd/kg)
ZrO_2	5	0.05%	0.45	48.6
TiAlN	5	0.18%	1.62	48.5
Ti_2AlC	5	0.10%	0.90	48.6
Ti_3AlC_2	5	0.06%	0.54	48.6
ZrO_2	10	0.06%	0.54	48.5
TiAlN	10	0.20%	1.80	48.5
Ti_2AlC	10	0.25%	2.25	48.4
Ti_3AlC_2	10	0.21%	1.89	48.5

Given that the loss in fuel cycle length due to the inclusion of the coatings evaluated is less than three days, the economic penalty is not considered to be significant relative to the potential benefit of adding a coating.

Fuel Centerline Temperature During Steady State Operation

Adding coatings (also designated as films) could increase or decrease the fuel centerline temperature since there are competing factors that determine this value. The small increase in conduction path should increase the centerline temperature; however, coatings could have a higher or a lower heat transfer coefficient. Consequently, calculations that accurately model the heat transfer and fluid flow are required to determine the impact of these competing factors on the fuel centerline temperature.

An estimate of the fuel centerline temperature is obtained based on values for a reference reactor[1] listed in Tables 3 and on estimates for thermal conductivities listed in Table 4.[1,3,4,5]

Table 3: Parameters for the calculation of temperature changes in a fuel pin.[1]

Parameter	Variable	Value
Linear Power Density (**MAX**)	q'_{max}	460 W/cm
UO$_2$ Fuel Thermal Conductivity	k_{Fuel}	0.0250 W/cm K
Clad (Zircaloy IV) Conductivity	k_{Clad}	0.1070 W/cm K
Heat transfer coefficient in gap	h_g	0.75 W/cm^2 K
Heat transfer coefficient in moderator	h	3.2 W/cm^2 K
Moderator Temperature	T_{mod} or T_∞	290°C

Table 4: Thermal conductivity of proposed coatings. Zircaloy IV has a thermal conductivity of ~107 W/m-K.

Coating	Thermal Conductivity (W/m-K) [1,3,4,5]
ZrO$_2$	2.0
TiAlN	5.0
Ti$_2$AlC	30.0
Ti$_3$AlC$_2$	40.0

The following equation is used to calculate the fuel centerline temperature,[6]

$$T_{C.L.} - T_\infty = \frac{q'}{2\pi}\left(\frac{1}{2k_{Fuel}} + \frac{1}{R_g h_g} + \frac{1}{k_{Clad}}\ln\left(\frac{R_{co}}{R_{ci}}\right) + \frac{1}{R_{oo}\left(k_{film}/\delta_o\right)} + \frac{1}{R_{oo}h} \right)$$

(1)

where, $T_{C.L.}$ is the fuel centerline temperature, T_∞ is the moderator temperature, k is the thermal conductivity for the respective region, R_g is the radius to the gap, R_{co} and R_{ci}

represent the inner and outer cladding radius. R_{oo} is the radius to the outside of the film, δ_0 is the film thickness, and h is the heat transfer coefficient from the film to the coolant.[6]

No measurements data were found for the heat transfer coefficient (h) of the coatings, so a typical value of $3.0 \frac{W}{cm^2 K}$ for LWRs with Zr cladding was used for the reference case.[1] Uncertainty analyses were performed for the fuel centerline temperature since several parameters in the equation for fuel centerline temperature were not well defined. These analyses utilized Monte Carlo techniques for sampling triangular distributions of the heat transfer coefficient triangular distribution with endpoints of $\left(2.7 - 3.3 \frac{W}{cm^2 K}\right)$, Table 5 lists maximum temperatures for each simulation.

Table 5: Temperature changes from moderator to fuel centerline and inner cladding radius with $h_s = 3.0 \frac{W}{cm^2 K}$. A typical PWR has a moderator temperature of 290 °C (554°F) and a fuel centerline of 2,109 °C.

	Film Thickness (μm)	Centerline Temperature (°C)	Change in T_{CL} (%)
Reference	-	1834.8 ± 8.903	-
ZrO$_2$	5	1840.89 ± 8.913	**0.33%**
TiAlN	5	1837.22 ± 8.925	**0.13%**
Ti$_2$AlC	5	1835.18 ± 8.928	**0.02%**
Ti$_3$AlC$_2$	5	1835.07 ± 8.930	**0.02%**
ZrO$_2$	10	1847.01 ± 8.925	**0.67%**
TiAlN	10	1839.66 ± 8.924	**0.27%**
Ti$_2$AlC	10	1835.58 ± 8.936	**0.04%**
Ti$_3$AlC$_2$	10	1835.38 ± 8.939	**0.03%**

One can obtain an analytical solution for the fuel centerline temperature if one assumes a linear power density or a sin distribution. For the case of a sin distribution the linear power density can be written as,

$$q'(z) = q'_0 \sin\left(\frac{\pi z}{H}\right). \tag{2}$$

A differential energy balance along the channel is given by the following equation,

$$w c_p dT = q''(2\pi r_F)dz = q'(z)dz \tag{3}$$

where w is the mass flow, c_p is the specific heat of the coolant, and z is the position along the channel. Integration of this equation gives,

$$w c_p \int_{T_{inlet}}^{T_M} dT = q_0' \int_0^z dz' \sin\left(\frac{\pi z'}{H}\right) \tag{4}$$

with the result,

$$T_M(z) - T_{inlet} = \frac{q_0' H}{\pi c_p w}\left[1 - \cos\left(\frac{\pi z}{H}\right)\right]. \tag{5}$$

For the case of a linear distribution with a sin distribution, the fuel centerline temperature is as follows:

$$
\begin{aligned}
T_{CL} = T_{inlet} &+ \frac{q_0' H}{\pi c_p w}\left[1 - \cos\left(\frac{\pi z}{H}\right)\right] \\
&+ \frac{q_0' \sin\left(\frac{\pi z}{H}\right)}{2\pi}\left(\frac{1}{2k_{Fuel}} + \frac{1}{r_g h_g} + \frac{t_C}{r_C k_C} + \frac{t_{film}}{r_{film}\, k_{film}} + \frac{1}{r_{film} h_s}\right).
\end{aligned} \tag{6}
$$

Each of the proposed films will have a unique thermal conductivity, thus each film will affect the system uniquely, along with any film thickness variation (i.e. r_{film}, t_{film}, k_{film}).

Impact of Coating Roughness on Fuel Centerline Temperature

The coating roughness impacts on the heat transfer coefficient and on the pressure drop along the coolant channel can be estimated by using the Moody diagram[8]. Given the film roughness and the Reynolds number one can read the Darcy friction factor from the graph. Given the Prandtl and Nusselt (which includes the friction factor) numbers, one can calculate the heat transfer coefficient.

Based on information from Pennsylvania State University[9], their films are deposited with roughness values of approximately 10 μin (0.254 μcm). This value is used with two perturbations of 5 μin and 15 μin roughness to illustrate the change on the heat transfer coefficient. Table 6 lists the heat transfer coefficient using the three film roughness values.

Table 6: Impact on heat transfer coefficient with various film friction factors.

Film Roughness (μin)	Darcy Friction Factor (f)	Nusselt Number	Heat Transfer Coefficient (W/cm^2 K)
5 (0.127μm)	0.014	528.26	2.97
10 (0.254μm)	0.015	566.66	3.18
15 (0.381μm)	0.016	605.13	3.40

Based on the values listed in Table 6, a variation of no more than 10 % should be expected in the heat transfer coefficient for any of the coatings that may be developed. According to Duderstadt[1], typical heat transfer coefficient values for Zr-Clad to Water ranges from $2.8 - 4.5 \frac{W}{cm^2\ K}$ depending on flow parameters.[1]

The coating roughness also introduces a pressure drop along the channel. This pressure change uses the Darcy friction factor along with moderator flow parameters, as seen in the following equation:[1,6]

$$\Delta P = \rho g \left[f \frac{L}{d_h} \frac{v}{2g} \right] \tag{7}$$

where, ρ is the moderator density, g is gravity, L is the channel length, v is flow velocity, d_h is the hydraulic diameter, and f is the Darcy friction factor.

Table 7: Pressure drop along the flow channel.

Film Roughness (μin)	Friction Factor (f)	Pressure Drop (psi)
5 (0.127μm)	0.014	1.67
10 (0.254μm)	0.015	1.79
15 (0.381μm)	0.016	1.91

Fuel Moderator Temperature During Transients
The axial dependence of the fuel centerline temperature is evaluated by decreasing the linear power density and the coolant flowrate, at different rates, to one-half of the initial values for each of the four coatings. In particular, the following transients are considered:

1) The linear power density is uniformly decreased at an exponential rate faster or slower than the moderator flow rate is changed as follows:

$$q'(t) = \frac{1}{2}q'(0)[\exp(-\lambda_1 t) + 1] \tag{8}$$

2) The moderator flow rate is decreased at an exponential rate faster or slower than the linear power density is changed as follows:

$$\dot{m}(t) = \frac{1}{2}\dot{m}(0)[\exp(-\lambda_2 t) + 1]. \tag{9}$$

If these two time-dependent equations are substituted into the thermal resistance equation, the following equation is obtained:

$$
\begin{aligned}
T_{CL} = \\
T_{inlet} + \frac{\left(\frac{1}{2}q'(0)[\exp(-\lambda_1 t)+1]\right)H}{\pi c_p \left(\frac{1}{2}\dot{m}(0)[\exp(-\lambda_2 t)+1]\right)}\left[1 - \cos\left(\frac{\pi z}{H}\right)\right] + \\
\frac{\left(\frac{1}{2}q'(0)[\exp(-\lambda_1 t)+1]\right)\sin\left(\frac{\pi z}{H}\right)}{2\pi}\left(\frac{1}{2k_{Fuel}} + \frac{1}{R_g h_g} + \frac{1}{k_{Clad}}\ln\left(\frac{R_{co}}{R_{ci}}\right) + \frac{1}{R_{oo}\left(k_{film}/\delta_o\right)} + \right. \\
\left. \frac{1}{R_{oo}h}\right).
\end{aligned}
\tag{10}
$$

If the linear power density is decreased faster than the mass flow rate, (i.e. $\lambda_1 > \lambda_2$), the coolant temperature momentarily decreases and then returns to its initial value. This case is illustrated in Figure 2 for a fuel rod with no coating. The same transient is shown for the TiAlN coating in Figure 3.
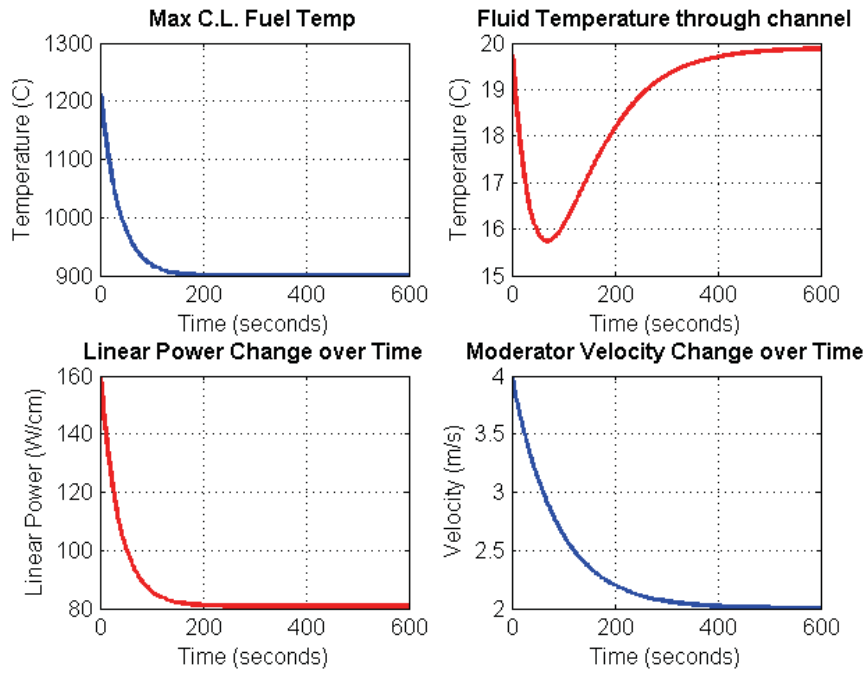
Figure 2: No-film region simulation illustrating the two varying parameters and the impact on the moderator temperature change along the channel.
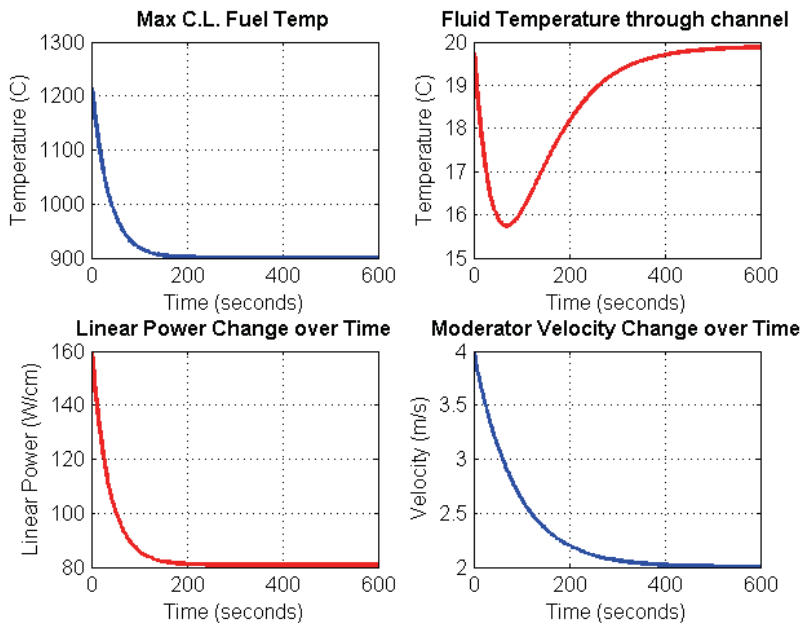
Figure 3: Power transient followed by slower velocity change using 10μm TiAlN film.

As a second simulation, the lambdas are switched so that the flow velocity decreases faster than the power density. Additionally, the heat transfer coefficient is decreased from $3.4\frac{\text{W}}{\text{cm}^2\text{K}}$ to $3.0\frac{\text{W}}{\text{cm}^2\text{K}}$. Figures 4 and 5 illustrate these simulations for the reference case with no-film model and for the TiAlN coating.
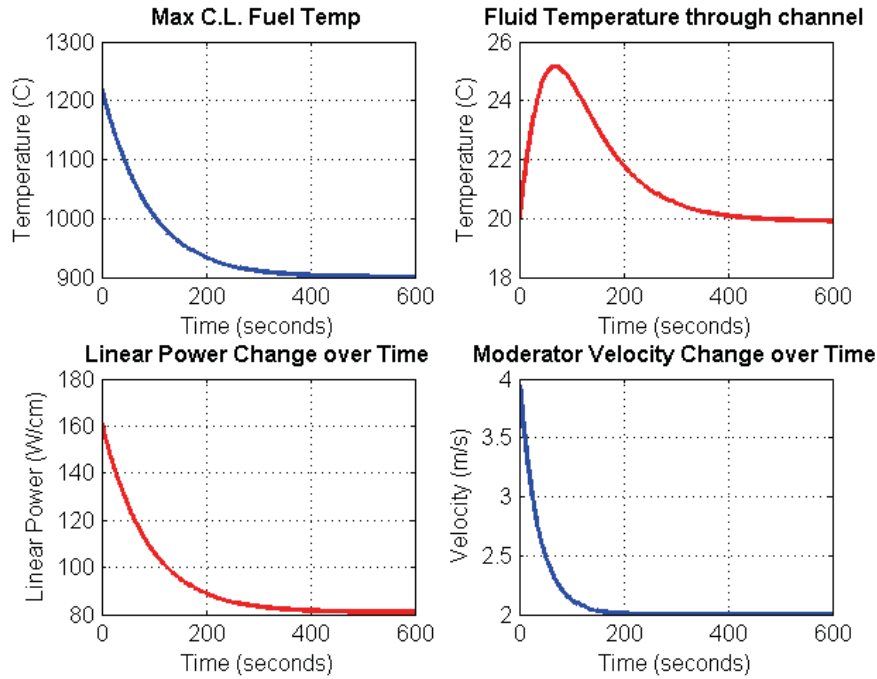
Figure 4: Reference run for flow velocity variation followed by power density.
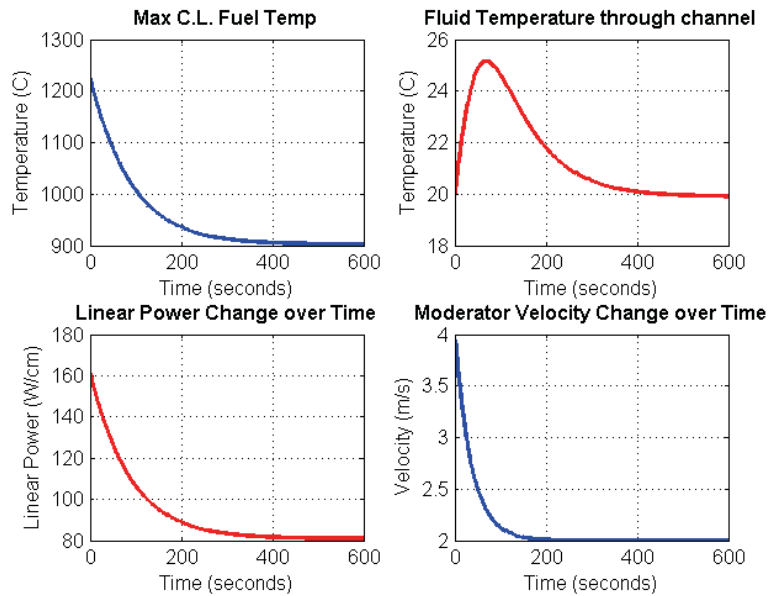
Figure 5: Flow velocity transient followed by slower power density change using 10μm TiAlN film and lower heat transfer coefficient.

Detailed analyses on the impact of coatings on reactor performance and safety are provided in a thesis by Stewart.[10] It is shown that coatings evaluated to date have an insignificant impact on reactivity, heat transfer, and fuel cycle length.

Zero-Dimensional Analysis of a Loss of Cooling Accident

The progression of reactor core degradation during a loss of coolant accident depends on many variables. For example, fuel loading history, power history, and the time duration of the loss of coolant flow impact the progression of the accident. In order to obtain an estimate of the benefit of a coating, the following assumptions are made:

1) The core is protected until the mass of the water in the active core is converted to steam,
2) The decay heat is based on one year of operation and one day of cool down,
3) The heat up rate is based on the heat capacity of UO_2 and the heat capacities of the cladding and structural materials are neglected,
4) A zirconium-water reaction would begin after the initial mass of water in the core is converted to steam,
5) Continuing boiling of water in the lower plenum would provide H_2O to support a Zr-H2O reaction, and
6) The coating protects the cladding until it reaches the melting temperature of zirconium.

The impact of a loss of flow accident with and without a coating on fuel pin is evaluated based on a zero-dimensional model and on a single-channel analysis. Table 8 provides a list of parameters that are used to obtain results presented in this report.

Table 8. Reactor-specific parameters from Duderstadt[1]. Material properties are obtained from a variety of sources.

Parameter	Value		Parameter	Value
Reactor Power (MWth)	3,411		Fuel Pin Pitch (cm)	1.25
Mass of UO_2 (kg)	90,000		Fuel Pellet Diameter (cm)	0.819
Specific Power, Full Power (W/g)	37		Thickness of Gap (cm)	0.0082
Heat Capacity of UO_2 (J/kg K)	240		Thickness of Clad (cm)	0.0572
Heat Capacity of H_2O (J/kg K)	385		Number of Fuel Pins	50,952
Melting Temperature of Zr (C)	1,830		Number of Assemblies	193
Melting Temperature of SS (C)	1,370		Assembly Pin Locations (17x17)	55,777
Melting Temperature of UO_2 (C)	2,865		Height of Fuel (cm)	366
Zr-H_2O Exothermic Reaction (C)	1,200		Volume of H_2O in Core (m^3)	12.8
Density of UO_2 (g/cm^3)	10.9		Active Core Volume (m^3)	32.8
Density of Zr (g/cm^3)	5.68		Mass of Zr Cladding (kg)	14,000
Heat of H_2O Vaporization (J/mole)	40.65		Thickness of coating (μm)	10
Decay Heat After One Day (MW)	15.3		Clad to Steam Ht Trans Cof (W/m^2C)	7,500
Specific Heat After One Day (W/g)	0.185		Clad to Water Ht Trans Cof (W/m^2C)	45,000

Time to Boil Dry Based on Total Water Inventory and Total Decay Heat
The volume of water that is available to provide a heat sink for decay heat is assumed to be the moderator volume in the active core. The rate of boiling water, and time to boil dry are estimated by,

$$BR = P_d / \Delta H \qquad (11)$$

$$T_B = M_w / BR \qquad (12)$$

where,

BR=boiling rate of water (kg/s)
P_d=decay power (kW)
ΔH=heat of vaporization of water

The decay power is estimated by,

$$P_d/P_0=0.0065(t^{-.2}-(t+T_0)^{-0.2}) \tag{13}$$

where,
t=days after shutdown
T_0=days of operation
P_0=full power

The mass of water in the active core is calculated to be about 12,000 kg, and the heat of vaporization for water is 40.65 Joules/mole. The decay heat after one year of operation and one day of cool-down, the power level is determined to be 0.45 %, or 15.3 MW. Thus, the time to boil the water in the active core volume is about 40 minutes. Based on the assumptions cited above, a heat up with effectively no cooling capacity would be delayed by about 40 minutes due to water being boiled from the core.

Heat Up Rate with no Cooling
The rate of temperature increase of the fuel pin is estimated by,

$$HR=SP_{dh}/C_f \tag{14}$$

where,

HR=heat up rate,
SP_{dh}=specific power due to decay heat, and
C_f=heat capacity of fuel.

Based on a heat capacity of 240 J/(kg K) of UO_2 and a specific heat during decay heat (one year of operation and one day of delay) of 0.185 W/g, the heat up rate (neglecting the heat capacity of Zr) is 0.8 K/s.

Time to Initiate a Zr-H$_2$O Reaction with no Coating and no Cooling
The initial average cladding temperature is estimated be about 350 C, and it is assumed that the Zr-H_2O reaction would begin after the temperature increased to about 1,200 C. Given a heat up rate of 0.8 K/s, the Zr-H_2O reaction would begin about 20 minutes after the moderator is boiled from the active core volume. In other words, it would begin about one hour after all coolant circulation is lost.

Time to Initiate a Zr-H$_2$O Reaction with Coating and no Cooling
It is assumed that a "perfect" coating could prevent a Zr-H_2O reaction until the steam temperature reaches the melting temperature of Zr (about 1,830 C). Thus, the coating would prevent the Zr-H_2O reaction for an additional 20 minutes under this highly degraded core condition.

Production of Hydrogen
The energy generated by the Zr-H_2O reaction is given by

Zr + 2H_2O → ZrO_2+2H_2O + 586.9 kJ/mole Zr
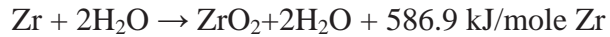
Reaction of 14,000 kg Zr cladding would yield about 600 kg of H_2 and about 8.8 E+10 J of energy.

It is expected that this reaction would occur in a high temperature steam environment and that it would most likely be limited by the availability of H_2O. If the reaction takes place in one hour the specific power during the reaction would be about 0.3 W/g during the reaction, which is nearly double the energy release rate due to decay heat.

Single Channel Analysis of a Loss of Cooling Accident
Figures 6 and 7 illustrate the model considered for single channel analysis.
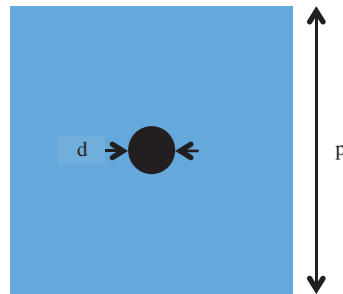
Figure 6. Radial view of a single channel.
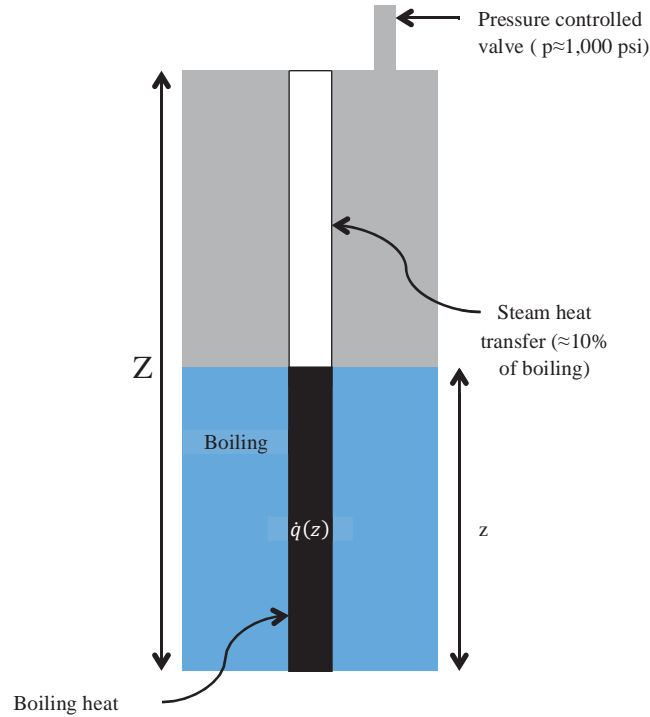
Figure 7. Axial view of single channel.

Parameters used in the following equations are defined as follows:
Z=height of the fuel channel,
z(t)=level of the steam-water interface,
P=Pressure set by the controlled venting,
p=fuel pin pitch,
T_{bw}=Temperature of the boiling water,
m_s(z)=generation rate (and flow rate) of steam produced as a function of the steam-water level interface,
q'(z)=linear power density as a function of the steam-water level interface,
D=effective diameter of a unit cell,
d=diameter of the fuel pin,
ΔH(P,T)=heat of vaporization at pressure P and temperature T,
T_{ax}(z)=axial temperature distribution of the fuel pin,
T_s(z,t)=the steam temperature as a function of position and time,
M_w(z,t)=mass of water in the channel at height z and time t,
ρ_w=density of water,
ρ_s=density of steam,
A_m=area of moderator,
V_m=volume of moderator,
v_s=velocity of steam,
M_L(z,t)=mass of water transferred to steam at height z and time t,
E_t(t)=energy transferred from the pin to water and steam,
M_{wr}(z,t)=mass of water remaining after time t at location z,

$\Delta z(t)$=change in water level at time t,
$w_L(t)$=water level at time t,
r_f=radius of the fuel,
k_f=thermal conductivity of fuel,
h_g=heat transfer coefficient of the gap,
k_c=thermal conductivity of the clad,
t_x=thickness of the coating,
k_x=thermal conductivity of the coating,
h_s=surface heat transfer coefficient,
t_{dry}=time to boil dry.

The rate of steam production is modeled to be the energy generation rate in the liquid region divided by the heat of vaporization of water, as follows:

$$m_s(z(t)) = \frac{\int_0^{z(t)} q(z')dz'}{\Delta H(P,T)} \tag{15}$$

The mass of water in the region of height z is given by,

$$M_w(z(t)) = \frac{z\pi}{4}[D^2 - d^2]\rho_w \tag{16}$$

and the velocity of steam in the steam region is modeled as follows:

$$v_s(z,t) = \frac{m_s(z)}{\rho_s A_w} \tag{17}$$

$$v_s(z,t) = \frac{\int_0^{t(z)} q'(z')dz'}{\Delta H(P,T)\rho_s A_w} \tag{18}$$

The time dependence of the decay heat is very slow relative to the time duration of loss of flow accident. Thus,

$$E_t(z) = t \int_0^z q'(z)dz' \tag{19}$$

The mass of water converted to steam in time t is given by,

$$M_L(z,t) = E_t(z)/\Delta H(P,T) \tag{20}$$

or

$$M_L(z,t) = t \int_0^z q(z')dz' / \Delta H(P,T) \tag{21}$$

The mass of water remaining is,

$$M_R(z,t) = M_w(Z,0) - M_L(z,t) \tag{22}$$

and the remaining water volume is,

$$V_{RW} = zA_w \tag{23}$$

The mass lost is,

$$M_L(z,t) = \rho_w A_w(Z - z) \tag{24}$$

The height of the liquid-steam interface is given by,

$$z = Z - M_L(z,t)/\rho_w A_w \tag{25}$$

$$z = Z - t \int_0^z q(z')dz' / \rho_w A_w \Delta H(P,T) \tag{26}$$

An incremental change in height may be determined by,

$$\Delta z(\Delta t) = \frac{\Delta t}{\rho_w A_w \Delta H(P,T)} \int_0^Z q'(z')dz' \tag{27}$$

$$z(\Delta t) = Z - \Delta z(\Delta t) \tag{28}$$

The axial temperature distribution can also be determined by selecting various height of the liquid-steam interface and calculating the corresponding axial temperature distribution.

Calculation of Single Channel Boil Down Time
Equation 26 can be rewritten to directly calculate the time that corresponds to a specific liquid-steam interface as shown below.

$$t(\mathfrak{z}) = \int_Z^{\mathfrak{z}} (dt/d\mathfrak{z}') \, d\mathfrak{z}' \tag{29}$$

$$t(\mathfrak{z}) =$$
$$\int_Z^{\mathfrak{z}} d\mathfrak{z}' \left[\frac{\rho_w A_w \Delta H(P,T)}{\int_0^{\mathfrak{z}'} q'(\mathfrak{z}'')d\mathfrak{z}''} \right] \tag{30}$$

For the case when the linear power density is a sin function, then one can show that

$$t(3) = \left(\frac{\rho_w A_w \Delta H(P,T)}{qavg'}\right)\left(\frac{z}{\pi}\right) ctn(\pi 3/2z) \tag{31}$$

Where q_{avg}' is defined as the average linear power density. If the linear power density is constant then

$$t(3) = \left(\frac{\rho_w A_w \Delta H(P,T)}{qavg'}\right) \ln(z/3) \tag{32}$$

Note that z is defined as the axial location of the liquid-steam interface.

Calculation of the Steam Temperature Above the Liquid-Steam Interface
A Matlab code that utilized XSteam[11] was written (described in the appendix) to implement the single channel analysis. In particular, XSteam, was used to obtain various steam properties when one or two other conditions are known. For example, pressure and enthalpy can be used as input functions to determine density, temperature, specific volume, specific entropy, specific heat capacity, etc. An explicit computational process is used to determine steam temperature at small axial intervals above the liquid-steam interface. The rate of energy addition at each small axial interval is used to determine the energy added, which is assumed to be the enthalpy added. XSteam is then used to determine the temperature increase, and density decrease, based on the energy added in each small interval. The mass flow rate is assumed to be constant so Equation (18) may be used to calculate the steam velocity.

An alternative method (although not used in the current implementation of the code) is to use a differential energy balance for fluid temperature and linear heat rate may be expressed as:

$$dE(z) = \dot{m}(t)c_p dT = q'(z,t)dz \tag{33}$$

$$\dot{m}(t) = \rho(t)\, v(t)\, A\, c_p \tag{34}$$

$$\rho(t)v(t)Ac_p dT = q'(z,t)dz \tag{35}$$

This equation can be integrated to obtain the steam temperature along the channel as follows:

$$T_s(z,t) = T_z(t) + \frac{1}{\rho_s(t)v_s(t)Ac_p}\int_0^z q'(z,t)\, dz \tag{36}$$

Heat Transfer Coefficient in the Steam Region
A constant heat transfer coefficient of 3000 W/m²K was used in previous work for the steam region. Treating the heat transfer more carefully, the Hsu and Westwater model for the film boiling region was used for the steam to clad heat transfer coefficient. For vertical laminar flow in the film boiling region, the average value of the heat transfer coefficient over the channel length L is found as

$$h_{CL} = 0.943 \left[\frac{g \ (\rho_l - \rho_v) \ \rho_{vfm} \ k^3_{vfm} \ h'_{fg}}{L \ \mu_v \ \Delta T} \right]^{\frac{1}{4}} \tag{37}$$

where the subscript vfm represents the film vapor [3]. The heat transfer coefficient requires calculating h'_{fg} as in Eq. (38)

$$h'_{fg} = h_{fg} + 0.34 \ c_{pv} \ \Delta T \tag{38}$$

The temperature difference ΔT from the solid surface to the bulk liquid is found as

$$\Delta T = T^M_{B} - T_s = 0.127 \left[\frac{g \ (\rho_l - \rho_v)}{2 k_F} \right]^{\frac{2}{3}} \left[\frac{\sigma}{g(\rho_f - \rho_g)} \right]^{\frac{1}{2}} \left[\frac{\mu_{fm}}{g \ (\rho_f - \rho_{g)}} \right]^{\frac{1}{3}} \tag{39}$$

This temperature difference is used to find the clad surface temperature from the centerline temperature.

Fuel Centerline and Clad Axial Temperature Distributions
For the case when steam flow rate is equal to the boiling rate, the following equation may be used to calculate the fuel centerline temperature.

$$T_{CL}(z,t) = T_s(z,t) + \frac{q'(z,t)}{2\pi r_F} \left[\frac{r_F}{2k_F} + \frac{1}{h_G} + \frac{t_C}{k_C} + \frac{t_f}{k_f} + \frac{r_F}{(r_F + t_C + t_f)h_s(z,t)} \right] \tag{40}$$

In order to calculate the axial fuel centerline temperature distribution steam properties must be determined as the steam flows up the channel. This is accomplished through the use of Xsteam[11], which is a Matlab data base used to evaluate steam and water properties based on other known properties (based on implementing International Association for the Properties of Water and Steam (IAPWS) IF97 standard formulation). XSteam uses the following functions and units for calculations.

Table 2. XSteam functions, taken from [11].

Notation	Quantity	
T	Temperature	C
p	Pressure	bar
h	Enthalpy	kJ/kg
v	Specific volume	m³/kg
rho	Density	kJ/m³
S	Specific Entropy	kJ/kg C
u	Specific Internal Energy	kJ/kg
Cp	Specific Isobaric Heat	kJ/kg C

	Capacity	
Cv	Specific Isochoric Heat Capacity	kJ/kg C
w	Speed of sound	m/s
my	Viscosity	Pa s
tc	Thermal Conductivity	W/(m C)
st	Surface Tension	N/m
x	Vapor fraction (0-1)	-
vx	Vapor Volume Fraction (0-1)	-

Single channel analysis results for shown in Figures 8-17 are based on the following assumptions:

1) Pressure is controlled at 1000 psi to maintain a constant water temperature in the liquid region,
2) Pressure maintains water temperature at a fixed location on the enthalpy curve,
3) Nucleate boiling can be maintained so that the heat transfer rate does not cause dry out or film boiling.

These assumptions, in conjunction with the single channel model obtain the boil down time as shown in Figure (8).
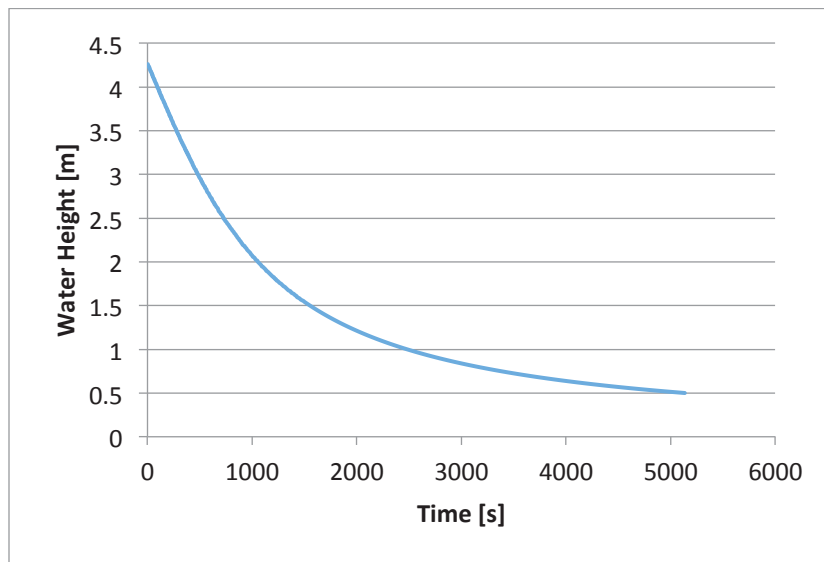
Figure 8. Time to boil down for a single channel.

The fuel temperature in the boiling region is assumed to remain at the saturation temperature for a pressure of 1,000 psi, and the heat transfer coefficient is assumed to be 32,000 W/m^{2}C in the region with water remaining. The plot in Figure 8 was cut off at 0.5m water height, due to long computational time since the remaining water boiling off exponentially slowly. Recall that the zero dimensional result (based on total water inventory and total decay power) for time to boil

dry was about 40 minutes. Note that the single channel result shows that it takes about 80 minutes for the core to boil down to 0.5 m.

For the steam region a clad to steam the Hsu and Westwater's correlation is used to obtain the heat transfer coefficient. Given the heat transfer coefficents and parameter values listed in Table 1, results for steam temperature, steam velocity, steam enthalpy, steam density, and fuel centerline temperature are obtained and illustrated in Figures 9 through 15. The axial distribution of steam temperature, found by inputting steam enthalpy and pressure into XSteam, is shown in Figure 9.
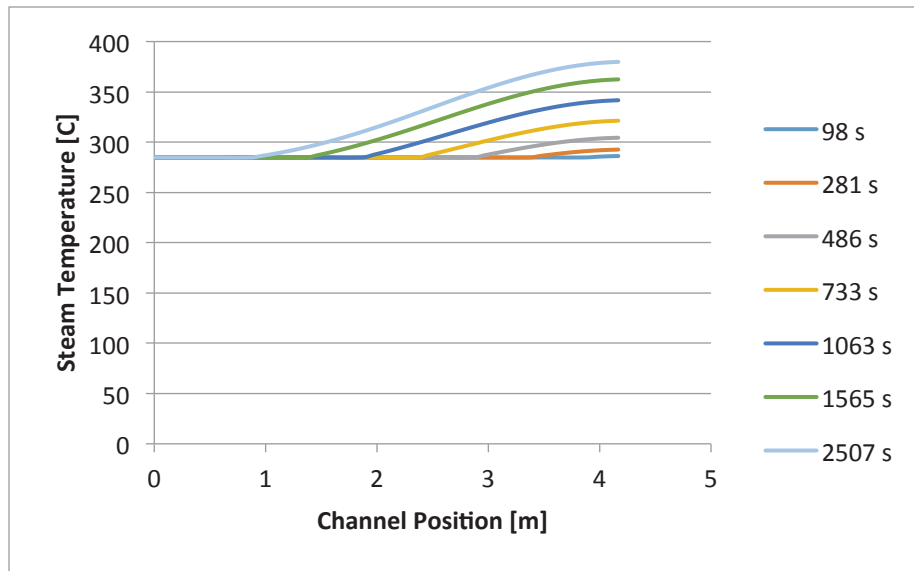
Figure 9. Steam temperature axial temperature distribution as a function of time to boil dry

The axial distribution of velocity of the steam can be found by Eq. (17) and is shown in Figure 10.
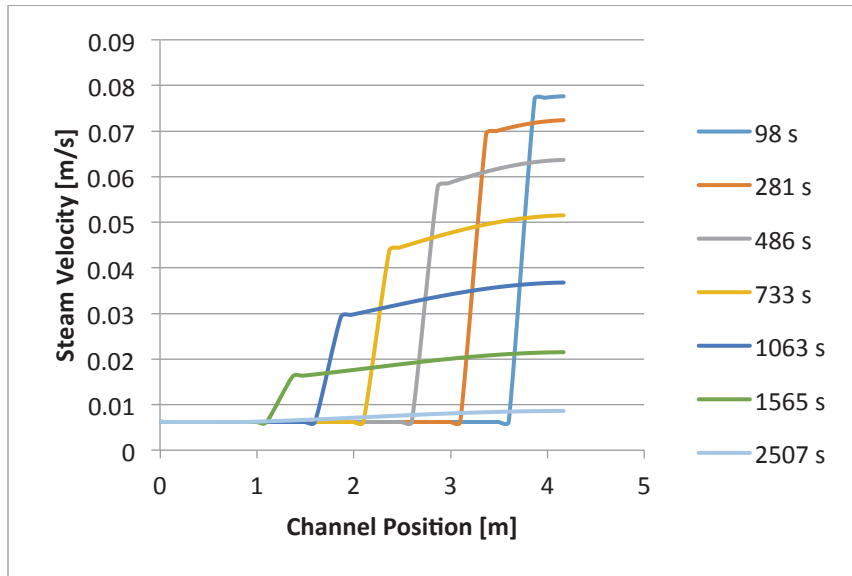
Figure 10. Steam velocity axial distribution as a function of position.

The axial distribution of enthalpy is shown in Figure 11. Enthalpy is used as an input parameter for XSteam in calculating the axial distributions of steam temperature and density.
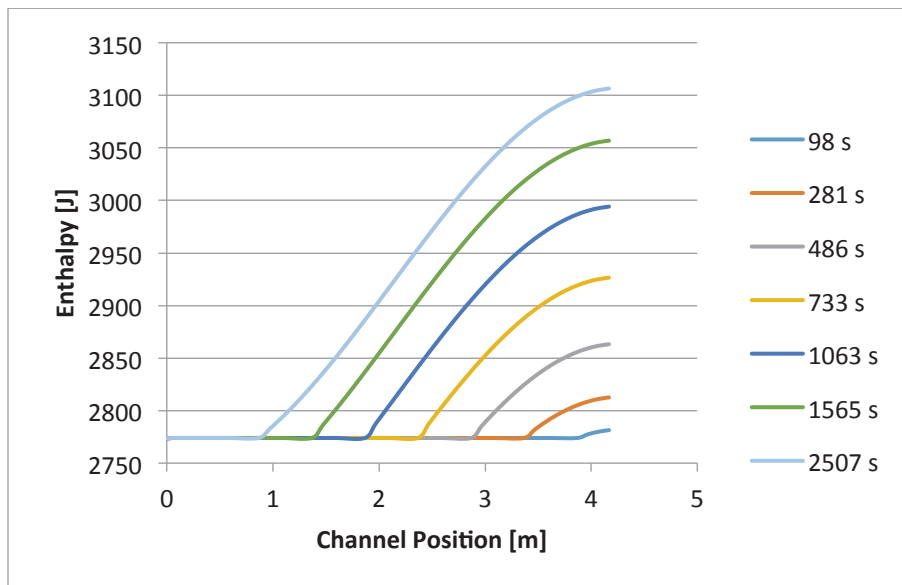
Figure 11. Axial distribution of enthalpy as a function of position.

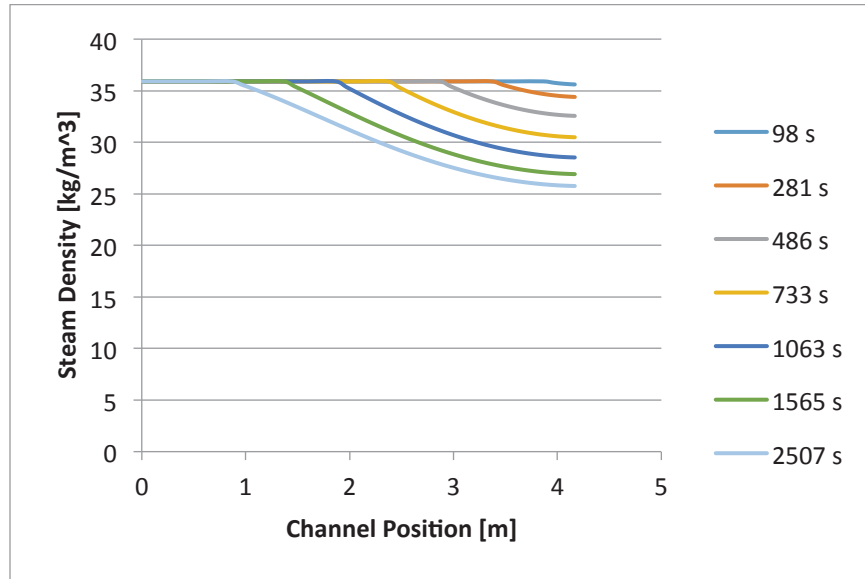The axial distribution of steam density is shown is Figure 12.

Figure 12. Axial distribution of steam density as a function of position

The heat transfer coefficient in the water region is assumed to be 32,000 W/m^{2}C. The steam to clad heat transfer coefficient is calculated using Eq. (35-36). Within the steam region, the maximum heat transfer coefficient decreases to approximately 100 W/m^{2}C. The heat transfer coefficient in Figure 13 is used to calculate the axial distributions of the fuel centerline temperature and clad surface temperature, and the heat transfer coefficient in the steam region is shown in Figure 14.
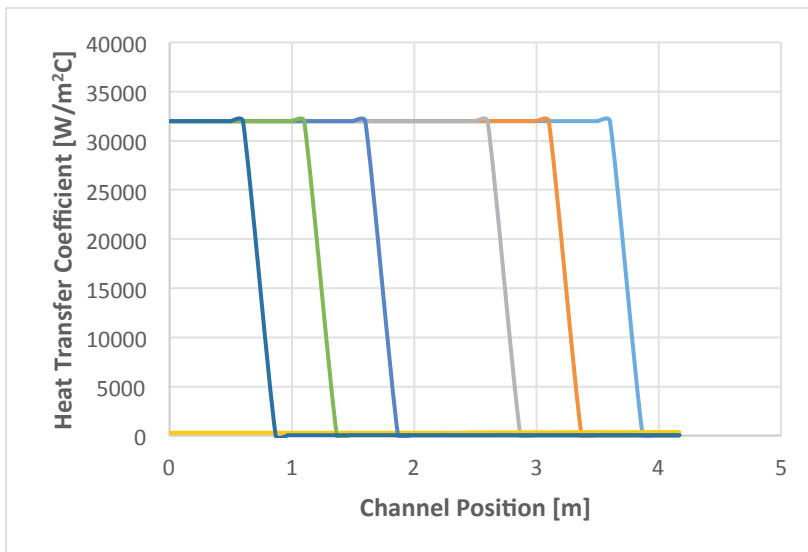
Figure 13. Heat transfer coefficient, assuming 32,000 W/m^{2}C in the water region and following the Hsu and Westwater correlation in the steam region for film boiling.

The axial distribution of fuel centerline temperature with the Hsu and Westwater heat transfer coefficient is shown in Figure 15.
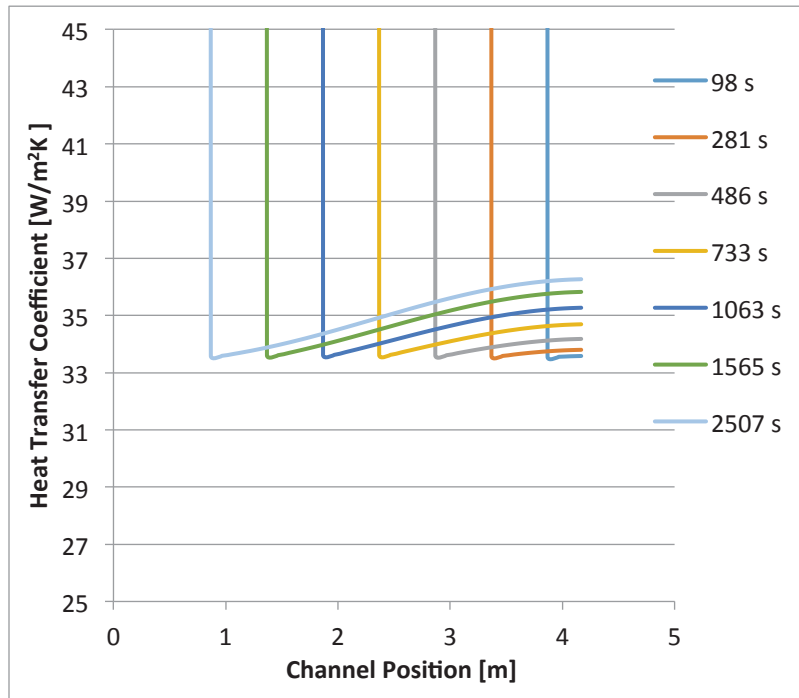

Figure 14. Heat transfer coefficient in the steam region during film boiling.

The heat transfer coefficient in the steam region is initialized at the estimated heat transfer coefficient in water, and it increases as the steam flows up the channel. The axial distribution of the clad surface temperature, found using the temperature difference between bulk liquid and solid surface with Eq. (37) is shown in Figure 15, and the fuel center line temperature is shown in Figure 16. The difference in the clad surface temperature and the fuel centerline temperature is shown in Figure 17.
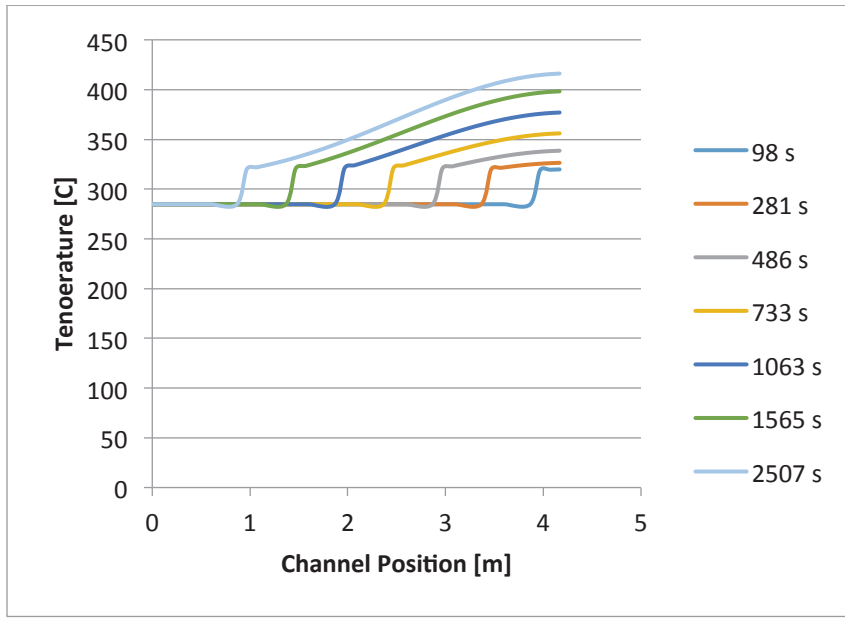
Figure 15. Fuel clad temperature axial distribution as a function of position.
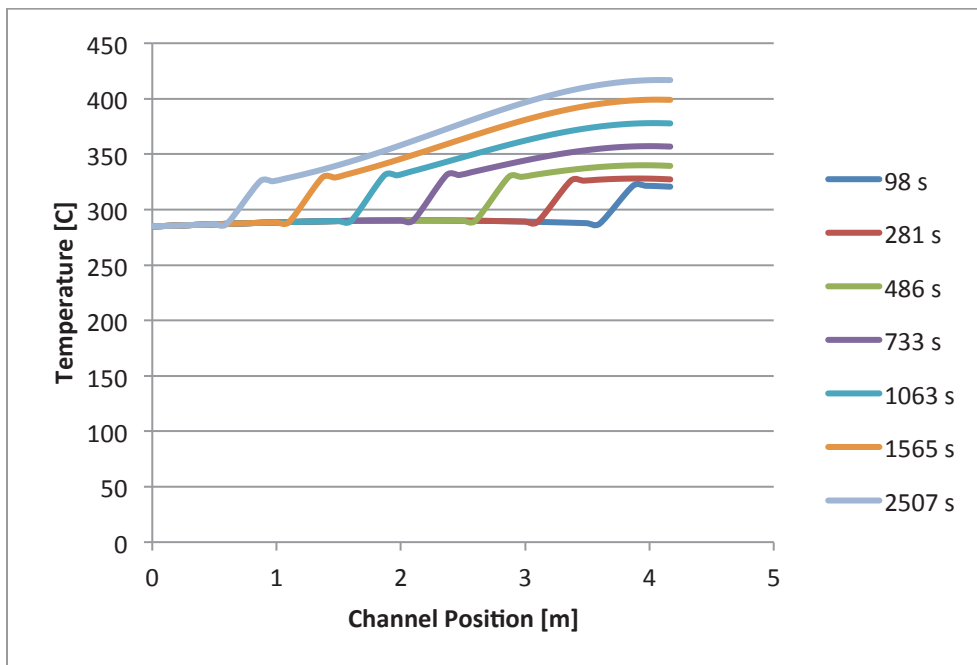

Figure 16. Fuel centerline temperature with a sinusoidal linear power density axial distribution as a function of position, using the Hsu and Westwater model for a heat transfer coefficient between the fuel and steam during film boiling.
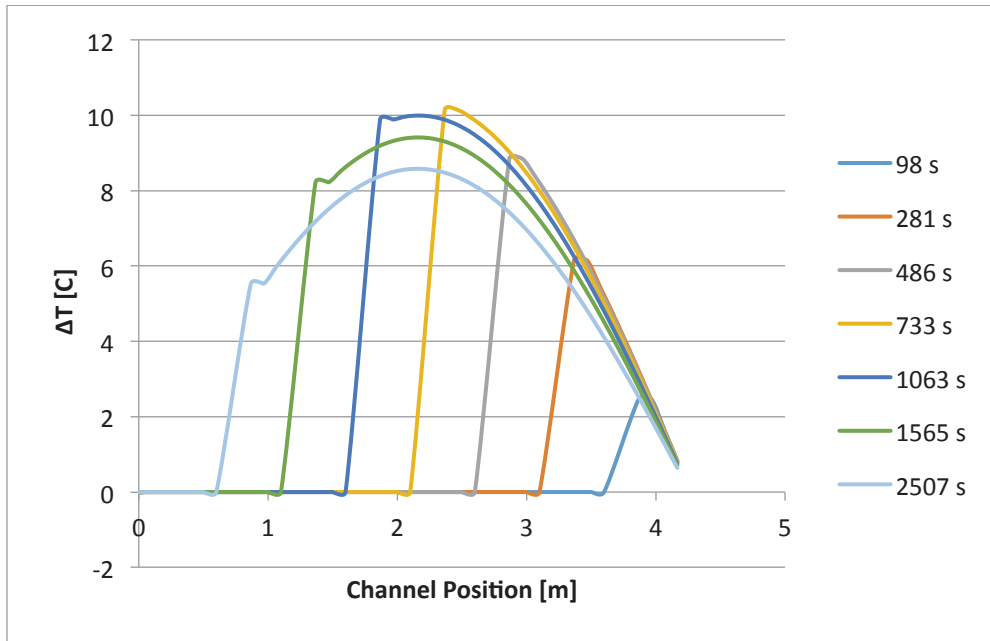
Figure 17. Temperature difference between the fuel centerline and the clad surface.

If one assumes that the fuel rod to steam heat transfer coefficient is essentially zero, or the steam flow rate is near zero, then the fuel centerline temperature increase is determined by the heat capacity of the fuel, as shown in Figure 18.
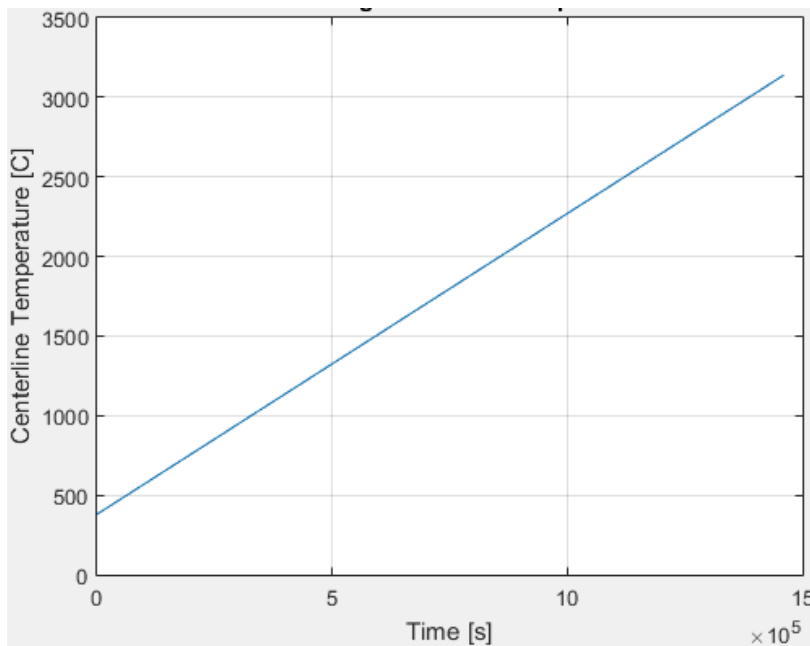

Figure 18. Fuel centerline axial temperature distribution as a function of position with no heat transfer between the fuel rod and the steam.

Summary of Observations

Results from this study are for the case of reactor operation of one year and a loss of coolant accident following one day after shutdown, and they are based on the assumptions cited in the text. Given these constraints, the following observations are made:

1) The loss of fuel cycle length for ZrO_2 film is about one-half day and about two days for the Ti_2AlC film. Thus, the economic penalty for loss of revenue due to the use of ceramic coatings is most likely acceptable if the coatings contribute to reactor safety.
2) The impact of coatings on fuel temperatures during normal operation appears to have no significant impact on reactor safety.
3) The time to boil the core dry after the complete loss of cooling, based on a zero-dimensional model, takes about 40 minutes.
4) For the case of no coating, the core temperature (based on the zero-dimensional model) will reach the Zr-H_2O reaction temperature (1,200 C) in an additional 20 minutes, or about one hour after the loss of coolant flow.
5) The time to initiate a Zr-H_2O reaction with coating and no cooling is based on the assumption that a "perfect" coating could prevent a Zr-H_2O reaction until the steam temperature reaches the melting temperature of Zr (about 1,830 C). Thus, the coating would prevent the Zr-H_2O reaction for an additional 20 minutes.
6) Given that there about 14,000 kg Zr cladding, a complete reaction of the Zr would yield about 600 kg of H_2 and about 8.8 E+10 J of energy.
7) If the Zr-H_2O reaction takes place in one hour, the specific power during the reaction would be about 0.3 W/g during the reaction, which is about 70 % higher than the energy release rate due to decay heat.
8) Results from the single channel analysis indicate that the time to boil dry is about 80 minutes.
9) The single channel analyses show that taking axially-dependent heat transfer coefficients and steam velocity into account effectively doubles the time to initiate the Zr-H_2O reaction as compared to the zero-dimensional analysis.
10) The use of coatings should extend the time to initiate the onset of a Zr-H_2O reaction by at least 20 minutes.

References

1. Duderstadt, James J. and Louis Hamilton. *Nuclear Reactor Analysis*. 1976. John Wiley & Sons, Inc.

2. Driscoll, M.J. Thomas Joseph Downar, and E. E. Pilat. *The Linear Reactivity Model for Nuclear Fuel Management*. American Nuclear Society. January 1, 1990.

3. Rasmussen, Inge L. *Optical Monitoring and X-Ray Absorption Spectroscopy for Studies of Wear on Thin Films*. December 2010. <http://www.nbi.ku.dk/english/research/phd_theses/phd_theses_2011/inge_l_rasmussen/inge_l_rasmussen.pdf>

4. Ding, Samani, and Chen. *Thermal Conductivity of PVD TiAlN Films using Pulsed Photothermal Reflectance Technique*. Applied Physics A. Springer-Verlag. July 2010.

5. Stéphane Orain , Yves Scudeller & Thierry Brousse (2001) STRUCTURAL AND MICROSTRUCTURAL EFFECTS ON THE THERMAL CONDUCTIVITY OF ZIRCONIA THIN FILMS, Microscale Thermophysical Engineering, 5:4, 267-275, DOI: 10.1080/10893950152646722

6. Todeas, Neil E. and Kasimi, Mujid S. *Nuclear Systems: Thermal Hydraulic Fundamentals*. Volume 1. 2nd Ed. CRC Press. 2012.

7. Schmidt, Frank W., Robert Henderson, and Carl Wolgemuth. *Introduction to Thermal Sciences*. 2nd Edition. John Wiley & Sons, Inc. 1993.

8. Schmidt, Henderson, and Wolgemuth. *Introduction to Thermal Sciences*. John Wiley & Sons. 2nd ed. 1993.

9. "Cross Section Metallography of TiAlN Coated ZIRLO." Ceramic Coating of Cladding Meeting. Pennsylvania State University. 12 July 2013. Lecture.

10. Stewart, Ian, *Impact of Fuel Rod Coatings on Reactor Performance and Safety,* Master of Science Thesis, The University of Tennessee, May 2015

11. Magnus Holmgren, X STEAM for Matlab, www.x-eng.com

Appendix – Matlab Code

The single channel analysis code logic is shown below. XSteam is used to find steam and water properties based on given parameters. The calculations performed in XSteam are based on the International Association for Properties of Water and Steam Industrial Formulation 1997 [12].
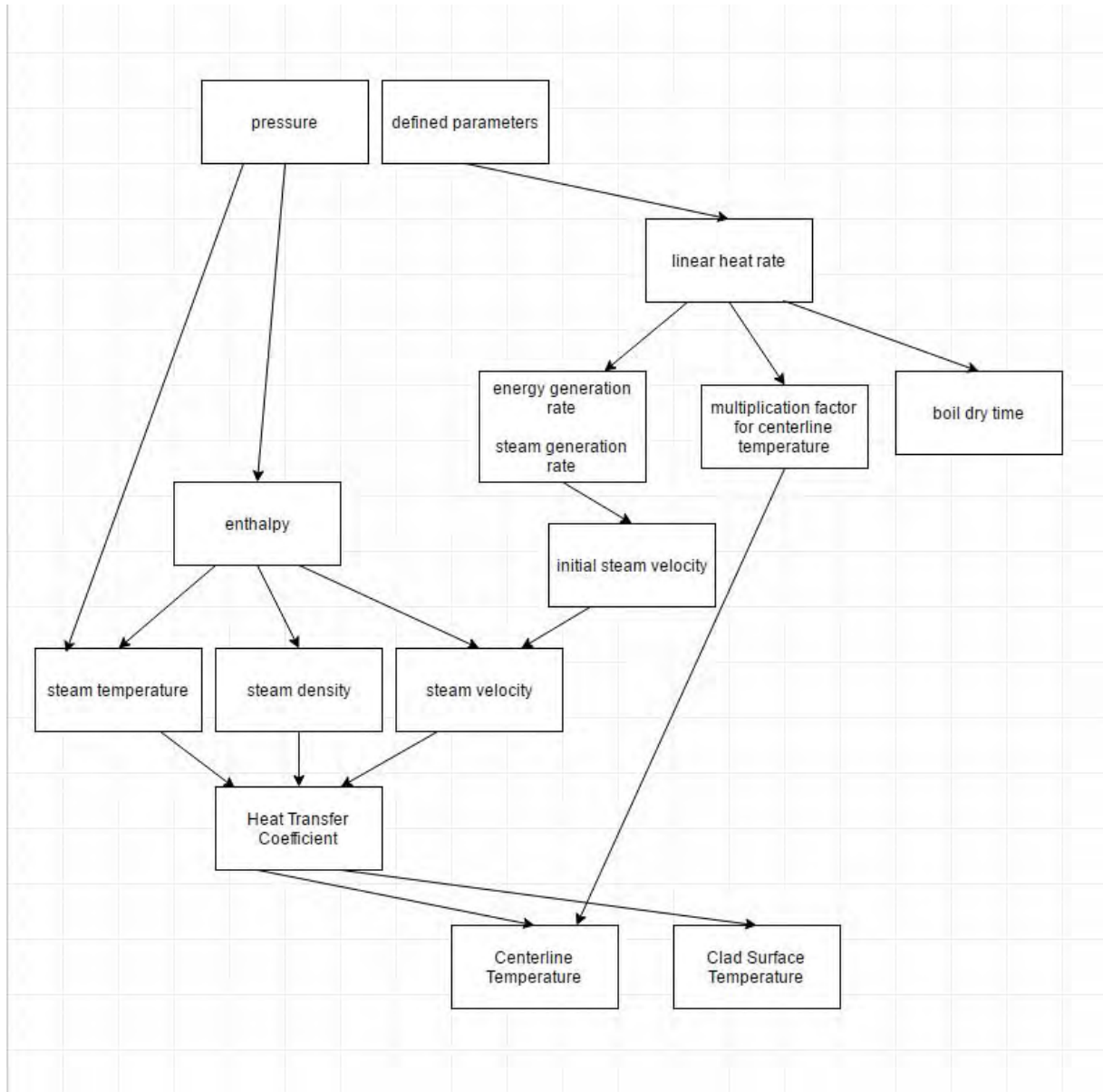
VII.   Summary of U.K. Collaborator Accomplishments

Papers (From Manchester)

I. Y. Liu, I. Bhamji, P.J. Withers, D.E. Wolfe, A.T. Motta, M. Preuss, Evaluation of the interfacial shear strength and residual stress of TiAlN coating on ZIRLO™ fuel cladding using a modified shear-lag model approach, Journal of Nuclear Materials, Volume 466, 2015, 718–727

In preparation (both are 80% completed):
II. Bhamjia, D. Lunta, J. Warda, D.E Wolfeb, A.T. Mottab, P.J. Withersa, M. Preussa Mechanical performance of TiAlN coatings before and after thermal exposure, to be submitted to JNM

III. Bhamjia, D.E Wolfeb, A.T. Mottab, J. Warda, S. Irukuvarghulaa, M Klausc, P.J. Withersa, M. Preussa, Residual stress and phase transformation during thermal excursions of TiAlN type coatings for accident tolerant fuel, to be submitted to JNM